ELECTRICAL AND OPTICAL CHARACTERISTICS OF INDIUM ARSENIDE JUNCTION LASERS

Thesis by

Navin B. Patel

In Partial Fulfillment of the Requirements

For the Degree of

Doctor of Philosophy

California Institute of Technology

Pasadena, California

1971

(Submitted February 23, 1971)

ACKNOWLEDGMENTS

The author wishes to express his sincere appreciation to Professor Amnon Yariv for his invaluable guidance and encouragement during the course of this research. I am also grateful to Mr. Desmond Armstrong for his patient and skilled assistance in the laboratory, and Mrs. Aldre´ Khoury, Mrs. Ruth Stratton, Mrs. Karen Current and Mrs. Carol Norris for their expert job of typing the manuscript. In addition, I would like to thank the following people whose help I received: Professor C. Mead, Professor M.-A. Nicolet, Professor N. George, Dr. H. Flicker, Dr. J. Zoutendyk, Dr. I. Melngailis, Mort Simpson, Earle Emery, Richard Wileman, Paula Samazan, V. Arakeri, P. Bhatia and N. Singh.

The financial support received from the Office of Naval Research, the Josephine de Karman Trust, and the California Institute of Technology is greatly appreciated.

To my parents

ABSTRACT

Electrical and light emission characteristics of pulsed InAs junction lasers were studied at various temperatures ranging from liquid helium temperature to room temperature. The junctions were prepared by vapor diffusing Zn into Sn doped n-type wafers of InAs, with a donor concentration of $10^{18} cm^{-3}$. Data of variation of capacitance with bias showed these to be abrupt junctions. At low injection currents, the current injection mechanism was determined to be photon-assisted tunneling. Gain and loss factors at $20.4^{o}K$ were determined from the variation of threshold current with diode cavity length. An independent value of the gain factor was determined from the observed variation with current of the superradiantly narrowed line-width from a nonlasing structure. The time-resolved laser spectra shift to longer wavelengths with time during pulsed operation of the laser. The line shift results from joule heating of the diode, and follows the variation of bandgap of InAs with temperature. Mode confinement studies indicate that the mode confinement is due to the optical gain in the active region at the junction and that the active region extends to approximately a diffusion length on both sides of the junction.

TABLE OF CONTENTS

Introduction		1
I.	Review of relevant semiconductor and p-n junction theory	4
II.	Device fabrication	20
III.	Current injection mechanism	35
IV.	Threshold current, gain and loss coefficients, superradiant narrowing, axial mode distribution, and stimulated external quantum efficiency	58
V.	Heating effects and time resolved spectra	77
VI.	Mode confinement	87
REFERENCES		101
LIST OF FIGURES		103

Introduction

InAs is a member of the III-V group of compounds. Though it was demonstrated in 1952, by Welker [1], that these compounds are semiconductors, little attention was paid to them until 1962, when laser action in GaAs diodes was discovered [2]. Since then, the study of spontaneous and stimulated emission of light from these and other semiconductors has become an exciting field of semiconductor physics and quantum electronics combined.

InAs is a narrow band-gap material (E_g = 0.42 electron-volt at a temperature of 4.2°K). Therefore the radiative recombination of electrons in the conduction band and holes in the valence band produces photons whose wavelength is in the infrared ($\lambda \simeq 3.1\ \mu$ in vacuum.) Laser action in InAs junctions was first reported by Melngailis, who also reported effects of magnetic fields on the emission from these junctions, efficiency measurements, results on optically pumped InAs lasers and on the various states involved in optical transitions in both n and p type materials [3]. Described in the present work are the results of experiments conducted with p-n junction lasers in InAs which are aimed at understanding the various physical processes obtaining in these pulsed junctions during spontaneous and stimulated radiative recombination.

The p-n junction diode is a convenient device for the study of spontaneous and stimulated light emission from semiconductors. It has the simplicity of excitation by an electric current compared to the more cumbersome and less efficient optical excitation required for most conventional lasers. All the p-n junctions were made by vapor diffusing Zn into n-type single crystal bulk material. Diffusions were made into

polished (100) and (111) faces as well as into cleaved (110) faces with junction depths ranging from 12 to 25 μ. Opposite ends of the diode structures were cleaved to give parallel reflectors, thereby forming the Fabry-Perot cavity needed for a laser oscillator.

Since the emission of light originates from the recombination of injected current carriers the nature of the radiation depends on the injection mechanism. The spontaneous light emission at low current levels was investigated in parallel with the electrical characteristics. The data are consistent with the model for photon-assisted tunneling across the junction.

When injection lasers are driven by current pulses, the temperature rise during the pulse causes transient changes in the observed spectra. All pulsed injection lasers exhibit "mode-jumping" to longer wavelengths during the time interval when the laser is pumped, particularly under conditions of high current level excitation. The time-resolved laser spectra of the InAs junctions were observed to shift to longer wavelengths. The line shift results from joule heating of the junction and follows the variation of bandgap with temperature.

Data on the threshold current for stimulated emission (for a diode temperature of 20.4°K) as a function of the reciprocal cavity length were obtained. These data yield a value of $\alpha = 40$ cm^{-1} for the total cavity loss constant, and $\beta \approx 10$ Amp. cm^{-1} for the gain constant of the junction. An interesting side experiment was performed which also gave an independent value of β at 20.4°K. Measurements were made on the variation with current of the superradiant line narrowing of the radiation from a nonlasing structure. The results were consistent with the theory of superradiant line narrowing given by Yariv et al [4].

Data obtained from measurements of the far-field diffraction pattern of the stimulated-mode light intensity profile (in a direction perpendicular to the junction plane) indicate that the active region of high gain (the region where a population inversion exists) extends to approximately a diffusion length on both sides of the junction. The data also indicate that the confinement of the oscillating modes within the diode cavity is due to a variation in the real part of the dielectric constant, caused by the optical gain in the junction region.

The external quantum efficiency (η_d) for stimulated emission (at 20.4°K) was calculated by using the total light intensity vs. diode current data, plus the material parameters of the mercury doped germanium detector used for the measurements. The value obtained was $\eta_d \approx 10\%$. The corresponding radiative power output (at $\lambda = 3.1\ \mu$) is approximately 200 milliwatts for a diode current of 5 amps.

Chapter I

Review of Relevant Semiconductor and P-N Junction Theory

1.1 General Remarks:

Indium Arsenide (InAs) is a member of the family of crystalline semiconducting compounds, known as III-V compounds, formed by atoms from group IIIb (B, Aℓ, Ga, In, Tℓ) combining with atoms from group Vb (N, P, As, Sb, Bi). These substances are not alloys but definite chemical compounds with a 1:1 ratio between the III and V atoms which occupy alternate sites in the crystal lattice. As distinct from the elemental group IV semiconductors [e.g. Ge, Si, C (diamond)] in which the crystal binding is purely covalent, the III-V compounds contain an ionic binding component in addition to the predominant covalent bonding. The majority of the III-V compounds form crystals with the zinc-blende structure. This structure is similar to that of diamond except that there are two kinds of atoms in the unit cell. There are a large number of possible combinations, and these compounds cover a wide range of semiconducting properties, useful both for a study of semiconduction and for the manufacture of devices. The value of the bandgap energy ranges from approximately 10 eV for BN to 0.17 eV for InSb.

In spite of the fact that these compounds have two different atoms in the unit cell they sometimes show simpler behaviour than monoatomic group IV semiconductors. Indium antimonide and Indium arsenide, for example, approximate rather closely the simplest model of a semiconductor in which a spherical conduction band and a spherical valence band both lie at the center of the Brillouin zone. The energy band

structure for such a simple semiconductor crystal is illustrated in Figure 1-1(a). We note that the semiconductor has a direct-band structure (and the semiconductor is known as a direct semiconductor) in that the valence band energy maximum and the conduction band energy minimum occur at the same k-value in the Brillouin zone. This is as opposed to an indirect semiconductor in which the band extrema do not occur at the same k value in the Brillouin zone (Figure 1-1(b)).

This distinction between direct and indirect semiconductors is a very important one as far as optical transitions and hence the lasing properties of the semiconductor are concerned. Optical transition in a direct band-gap semiconductor is a first-order process since the momentum is automatically conserved during the transition, [$(k_c)_{min} = (k_v)_{max}$, Figure 1-2(a)], and hence the transition rate can be expected to be high. In an indirect semiconductor, the condition of momentum conservation during an optical transition can be met in two ways. First, the transition may take place away from the band edge(s), [process (1), Figure 1-2(b)] with $\bar{k}_c = \bar{k}_v$. However the electron-hole population available for such a transition would be relatively very small since electrons and holes usually experience thermal relaxation to energy states near the band edges before radiative recombination can occur. Secondly, the transition may take at the band edges [process (2), Figure 1-2(b)], but will involve the emission or absorption of a lattice phonon, with momentum conservation expressed as

$$\bar{k}_c = \bar{k}_v \pm \bar{k}_{phonon} \tag{1-1}$$

and energy conservation as

$$\hbar\omega_{photon} = E_c - E_v \pm \hbar\omega_{phonon} \tag{1-2}$$

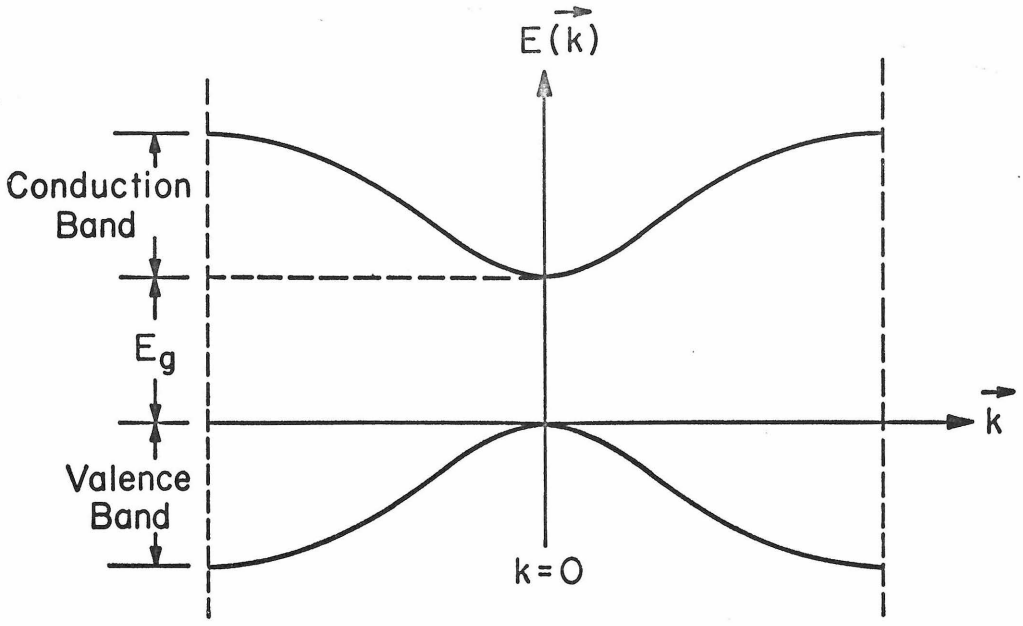

(a) Conduction and Valence Bands

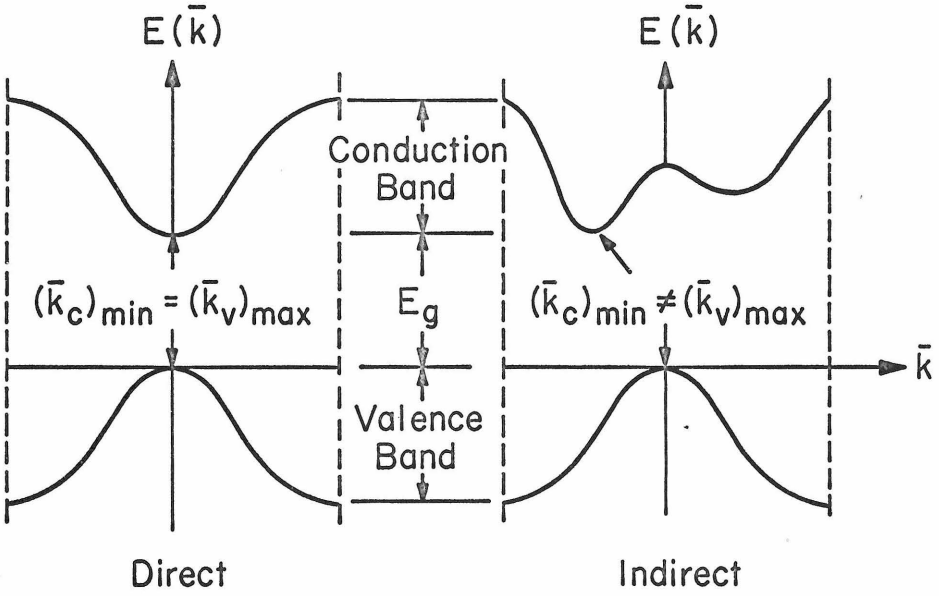

(b) Direct and Indirect Semiconductors

Figure 1-1. Energy Bands in Semiconductors

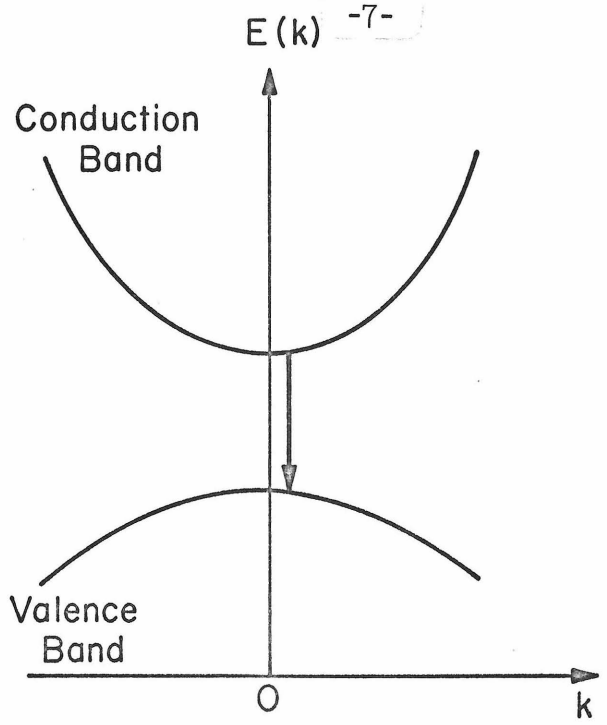

(a) Direct Semiconductor

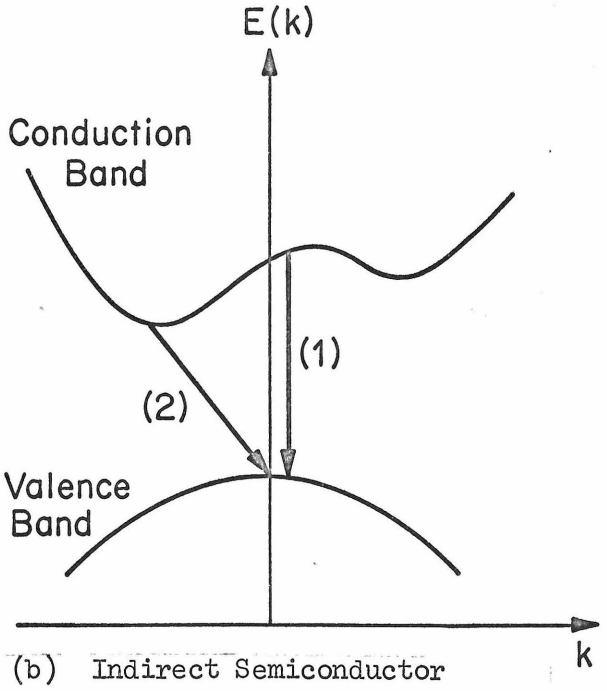

(b) Indirect Semiconductor

Figure 1-2. Radiative Transitions in Semiconductors

But this is a second order process and the probability of such a phonon-assisted radiative recombination occuring is much less than that for a direct transition. We see thus that the probability for radiative recombination can be expected to be much higher in direct semiconductors than in indirect semiconductors. At present all the well substantiated lasing semiconductors have direct-band structures.

InAs has a direct-band structure with a bandgap energy of 0.425 eV at $0^{\circ}K$ and 0.36 eV at $300^{\circ}K$. Between $77^{\circ}K$ and $300^{\circ}K$ the temperature dependence of the bandgap is known to be linear and is given by [5]

$$\frac{dE_g}{dT} = -2.8 \times 10^{-4} \text{ eV}/^{\circ}K \quad - \qquad (1\text{-}3)$$

1.2 Inversion Condition for Semiconductor Lasers

As in ordinary lasers, the amplification of radiation in semiconductors is the exact opposite of absorption, and it involves a reversal of the position of occupied and unoccupied energy states; in other words it involves a population inversion. To consider the inversion condition for a semiconductor laser, refer to Figure 1-3, which shows the energy versus density of states in a direct band-gap semiconductor. Figure 1-3(a) shows the equilibrium condition at $T = 0^{\circ}K$ for an intrinsic semiconductor in which the shaded area represents the filled states. Figure 1-3(b) shows the situation for an inverted population at $0^{\circ}K$. This inversion can be achieved, for example, by photoexcitation with photon energy greater than the band gap E_g . The valence band is empty of electrons down to an energy E_{FV} (quasi-Fermi level for holes in valence band), and the conduction band filled up to E_{FC} (quasi-Fermi level for electrons in

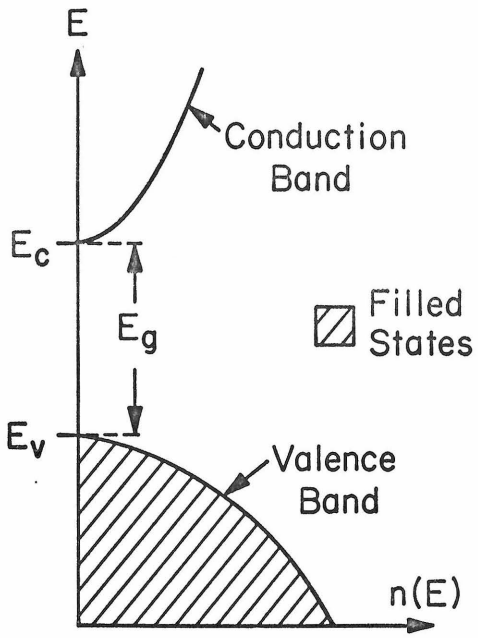

(a) Equilibrium, T = 0°K

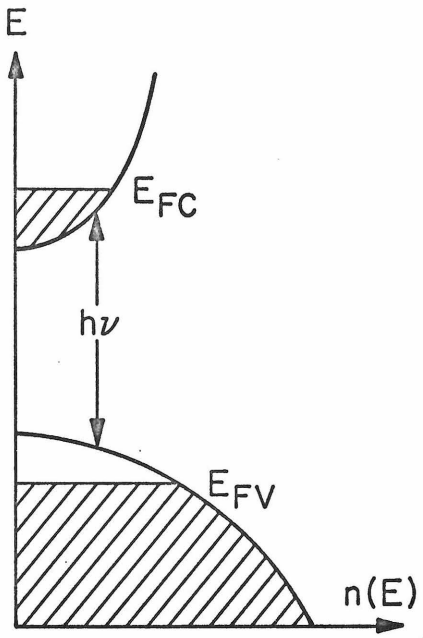

(b) Inverted, T = 0°K

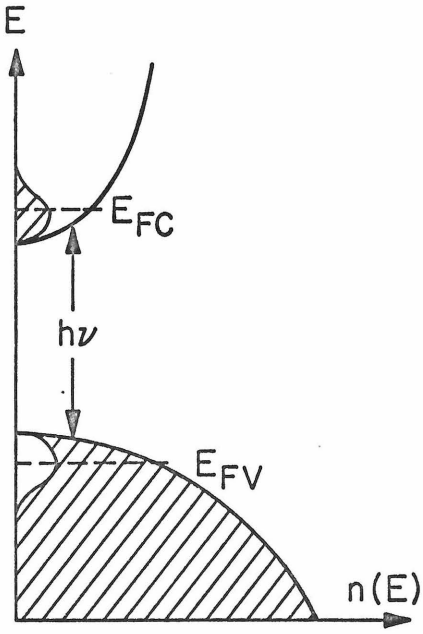

(c) Inverted, T > 0°K

Figure 1-3. Energy versus Density of States in a Semiconductor

the conduction band). Now photons with energy $h\nu$ such that $E_g < h\nu < (E_{FC} - E_{FV})$ will cause downward transition and hence stimulated emission.

At finite temperatures, the carrier distributions will be "smeared" out in energy as shown in Figure 1-3(c). Although overall thermal equilibrium does not exist, carriers in a given energy band will be in thermal equilibrium with one another. The occupation probability of a state in the conduction band is given by the Fermi-Dirac distribution

$$F_c(E) = \frac{1}{1 + \exp(\frac{E-E_{FC}}{kT})} \qquad (1\text{-}4)$$

A similar expression holds for the valence band.

Consider the rate of photon emission at ν due to a transition from a group of upper states near E in the conduction band to lower states at $(E-h\nu)$ in the valence band. The rate for this emission is proportional to the product of the density of occupied upper states $n_c(E)F_c(E)$ and the density of the unoccupied lower states $n_v(E-h\nu)[1-F_v(E-h\nu)]$. The total emission rate is obtained by integrating over all energies.

$$W_{emission} \sim \int n_c(E)F_c(E)n_v(E-h\nu)\,[1 - F_v(E-h\nu)]\,dE \qquad (1\text{-}5)$$

In a similar manner, we can write for the absorption rate,

$$W_{absorption} \sim \int n_v(E-h\nu)\,F_v(E-h\nu)\,n_c(E)\,[1 - F_c(E)]\,dE \qquad (1\text{-}6)$$

with the same proportionality constant, which includes the square of the transition probability matrix element. For a net amplification we

require that $W_{emission} > W_{absorption}$. From equations (1·4), (1·5) and (1·6) we obtain

$$E_{FC} - E_{FV} > h\nu \qquad (1\text{-}7)$$

This is the required inversion condition, and is referred to as the Bernard-Duraffourg condition [6]. It is a necessary condition for stimulated emission to be dominant over absorption for conduction to valence band transitions in an intrinsic semiconductor.

1-3 General Ideas about P-N Junction Diode Lasers:

The condition of population inversion discussed above, can be obtained in a semiconductor material by exciting electrons from the valence band to the conduction band by some external means. In bulk semiconductors, this may be achieved by several methods, such as (a) photo-excitation (b) electron beam excitation and (c) avalanche production of electron-hole pairs. Methods (a) and (b) require special external sources while method (c) requires extremely high applied voltages. However, the semiconductor p-n junction diode provides, by virtue of its indigenous structure, an excellent scheme for producing a population inversion and hence, stimulated emission of radiation.

The energy band diagram for a degenerate p-n junction is shown in Figure 1-4(a), for the condition of zero bias. The built-in voltage (V_B) is such that there is equal and opposite "thermionic" current flow of magnitude I_o from the two sides of the junction, resulting in a net zero current. The voltage barrier V_B results from the formation of excess negative and positive charge regions on the p and n sides, respectively. The excess-charge dipole layer (referred to as the

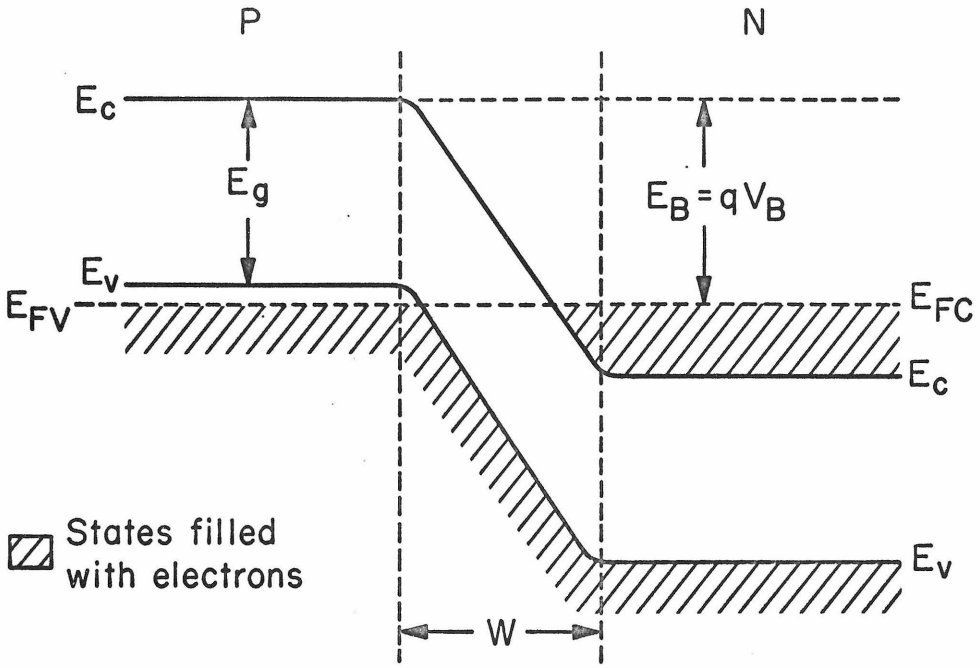

(a) With Zero Bias

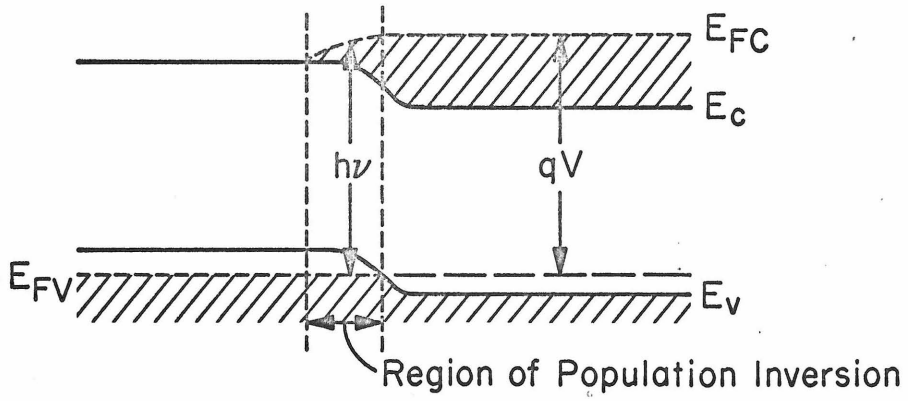

(b) With Forward Bias (V) and an Effective Population Inversion

Figure 1-4. A Degenerate P-N Junction

depletion layer) is required to equalize the Fermi-levels on the two sides of the junction (a necessary condition for thermodynamic equilibrium).

The junction is degenerate in that the constituent p and n materials are degenerately doped. [A semiconductor is said to be degenerately doped when the doping is so heavy that the Fermi-level moves into the conduction band or the valence band depending on whether the impurity is n-type or p-type.] This is a necessary condition in order to satisfy the population inversion condition (1-7) discussed above. Figure 1-4b illustrates the presence of an effective population inversion at the junction of a forward Biased diode, with bias V.

For an abrupt junction (i.e. uniform donor and acceptor densities on the p and n sides) the width of the depletion layer (or junction width) with an applied voltage V is given by [7]

$$W = W_1(V_B - V)^{\frac{1}{2}} \tag{1-8}$$

with

$$W_1 = \left(\frac{2\epsilon}{q}\right)^{\frac{1}{2}} \left[\frac{N_A + N_D}{N_A N_D}\right]^{\frac{1}{2}} \tag{1-9}$$

where N_A and N_D are the acceptor and donor densities on the p and n sides, ϵ is the static dielectric constant of the material and q is the magnitude of the electronic charge.

The depletion layer of an abrupt junction behaves like a parallel plate capacitor with a capacitance (differential) per unit junction area of

$$C = \left(\frac{\epsilon}{W_1}\right) (V_B - V)^{-\frac{1}{2}} \tag{1-10}$$

With the application of a forward bias voltage (V), the minority carriers' current injected over the barrier increases by a factor $e^{qV/\beta kT}$ while the opposing thermally generated majority carrier current remains the same (I_o). The net flow of thermionic current across the junction is given by

$$I = I_o \left[e^{qV/\beta kT} - 1\right] \qquad (1\text{-}11)$$

where k is Boltzmann's constant and β is a numerical constant determined by the amount of generation and recombination of carriers which occurs in the depletion region [8].

1-4 Tunneling Currents in Narrow Junctions.

As stated above, relation (1-11) gives the diode current due to the "thermionic" injection of minority carriers across the junction barrier. However if the junction is very narrow (i.e. the junction width W is very small, of the order of a hundred angstroms or less) then the probability of carriers tunneling across the junction is large, and for low enough temperatures and forward bias voltages, the injection of minority carriers across the voltage barrier may be less than the injection due to tunneling through the barrier. In this region then, the current-voltage (I-V) characteristics will be dominated by tunneling currents rather than thermionic current.

We see from relation (1-9) that the junction width is inversely proportional to the impurity concentration in the n and p sides, so that the higher the doping the narrower the junction. Now we saw in the previous discussion that p-n junction laser diodes, in order to satisfy the population inversion condition, have to be degenerately doped.

Consequently they have very narrow junctions, and much more often than not, it will be found that lasing diodes exhibit tunneling effects in their I-V characteristics.

In Figure 1-5 are shown the energy band diagrams for a degenerately doped junction, with different biasing conditions. For a junction with no bias applied (Figure 1-5(a)) tunneling transitions are possible in the energy range between levels r and s shown in the diagram. Transitions will actually occur only over a small interval near the Fermi-level in which both electrons and holes are available in reasonable numbers. Of course there is no net flow of current in equilibrium since transitions occur with equal frequency in both directions.

As a reverse bias is applied (Figure 1-5(b)) the filled electron levels in the p-type material become higher than empty levels in the n-type. Tunneling can occur and current flows; the current indeed increases with reverse bias, because more filled levels come into play. Tunneling also occurs for a forward biased junction, for here too filled and empty levels overlap (Figure 1-5(c)). The current increases as the bias is increased, but it does not increase indefinitely, since ultimately the filled electron levels are raised to the point where they are opposite forbidden states in the gap of the p-type material (Figure 1-5(d)). Tunneling out of these filled states cannot occur and the tunneling current decreases with further increase in the forward bias. The composite characteristic of such a device is shown in Figure 1-6. This is the so called "tunnel diode" characteristic.

The tunneling process described above is the "horizontal" tunneling,

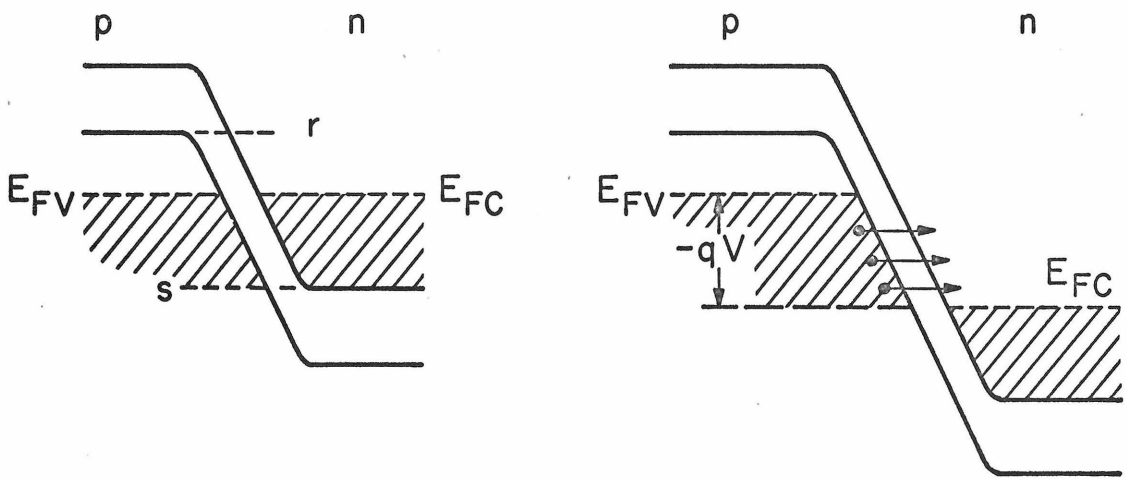

(a) Zero Bias

(b) Reverse Bias

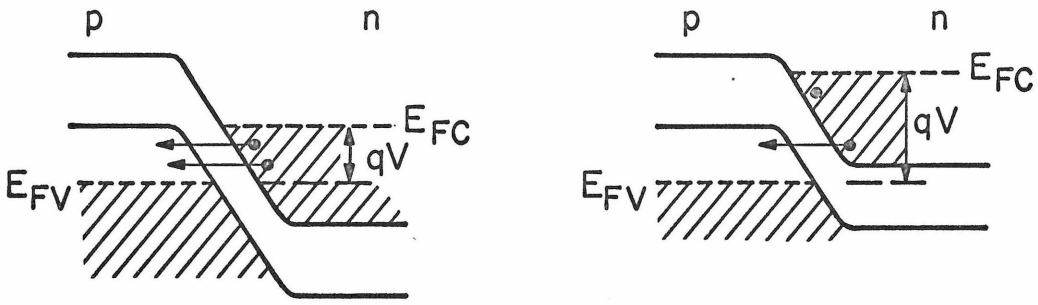

(c) Forward Bias

(d) Forward Bias

Figure 1-5. Energy Band Diagrams of Tunnel Diode

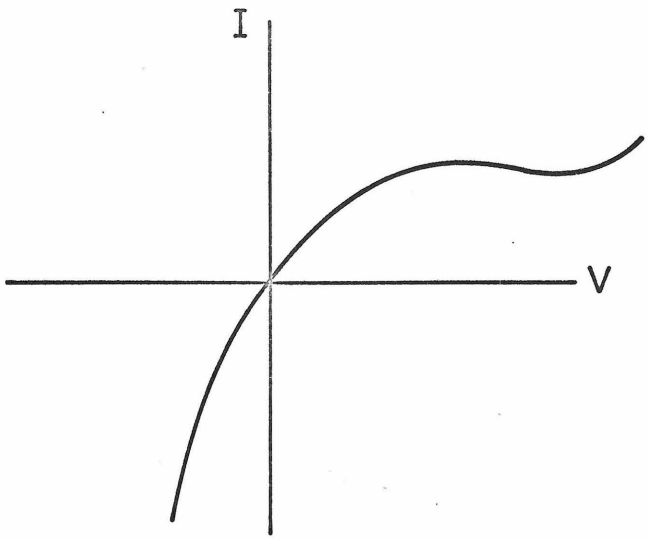

Figure 1-6. Tunnel Diode I-V Characteristic

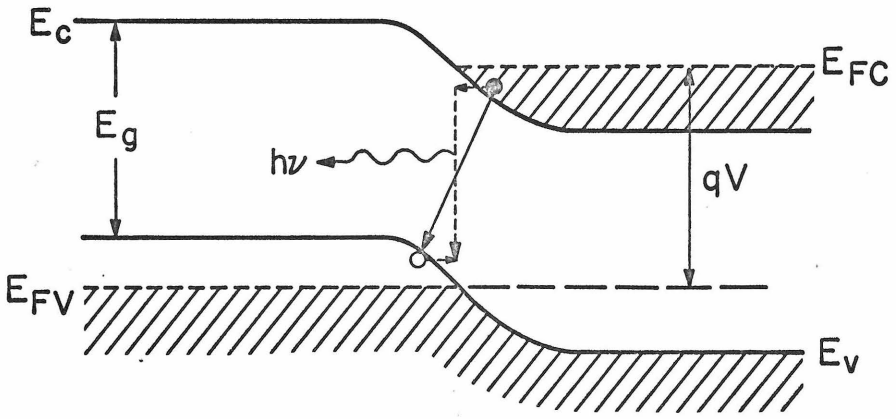

Figure 1-7. The "Diagonal" Tunneling Model

in which energy is conserved. At moderately large applied forward biases, another kind of tunneling can occur in which the tunneling holes and electrons recombine radiatively to aid the tunneling process. This mechanism of photon-assisted tunneling has been discussed in detail by Leite et al [9] in conjunction with experiments using GaAs p-n junctions. The "diagonal" tunneling model used to explain this phenomenon is shown in Figure 1-7. It is based on the simultaneous tunneling, under the influence of the large electric field present in the junction, by an electron (from the n side) and a hole (from the p side) into the junction region where they recombine radiatively via the emission of a photon. The net result is the diagonal transition of an electron from the n-side to a hole state on the p-side. The diagonal tunneling is therefore a source of current flow as well as a source of radiation. At the point in the junction where the integrand of the matrix element for the radiative transition of an electron to a hole state is a maximum, the probability for radiative recombination is also at a maximum. For the completely symmetric case of equal electron and hole effective masses and equal impurity doping, the point of maximum transition probability will occur exactly at the middle of the junction. If we take the total radiated light intensity ($\mathcal{S}$) to be proportional to the radiative transition probability at midjunction, the dependence of $\mathcal{S}$ on the applied voltage (V) for an abrupt junction is [9]

$$\mathcal{S} \sim e^{S_T V} \tag{1-12a}$$

with

$$S_T = \left(\frac{q}{2}\right)^{3/2} \frac{\pi m_T^{\frac{1}{2}}}{2q\hbar} W_1 \tag{1-12b}$$

Here W_1 is the width constant in (1-8), and m_T is the reduced effective tunneling mass for electrons and holes. Also, the slope S_T should be independent of temperature.

Another consequence of the tunneling model becomes clear from a study of Fig. 1-7. Since only electrons and holes very near the respective quasi-Fermi levels E_{FC} and E_{FV} have an appreciable probability of tunneling (these carriers have the smallest barrier against which to tunnel), it follows that the applied voltage V and the peak radiation frequency ν_p are related by

$$h\nu_p \cong qV \qquad (1\text{-}13).$$

Chapter II

Device Fabrication

2-1 Introduction

The finished device units used in the experimental study consisted of Fabry-Perot cavities of InAs p-n junctions mounted suitably on TO-5 transistor headers, with appropriate contacts to the p and n sides. The TO-5 headers were used because of the simplicity of mounting them either on the cold-finger dewar or in the cold-immersion dewar. The fabrication of these finished units starting from bulk InAs consisted of several steps which were carried out in sequential order and are described in this chapter.

2-2 Preparation of the Bulk Material

The bulk material, supplied by the Monsanto Company, was in the form of wafers 1/2 mm thick. Their diameters varied from 1 cm to 2.5 cm, depending upon the ingot from which they were cut. Some of the wafers were oriented along the (111) direction and some along the (100) direction. Each wafer had one side lapped down 5 mils after sawing to remove the surface layer damaged by the sawing. This face of the wafer had then been polished down to 0.3 micron fineness.

The junction formed by the diffusion of Zn into these polished (111) and (100) faces were used in making the diode cavities for some of the devices. As a result these devices had their junctions lying along (111) or (100) planes. For some other devices the junction used was that formed by the diffusion of Zn into a cleaved (110) face. The reason for doing this was as follows. For a diode to lase efficiently, a primary requirement is that the junction be as plane as possible.

Assuming the diffusion front to be uniform, this requires that the face into which the diffusion is done be as planar as possible. There was some uncertainty as to whether the polishing on the (111) and (100) wafers was good enough to provide good plane junctions. On the other hand, a cleaved face of a crystal provides a natural perfect plane, providing there are no cleavage flaws.

InAs has a natural cleavage in the (110) set of planes and there are two mutually perpendicular sets of these planes at right angles to a (100) face. The thinner the crystal section to be cleaved, the easier it is to cleave it. It was found that InAs cleaved along the (110) planes in an easy and predictable manner if the wafers being cleaved were 15 mils or less in thickness. Hence, the (100) wafers to be cleaved were first hand-lapped down to a thickness of 12-13 mils. The orientation of the (110) planes in the wafer was found by poking around on the edge of the wafer with a sharp metal point until a small piece cleaved off in one of the (110) planes. This gave the orientation of one set of (110) planes and the other set was perpendicular to it.

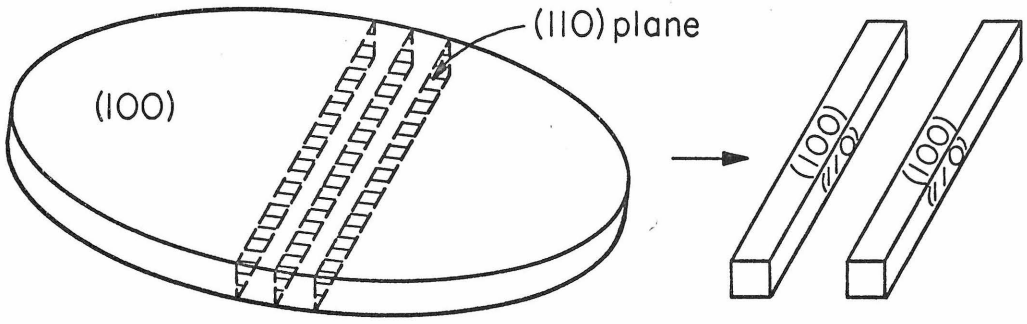

Figure 2-1. Cleaving Configuration of (100) Wafer of InAs

The wafer was then placed on a flat glass plate under a microscope and cleaved along a desired (110) plane by holding a sharp razor edge along the boundary of this plane on top of the wafer and then tapping the other edge of the razor with a cylindrical metal piece. Starting with a (100) wafer and cleaving in this manner, long rods of InAs, each with two opposite, cleaved (110) faces, were obtained (Figure 2-1). These were the cleaved faces into which Zn was diffused to get junctions lying along (110) planes.

2-3 Diffusion of Zn into the Bulk Material

All the p-n junctions were made by diffusing a p-type layer onto the n-type bulk material. The diffusion took place in a 30 mil quartz tube. To reduce the vapor pressure of Zn, an alloy of 50 mg Zn and 450 mg Ga was used as the diffusion source. The source and n-type InAs crystals (which had previously been prepared for diffusing as described in the previous section) were placed in the quartz tube and the tube pumped down to 10^{-6} torr. During the vacuum pumping the tube was gently heated with hydrogen-oxygen torch flame. The tube was then sealed off with the torch and checked for leaks with a Tesla coil. The sealed tube configuration is shown in Figure 2-2.

The sealed tube was placed in the center of a diffusion furnace which had been preheated to the diffusion temperature and stabilized at that temperature for 12 hours (Figure 2-3). Different diffusions were done at different temperatures, ranging between 520°C and 565°C. The diffusion times varied between 1 hour and 3 hours. At the end of the diffusion run, the quartz tube was removed from the furnace and quenched in water.

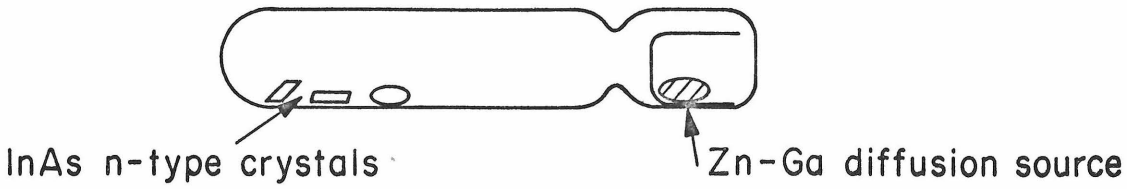

Figure 2-2. Diffusion Tube for InAs

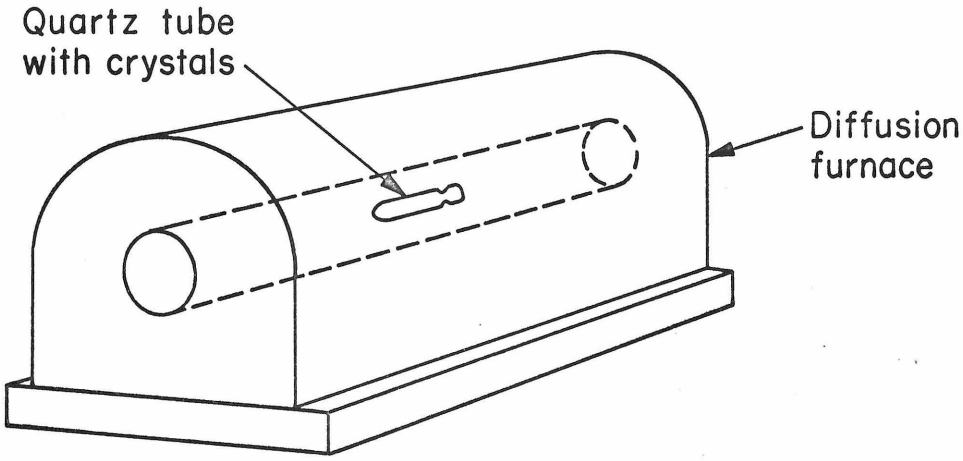

Figure 2-3. Diffusion Furnace

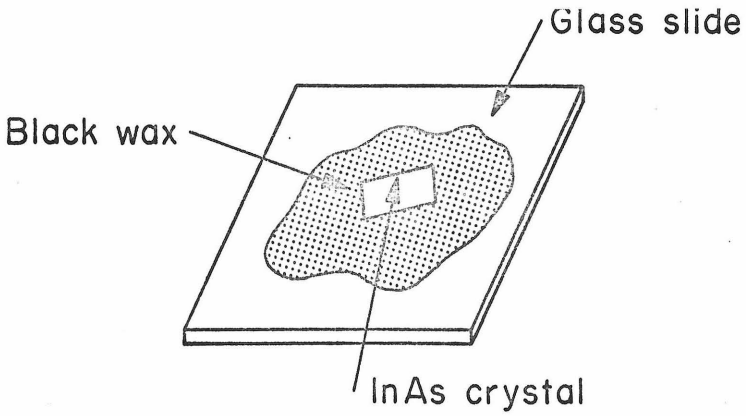

Figure 2-4. Lapping Configuration of InAs Crystals

During the diffusion run at the elevated temperature, the Zn from the vapor phase had diffused into the n-type material, forming a p-type layer completely surrounding the single crystal samples. The equilibrium conditions were frozen in by quenching the crystals at room temperature, thereby forming a permanent p-n junction at a given depth.

After quenching, the tube was broken open and the crystals were checked using a thermoelectric probe (hot-point probe) to verify the presence of a p-type layer.

2-4 Formation of Diodes from the Diffused Material

The diffusion runs provided junctions in diffused material with three different orientations from which to form the diode cavities. There were the large wafers oriented along the a) (100) and b) (111) directions and c) the long bars having two opposite cleaved (110) faces. In all of them it was necessary to remove the diffused p-layer from all but a single surface.

a) For the (100) oriented wafers, the first step was to remove the junction from the face opposite to the polished face. Each wafer was mounted (with polished face down) on a glass slide, using a low melting point black wax (Figure 2-4). The exposed surface was then hand lapped (using a 18 micron abrasive material mixed with distilled water) on a fine cloth surface until the p-layer was removed. The removal of the p-layer from the crystal face was verified with the use of a hot-point probe. The lapped wafer was removed from the glass slide by dissolving the black wax in ethylene. It was then placed (junction face down) on a glass slide under a microscope and cleaved, using a razor blade, along a set of (110) planes into long bars about 10 mils

wide (Figure 2-5).

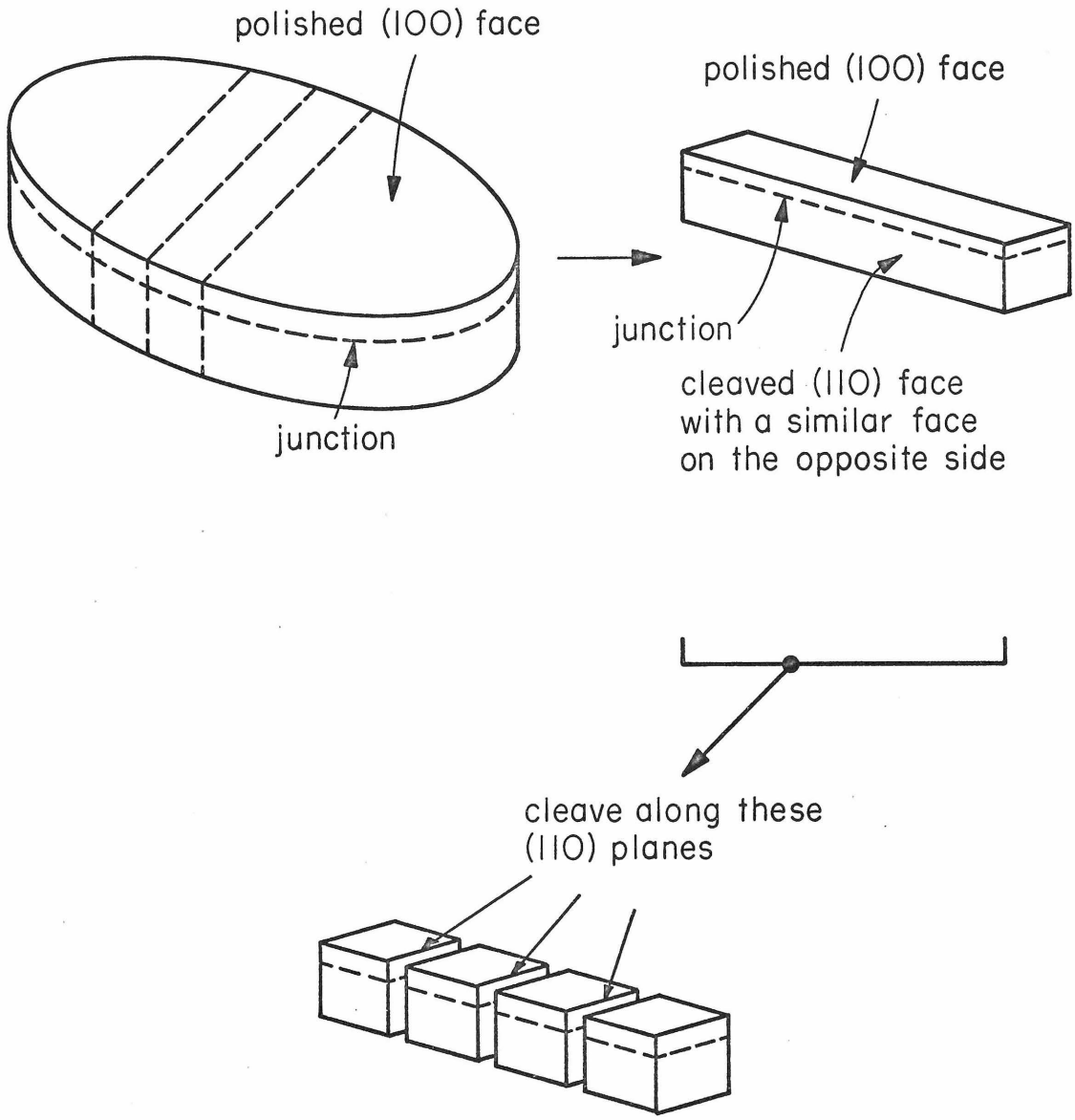

Figure 2-5. Fabrication Steps for a Laser Diode Cavity

These bars were mounted on a glass slide (using the black wax) with one of the cleaved (110) faces exposed. This face was then roughened by hand-lapping for about five seconds in 5μ abrasive. Each bar was then cleaved along the other set of (110) planes to get rectangular parallelipiped shaped diode cavities (Figure 2-6 in which typical dimensions are also shown) in which one pair of opposite faces was optically reflecting while the other pair had one side roughened. (In some of the cavities both the sides of this other pair were roughened.) These cavities could then act as Fabry-Perot structures in one direction.

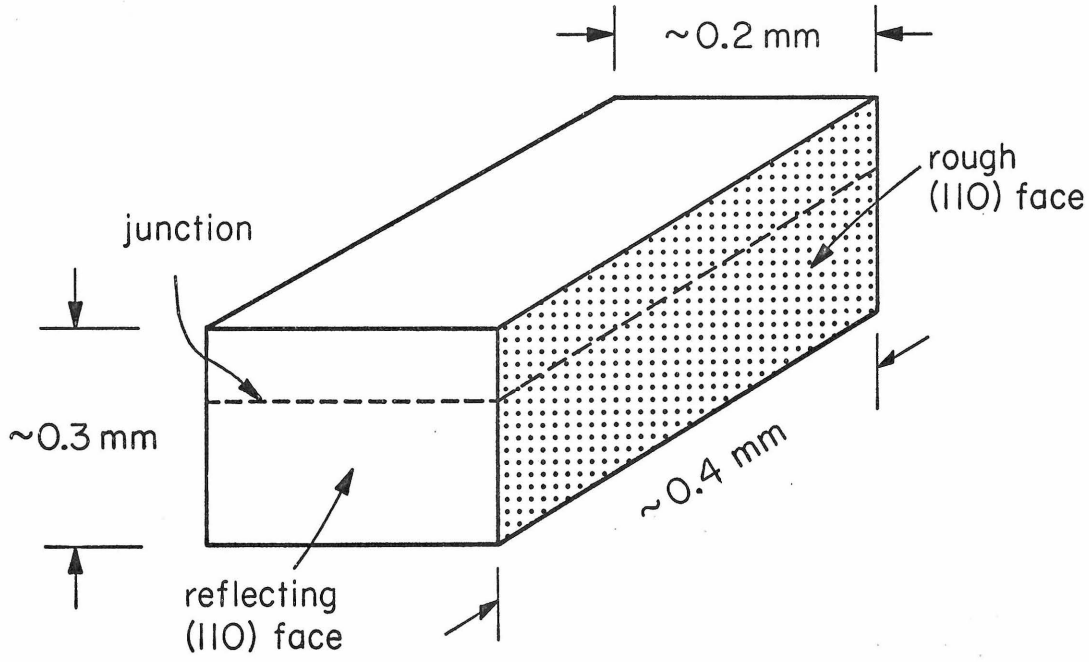

Figure 2-6. Finished InAs Laser Diode

b) A similar procedure was followed in the case of the (111) oriented wafers, except that at right angles to a (111) plane there are three sets of (110) cleavage planes at 60° to one another, so that the end products after cleaving were diode cavities in three shapes: 1) equilateral triangles, with the three sides lying along cleaved (110) planes; 2) trapeziums; 3) parallelograms (Figure 2-7).

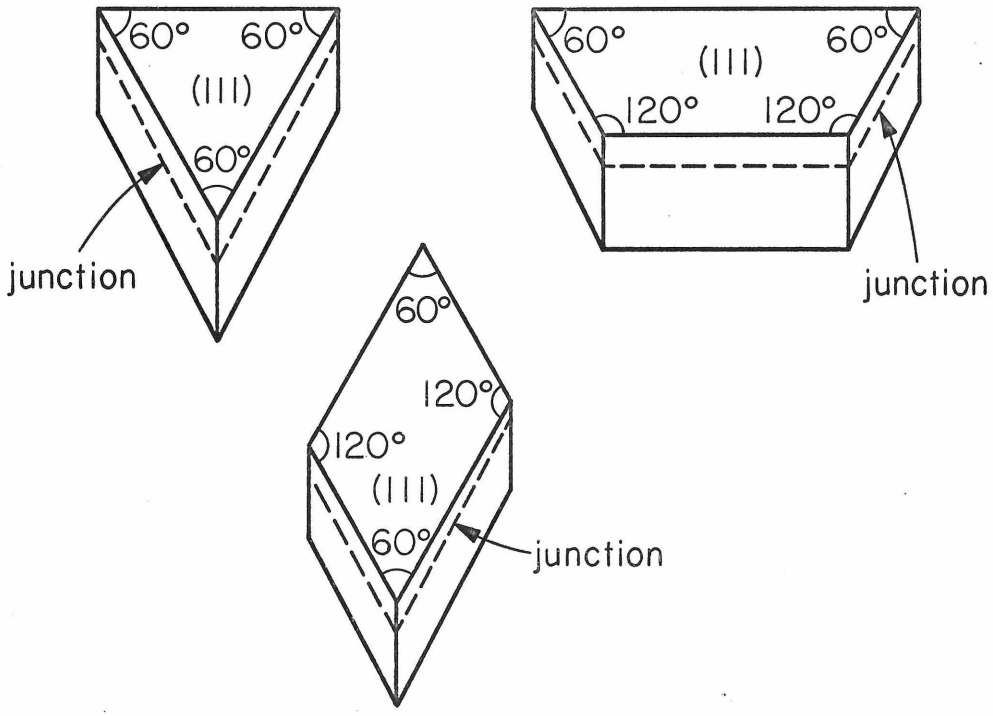

Figure 2-7. Laser Structures Cleaved from (111) InAs Wafer

c) In the case of the long cleaved bars, first the p layers were removed from the two opposite (100) faces by lapping so that the bars then looked as shown in Figure 2-8.

Each bar had two good junction planes near the two opposite cleaved (110) faces. By cleaving along a (110) plane parallel to these, right down the middle of the bar as shown in Figure 2-8, two bars, each with a junction plane in a (110) plane were obtained. Rectangular diode

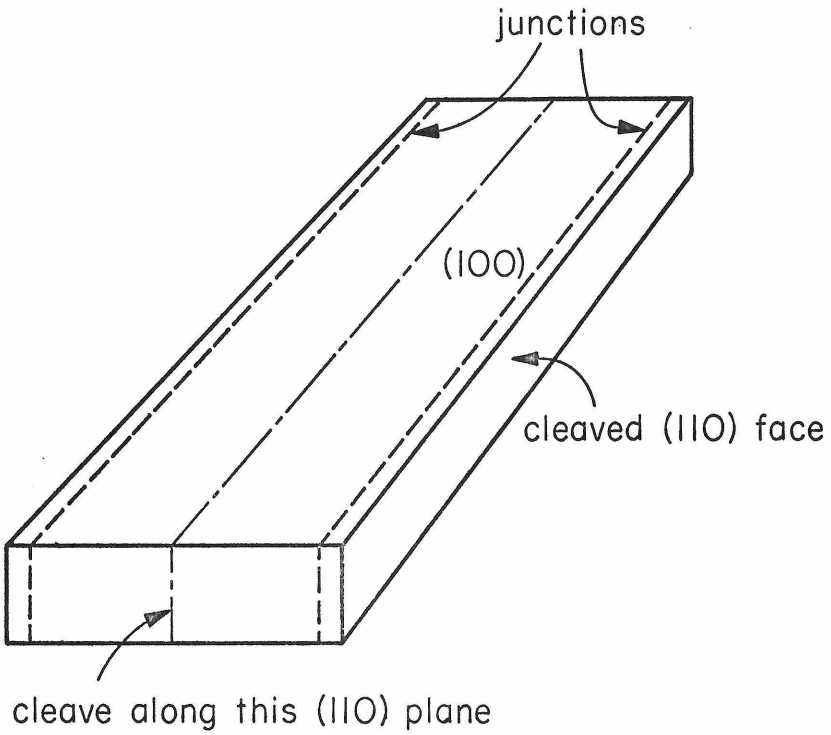

Figure 2-8. Cleaving Configuration of (100) Bars of InAs

cavities were obtained from these by cleaving along the other set of (110) planes.

In all the above cases, during the removal of the p-layer by lapping, the material type and thickness were carefully checked after small amounts of repeated lapping. In this manner the depth of the diffused layer was found to be in the range 1/2 $\sim$ 1 mil for the junctions obtained from the different diffusion runs.

2-5 The Formation of Electrical Contacts to the Diodes

In order for a p-n junction diode to exhibit its true current-voltage (I-V) characteristics the electrical contacts to the n and p sides of the diode must be ohmic in nature, i.e., the contacts should not by themselves exhibit rectification properties, and their

impedances must be small compared to that of the junction.

Several metals and alloys were tried in determining suitable ohmic contacts to n-type and p-type InAs. The metal-semiconductor pairs investigated are listed in Table 2-1.

Table 2-1

InAs impurity type	Contact material	Nature of contact
n	gold (film)	ohmic
n	In-Sn alloy	ohmic
n	In-Sn-Pb alloy	ohmic
p	gold (film)	non-ohmic
p	In-Sb alloy	non-ohmic
p	In-Sn-Pb alloy	non-ohmic
p	aluminum	non-ohmic
p	Ni-Au alloy (film)	ohmic
p	*Zn-Au alloy (film)	ohmic

*Suggested by Dr. C. Mead

All the contacts tried with n-type InAs were found to be ohmic, while with p-type InAs only the alloys (Zn-Au) and (Ni-Au) were found to be ohmic.

Because of its large bonding strength and low melting point (138^{o}C), In-Sn-Pb alloy was used as the contact to n-sides of the diodes. Since it was easier to alloy the Zn-Au film than the Ni-Au film to the p-type material, it was used for making contacts to the p-sides of the diodes. The procedure used to make the Zn-Au alloy film contact to the p-sides was as follows.

After the formation of a junction on all their surfaces by the diffusion of a p-type layer and prior to carrying out the lapping and cleaving procedure described in the previous section, thin films of zinc and gold, in that order, were deposited on the wafers. These samples were then subjected for a few seconds to a temperature of about 500°C in a hydrogen atmosphere. The Zn and Au would then run and alloy onto the p-type material. When this occurred, the surface would change its color from the golden one of Au film on top to a silvery-grey one of the alloy. The In-Sn alloy solder used to solder the wire making the electrical connection to the p-side did not run well and did not stick well to this alloy film, but it behaved very well on a gold film. So a gold film was deposited on top of the Zn-Au alloy film.

At this stage we had wafers and bars covered with film of ZnAu alloy and on top of that an Au film on all sides but one (this was the side facing down during the vacuum depositing of the films, and contained the junction which was to be lapped away). After this the lapping and cleaving procedures described in the previous sections were carried out so that the alloyed film remained as a contact only to the p-side of the diode cavity, but was present neither on the n-side nor on the sides of the diode cavity to act as an undesirable shunt across the p-n junction in the diode cavity.

These diode cavities were then soldered onto standard type TO-5 gold-plated transistor headers so that the finished product looked as

shown in Figure 2-9, except that the size of the diode in relation to that of the header has been greatly exaggerated for the sake of clarity.

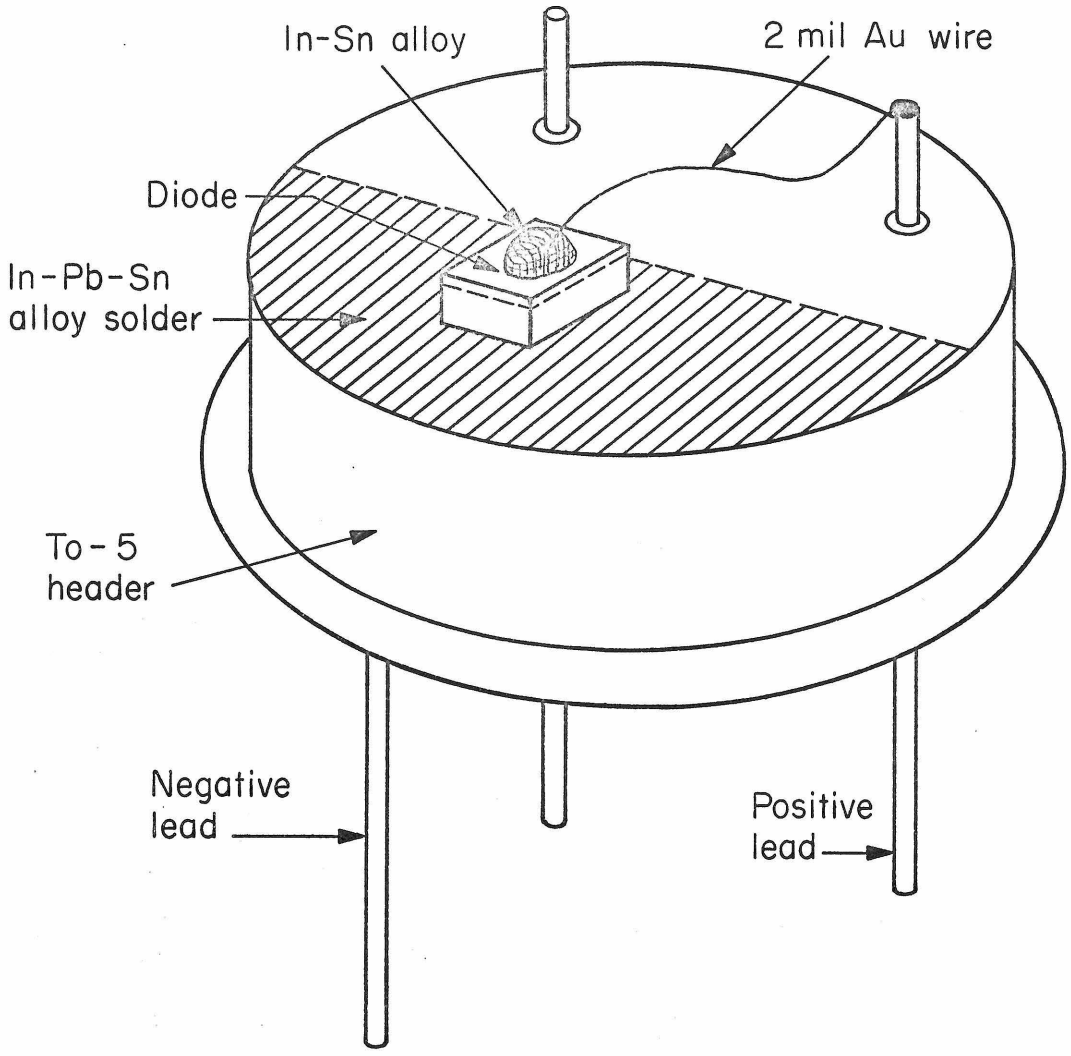

Figure 2-9. Diode Mounted on a TO-5 Header

Because of their extremely small sizes, the mounting of the diodes onto the TO-5 headers was a very tricky process. One had to be careful to see that the diodes were not shunted with the soldering material, or mechanically damaged with the extremely fine-pointed pair of tweezers used to handle them. The mounting involved several delicate steps carried out under a microscope, as described below.

The TO-5 header was held securely in a small vise, which was so placed that the top of the header could be viewed under a high magnification microscope. Before soldering the n-type diode base to the header the front half of the header surface was covered with a thin layer of In-Sn-Pb alloy (which had previously been demonstrated to form an ohmic contact to n-type InAs) using a special solder flux* and a very fine tipped 25 watt soldering iron. The gold plating on the headers allowed for a good flow of the solder over the surface, thereby forming a good metal to metal contact between the solder and header surface. After this the header was rinsed with methanol to remove the solder flux residue.

Using the same solder flux and holding the diode in place with a pair of finely pointed tweezers, the diode was soldered onto the In-Sn-Pb alloy layer. This was done by melting the alloy layer under the diode by holding the soldering iron so that it touched one side of the alloy layer (away from the diode) and then allowing it to

---

*Superior No. 30 Super Safe Soldering Flux.

resolidify by removing the soldering iron.

Thus a good semiconductor to metal ohmic contact was achieved between the n-side of the diode and the surface of the header. After this the diode and header were rinsed with methanol again to remove the solder flux residue.

On the p-side of the diode, we already had an ohmic contact formed by the alloyed Zn-Au film.
On top of this was the gold film which had been deposited to facilitate making a good contact with the In-Sn solder "dot" (m.p. 131^{o}C) used to solder a 2 mil gold wire connecting the p-side to a post on the header.

Prior to actual soldering to diodes, small ($\sim$ 0.1 mm diameter) In-Sn solder dots, with one end of a 1 cm long 2 mil gold wire attached to them, were formed from small flat pieces of the alloy cut from wire stock. A small piece of the solder was placed on a glass slide and then a 1 cm long 2 mil gold wire was placed on the slide so that one end of it rested on the flat solder piece. This piece and the end of the wire were then coated with the special solder flux. The solder piece was then melted by placing the fine tip of the soldering iron on the slide very close to the piece so that the glass underneath got locally heated. The melted solder immediately was transformed into a small sphere with the end of the gold wire sticking into it.

After allowing it to solidify, the solder sphere with the attached wire was rinsed with methanol of the flux residues. This sphere was placed in the center of the top surface of the diode (whose

bottom side, the n-side, was already soldered to the header surface), with the connecting wire bent in such a manner that its free end rested on the far side of the header surface (not touching the In-Sn-Pb solder layer (Figure 2-10). The sphere was then barely moistened with the solder flux. It was then melted by placing the tip of the soldering iron onto one side of the header surface; on resolidifying it bonded itself to the gold-film on top of the p-side of the diode. The free end of the connecting wire was then soldered to one of the gold-plated contact pins, thereby completing the electrical connection of the diode to the header, the result being the finished product shown in Figure 2-9.

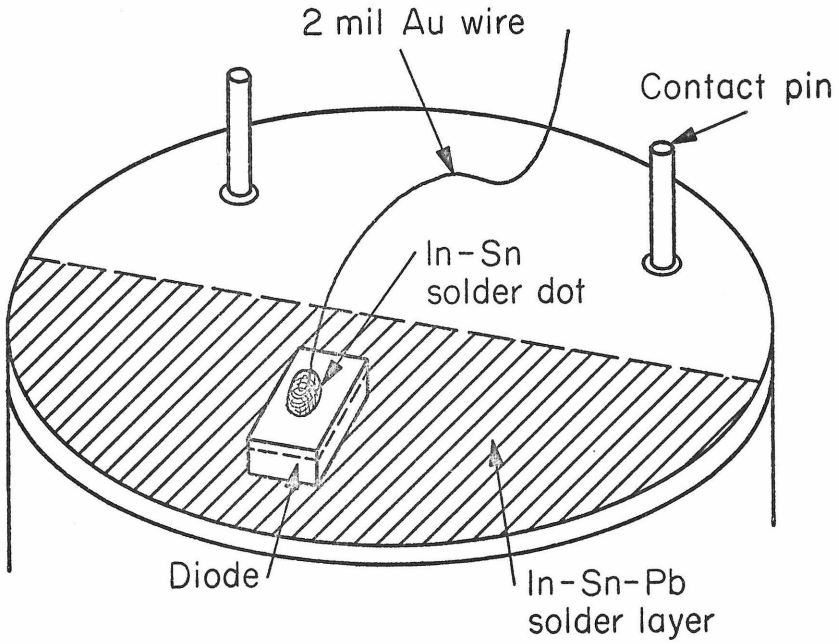

Figure 2-10. Configuration for Completing Electrical Connection to N-side of Diode.

Chapter III

Current Injection Mechanism

3-1 General Remarks

The aim of the present chapter is to present the observed current-voltage (I-V) data of the InAs diodes at various temperatures and to determine the current injection mechanism(s) responsible for the observed behavior. Corroborative data, such as total light intensity vs. current, capacitance vs. voltage, peak of spectral output vs. current, supporting the proposed model of current injection are also presented.

Before presenting the actual data, salient features of the apparatus and data acquisition systems used to obtain the experimental data will be presented below.

3-2.1 I-V data:

The experimental scheme used to obtain the current-voltage (I-V) characteristics of the InAs diodes is illustrated in fig.(3-1). As indicated in the diagram, current pulses (5 microseconds) were used for these measurements. The use of short current pulses prevented the heating up of the diodes at the higher current levels. The I-V data were obtained with the diodes submerged in liquid helium ($4.2^{o}K$), liquid hydrogen ($20.4^{o}K$), liquid nitrogen ($77^{o}K$), acetone-solid CO_2 ($195^{o}K$) and with the diodes at room temperature ($300^{o}K$).

3-2(2) C-V data:

The experimental arrangement used to obtain the differential capacitance (C) as a function of applied dc bias (V) is illustrated in fig. (3-2). The C-V data were obtained at $77^{o}K$ and $20.4^{o}K$.

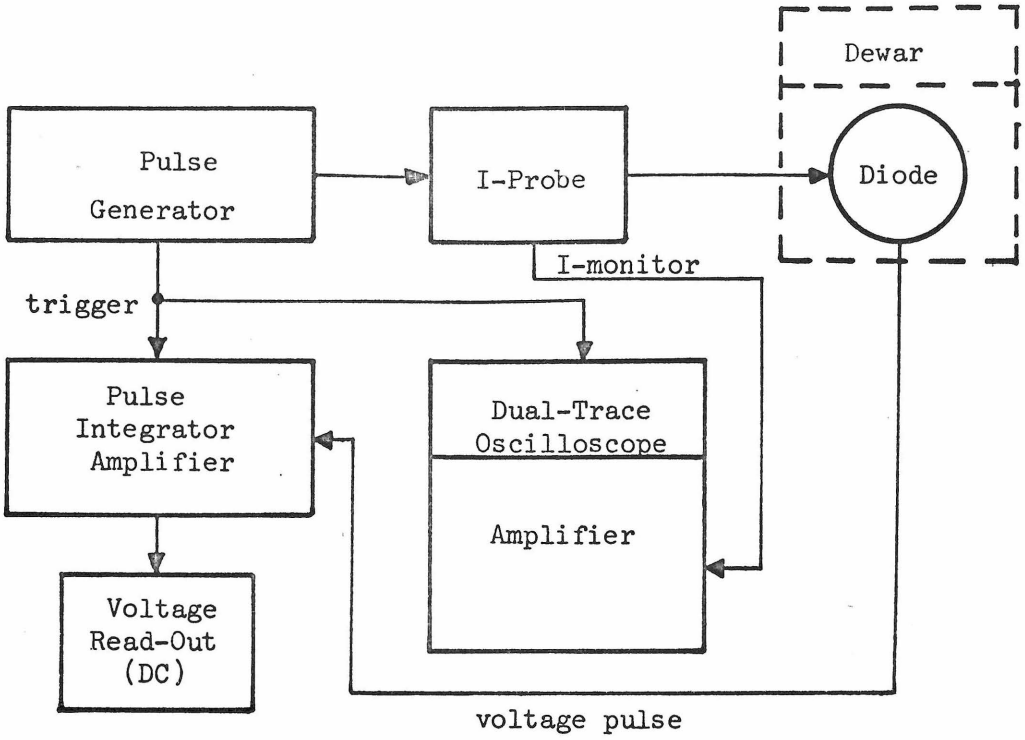

Figure 3-1. I-V Data Acquisition Scheme.

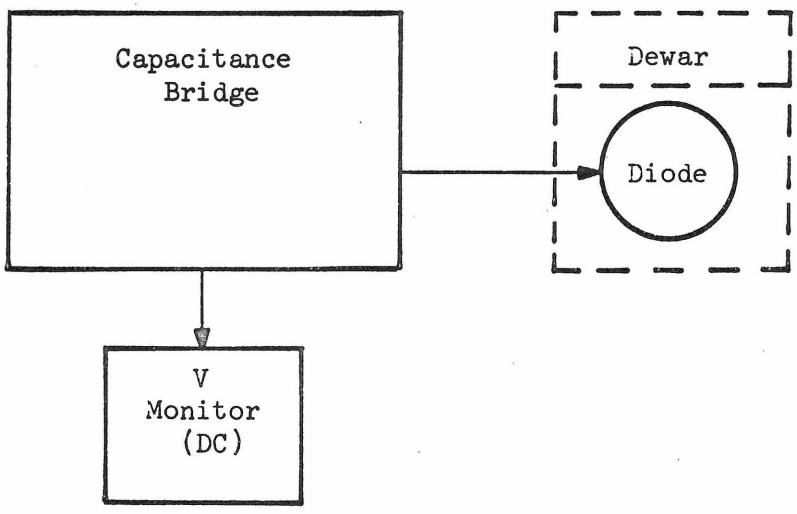

Figure 3-2. C-V Data Acquisition Scheme

3-2(3)$\mathcal{I}$ - I data:

The experimental set-up used to obtain the total radiation intensity ($\mathcal{I}$) as a function of diode current (I) is illustrated in Figure 3-3. The diode is mounted adjacent to the detector and both are submerged in a cryogenic liquid. A Ge:Hg (mercury doped germanium) detector was used to gather the data at 20.4°K and 4.2°K, while at 77°K, the detectors used were PbSe and Ge:Au.

All these detectors are photoconductive detectors and their use was necessitated by the requirement that the detector used be sensitive to wavelengths longer than 3μ and also that the detector be able to respond to pulses as short as a microsecond or less.

The basic scheme for light detection with a photoconductive detector is shown in Figure 3-4. Following the notation of Figure 3-4 the ratio of photo-induced change in voltage (ΔV) to the applied dc voltage (V_o) is given by

$$\frac{\Delta V}{V_o} = \frac{-R_L \Delta R}{(R_L + R_D)^2}\left[1 + \frac{\Delta R}{(R_L + R_D)}\right]^{-1} \qquad (3\text{-}1a)$$

where R_D is the dark resistance of the detector, and R_L is the load resistor. The quantity ΔR is the detector resistance modulation due to photo-excitation, given by

$$\frac{\Delta R}{R_D} = -\frac{\Delta n}{n_o}\left[1 + \frac{\Delta n}{n_o}\right]^{-1} \qquad (3\text{-}1b)$$

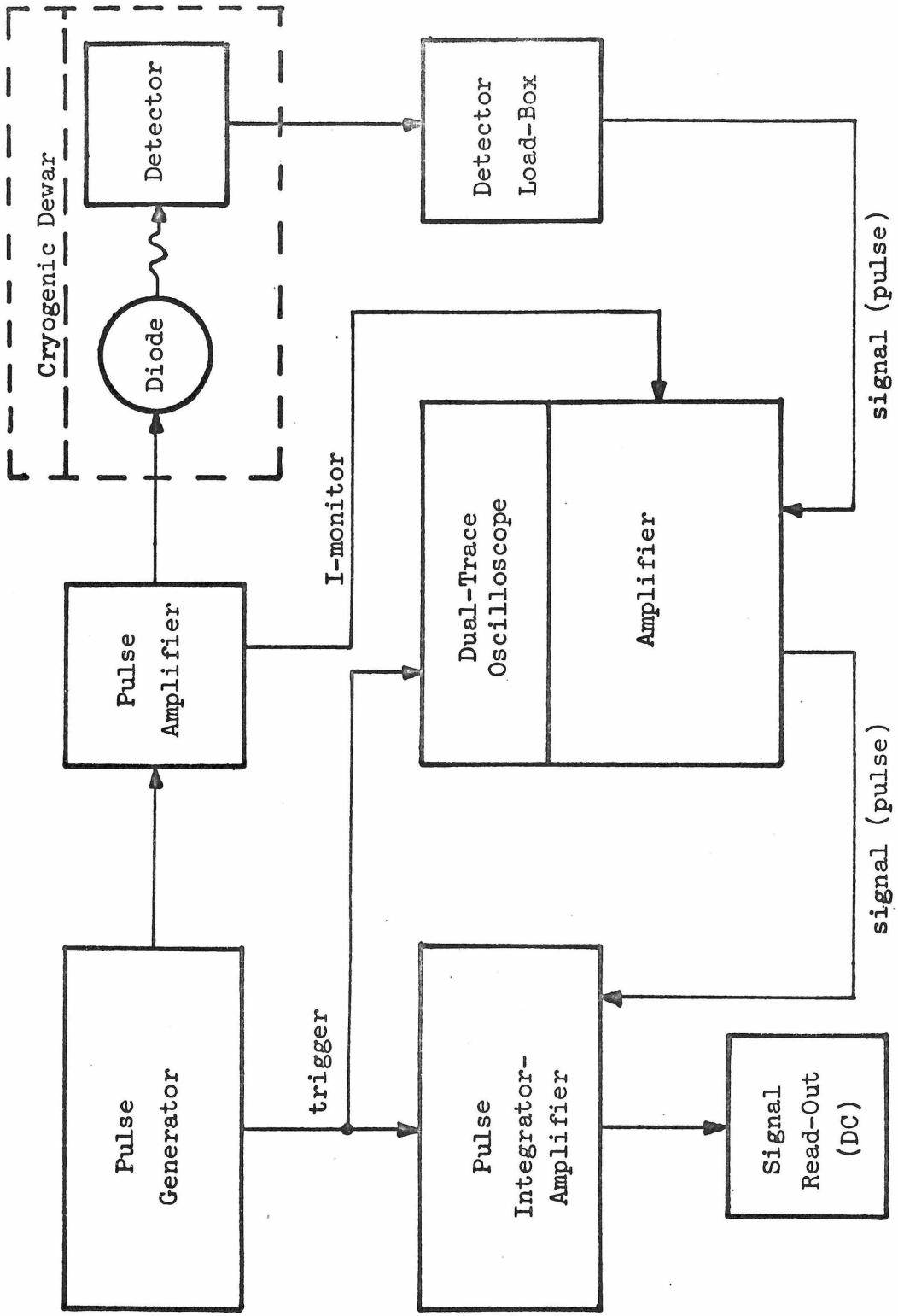

Figure 3-3. ϑ-I Data Acquisition Scheme

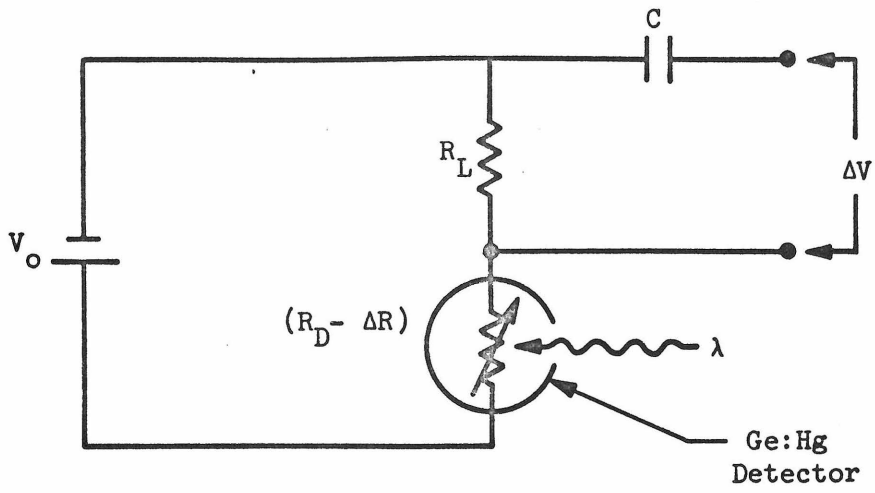

Figure 3-4. Ge:Hg Detector and Circuit

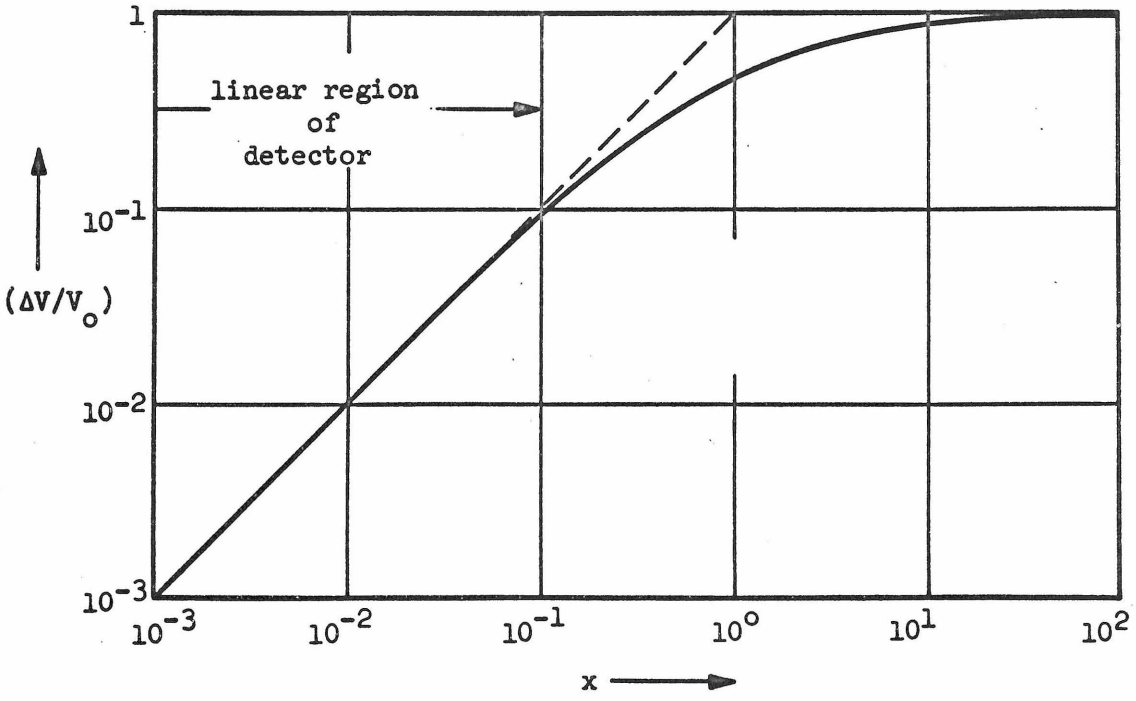

Figure 3-5. Detector Linearity

Here n_o is the unilluminated charge carrier population and the quantity Δn is the change in the charge carrier population due to photon absorption, and is given by

$$\Delta n = \eta_D \, G \, \phi \, \tau \tag{3-1c}$$

where G is the geometrical photon-loss factor*, τ is the carrier recombination life-time, ϕ is the total number of photons emitted per second and η_D is the detector (external) quantum efficiency (i.e. the number of carriers produced per photon intercepted by the detector). Now for $R_L \ll R_D$, the expression 3-1a becomes

$$y \equiv \frac{\Delta V}{V_o} = \frac{x}{1 + x} \tag{3-2a}$$

where

$$x \equiv \frac{R_L}{R_D} \cdot \frac{\Delta n}{n_o} \tag{3-2b}$$

$$\text{i.e.} \quad x \sim \phi \tag{3-2c}$$

The function 3-2a, plotted in Figure 3-5 determines the region of linear response of the detector system, i.e. the region where $\Delta V \sim \phi$. As seen from Figure 3-5 the detector remains linear up to signal voltages (ΔV) of magnitude $0.1 \, V_o$. (This is a very convenient method of testing for detector linearity, i.e. by merely monitoring $\Delta V / V_o$).

For $R_L \ll R_D$ we may write

$$\Delta V = \eta_D \, G \, R_L \, (^{q\tau}/_{\tau} t) \, \phi \tag{3-3a}$$

---

* The geometrical loss factor (G) is just the solid angle subtended by the light emitting surface at the detector, divided by 2π .

where

$$\tau_t \equiv \ell^2/\mu_n V_o \qquad (3\text{-}3b)$$

is the mobile charge transit time in the detector, ℓ is the distance between the contacts on the detector and μ_n is the carrier mobility in the detector material. If all these parameters for a detector are known then we can measure the photon flux ϕ received by it, through relation (3-3).

We may therefore express the external quantum efficiency of a light emitting diode (i.e. the number of photons emitted per charge carrier crossing the junction) as

$$\eta_d = \frac{\phi}{I} = \frac{\Delta V}{\eta_D G I R_L} \left(\tau_t/\tau\right) \qquad (3\text{-}4) .$$

where I is the total current flowing through the diode. If we wanted the differential external quantum efficiency then we would use $\frac{d(\Delta V)}{dI}$ in place of $\frac{\Delta V}{I}$ in the above expression.

3-2(4) Spectral intensity data:

The spectral intensity $\mathcal{S}(\lambda)$ of the stimulated and spontaneous emission from InAs diodes was measured with the system outlined in Figure 3-6. The spectra were obtained from diodes in contact with cryogenic baths of liquid hydrogen ($20.4^{\circ}K$) and liquid nitrogen ($77^{\circ}K$). The diodes were attached to a special "cold-finger" which was mounted on a cryogenic dewar. As before, the diode current consisted of short (1 ~ 10 microsecond) pulses to prevent excessive heating of the diodes. Special lenses made from arsenic-trisulphide (As_2S_3) were used because of their required infrared transmission characteristics. The spectrometer shown in the illustration contains a diffraction grating, blazed

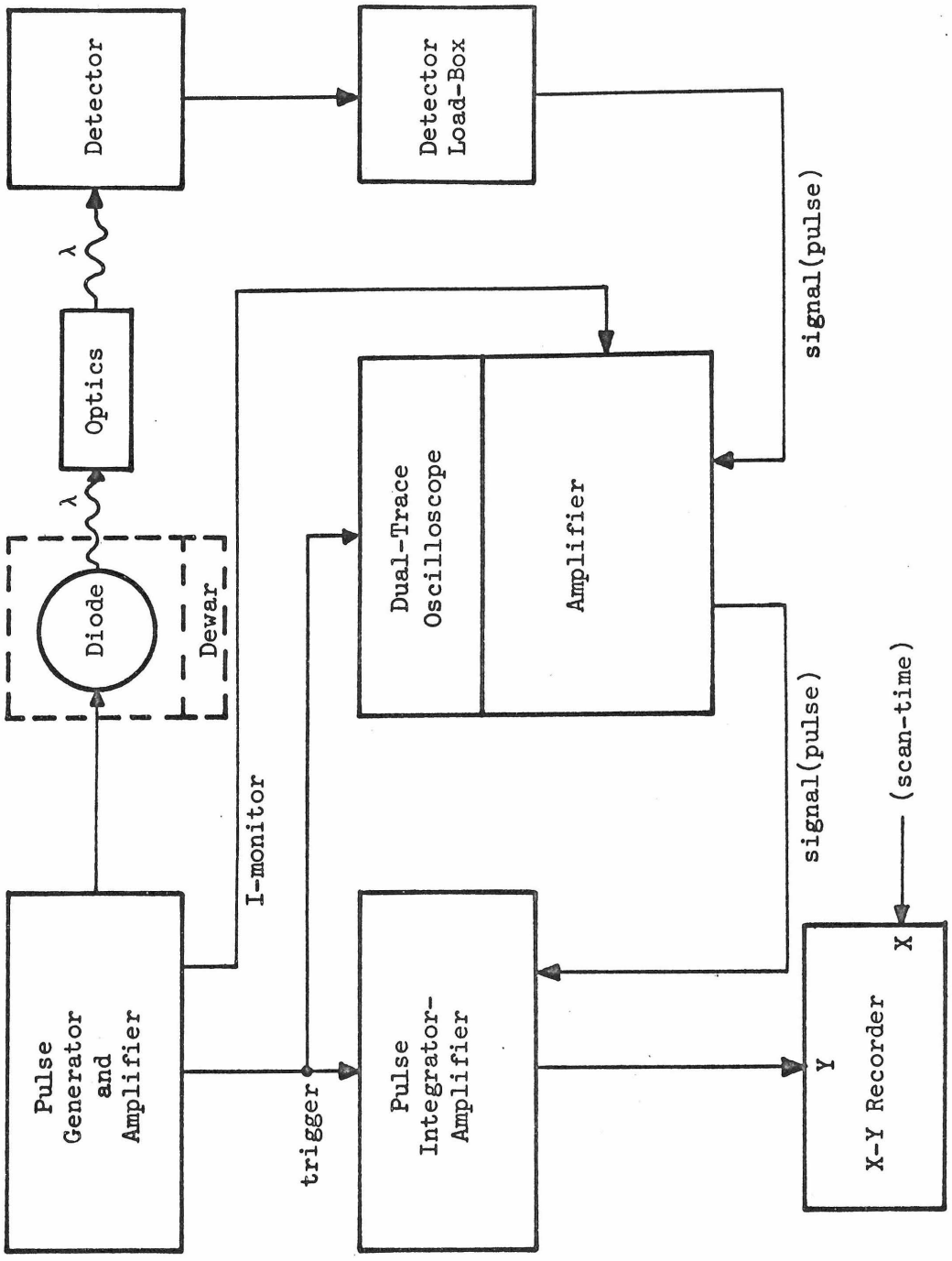

Figure 3-6. (a) $\mathcal{G}(\lambda)$ Data Acquisition Scheme (Electronics)

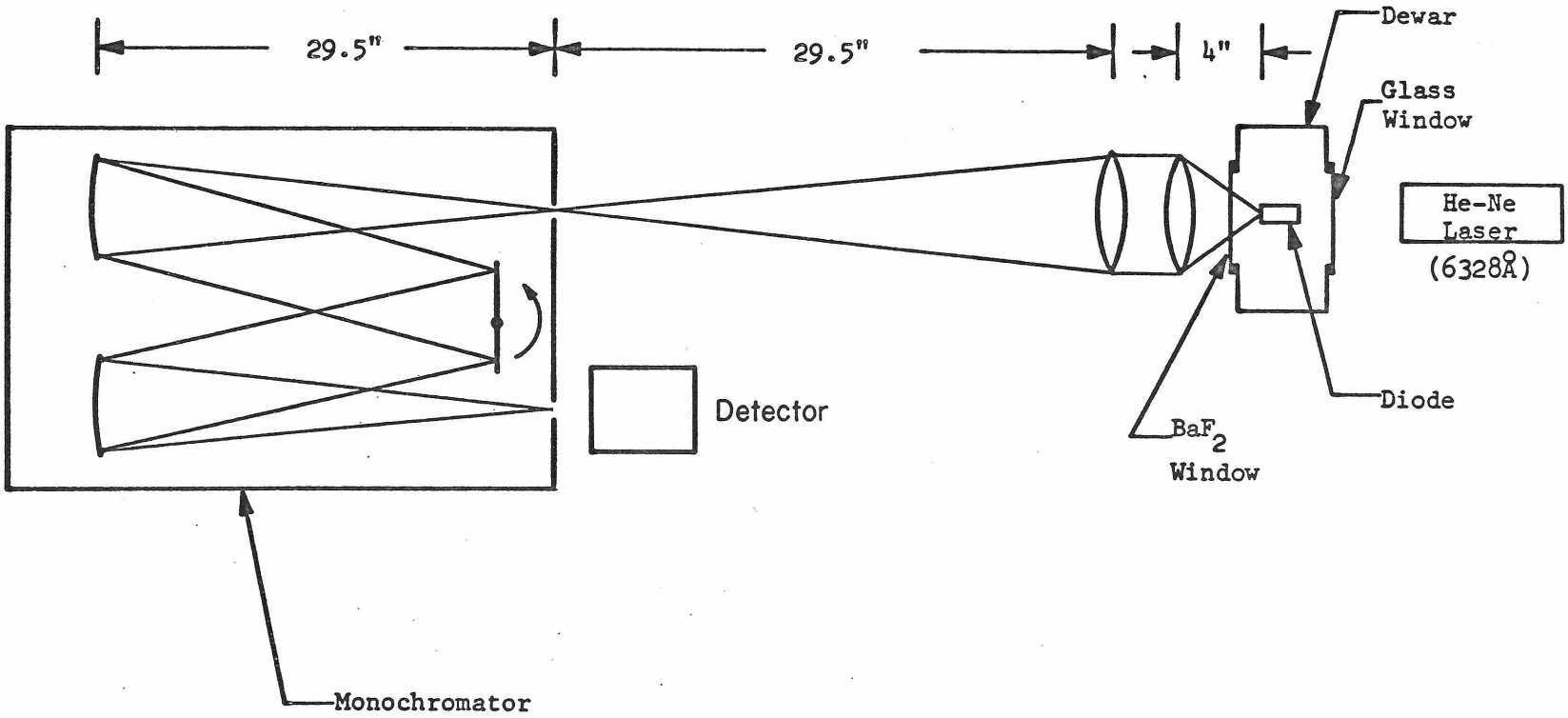

NOTE: Lenses are made of As_2S_3

Figure 3-6. (b) $\mathcal{S}(\lambda)$ Data Acquisition Scheme (Optics)

for $\lambda = 6\mu$, which was used in the second order. Alignment of the optical system and the diodes was accomplished with the use of a commercial He-Ne gas laser ($\lambda = 6328^{o}A$).

3-3 Experimental Data and discussion:

Measurements of the differential junction capacitance (C) as a function of applied (DC) voltage (V) are illustrated in Figure 3-7 for diode J_4 at $77^{o}K$. The linear relationship between $1/C^2$ and V indicates that the InAs diodes have abrupt junctions.

From relation (1-10), we see that the slope S of the line should give us

$$S = \frac{d}{dV}\left(1/C^2\right) = -\frac{W_1^2}{\epsilon^2} \qquad (3\text{-}3).$$

Hence

$$W_1 = \epsilon\left[|S|\right]^{\frac{1}{2}} \qquad (3\text{-}4).$$

The value of the width constant W_1 determined from the graph is

$$W_1 = 1.64 \times 10^{-5} \text{ cm Volt}^{-\frac{1}{2}} \qquad (3\text{-}5).$$

In Figure 3-8 are shown the forward bias current voltage characteristics of diode J_4 at $77^{o}K$, $20.4^{o}K$ and $4.2^{o}K$. Etching experiments and measurements of current versus area for other diodes made from the same sample indicated that the currents were not due to surface leakage around the junction of the diode. The data indicate that in the range in which the data points have been connected with straight lines, there exists an exponential dependence of current on voltage,

$$\text{i.e. we have } I \sim \exp(S_T V) \qquad (3\text{-}6).$$

It is seen that the same value of the (natural) logrithmic slope,

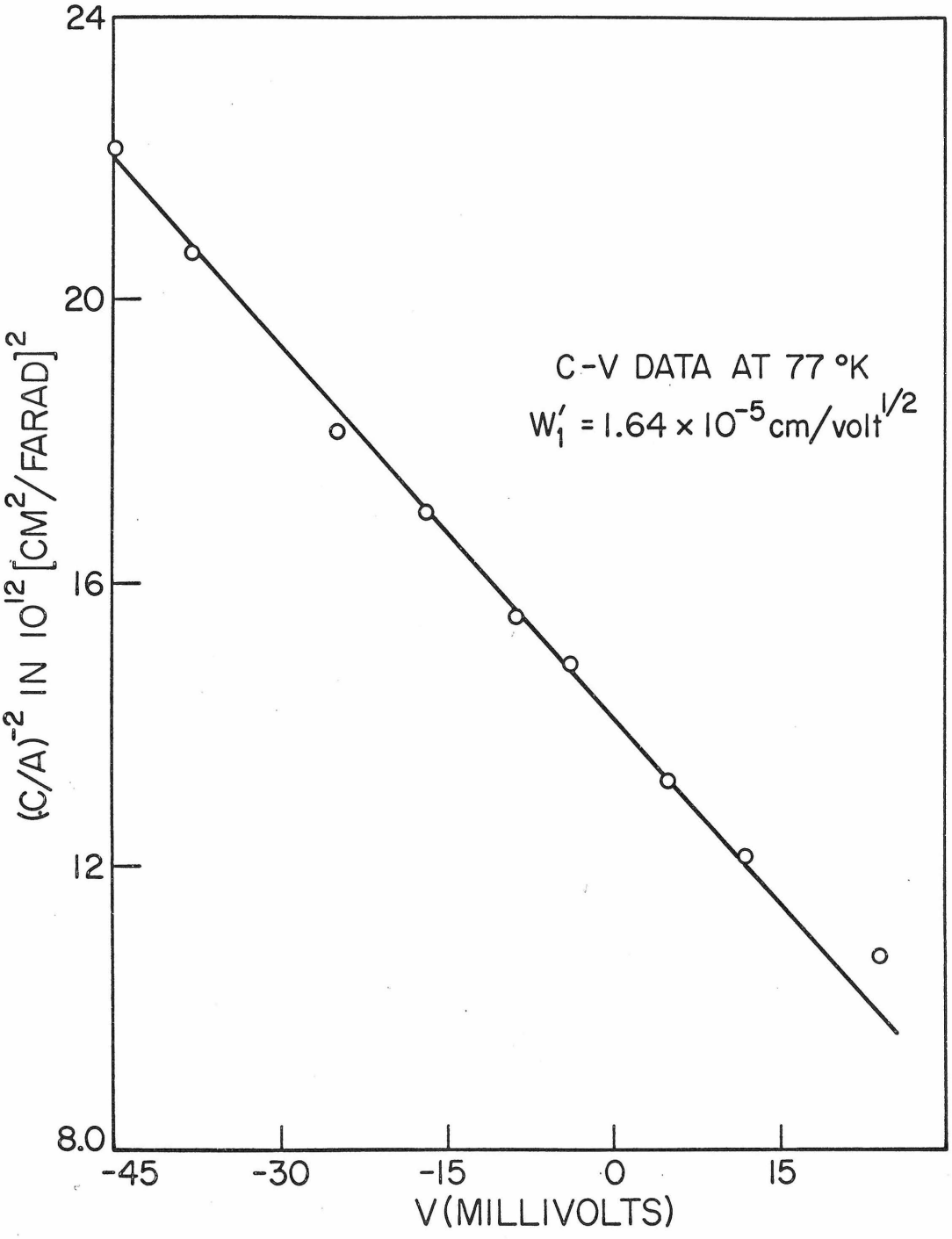

Figure 3-7. C-V Data for Diode J_4

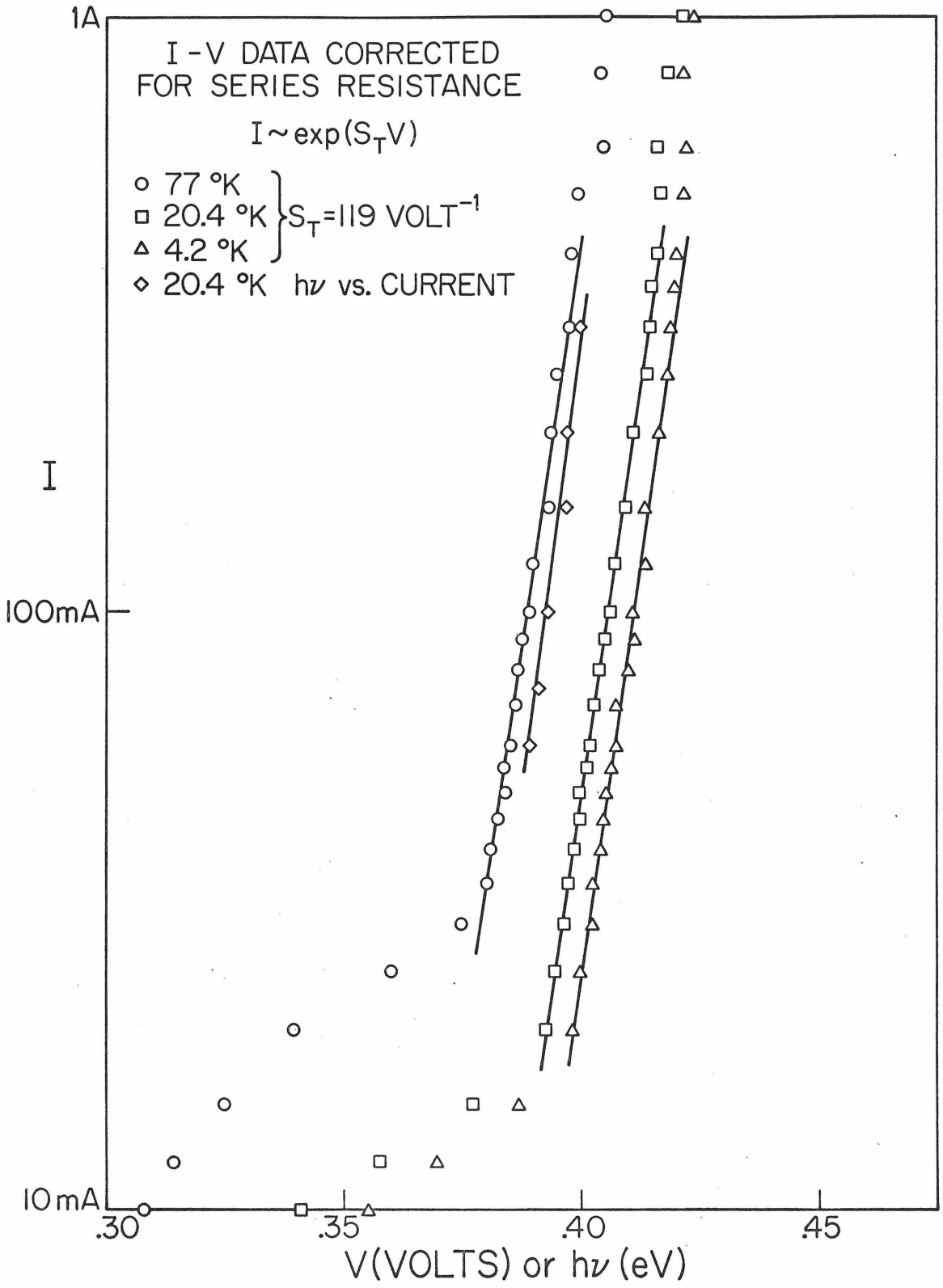

Figure 3-8. I-V Data for Diode J_4

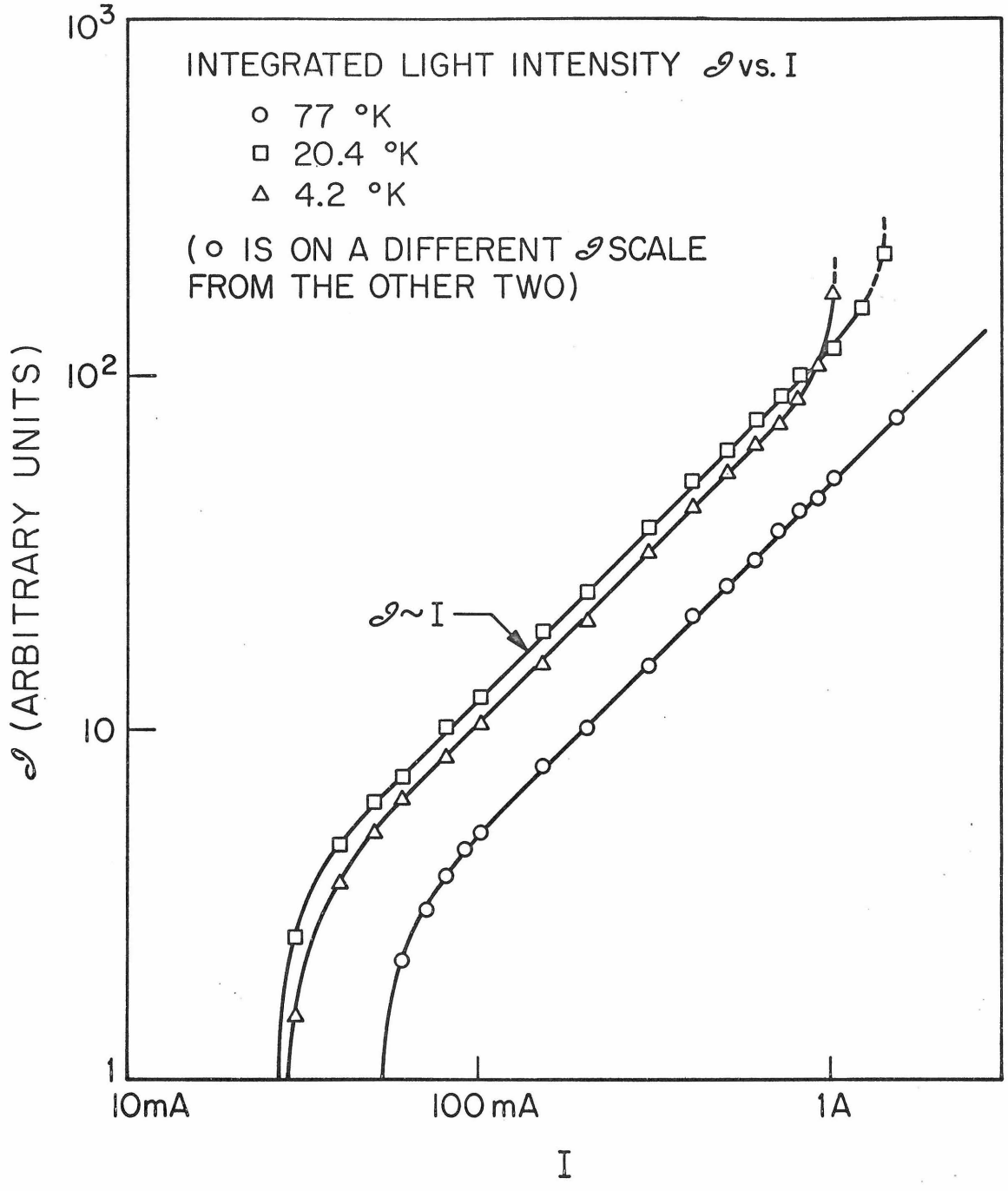

Figure 3-9. 𝒥-I Data for Diode J_4

$$S_T = 120 \text{ volt}^{-1} \tag{3-7}$$

is obtained for all the three temperatures. It therefore appears that the current is not thermionic in nature since the exponential coefficient would then be inversely proportional to the absolute temperature, as indicated by equation 1-11. In addition the slope ($^{q}/_{KT}$) for thermally generated current flow has the values of 150/volt, 570/volt, and 2760/volt for temperatures of 77°K, 20.4°K and 4.2°K respectively.

Figure 3-9 shows a plot of integrated light intensity $\mathcal{I}$ vs. current I for the diode J_4 in the range of currents under discussion and for the three aforementioned temperatures. It is seen that $\mathcal{I}$ is proportional to I, i.e. we have

$$\mathcal{I} \sim I \tag{3-8}$$

We had seen (expression (3-6)), that the current in this region followed the relation

$$I \sim e^{S_T V} \tag{3-6}$$

Hence we have

$$\mathcal{I} \sim e^{S_T V} \tag{3-9},$$

where S_T is independent of temperature.

This is as predicted by the model for photon-assisted tunneling of carriers. Since the model shows one photon emitted for each electron-hole pair tunneling into the junction, the intensity of the emitted light should be proportional to the tunneling current, and should have the same temperature independent dependence on the applied bias. The calculated value of S_T[using relation 1-12b, which follows from model]

using the value of W_1 obtained from the capacitance-voltage data is

$$S_{T_{calc.}} = 105 \text{ volt}^{-1} \tag{3-10}$$

in fair agreement with the measured value. We had observed in the discussion on photon assisted tunneling in Chapter I, that the peak $h\nu_p$ of the emitted radiation should approximately follow the applied voltage V, according to the relation

$$h\nu_p \cong qV. \tag{1-13}$$

In Figure 3-8, together with the I-V data, are also shown data points for I vs $h\nu_p$ at 20.4°K. We see that the points lie on a straight line with very nearly the same slope as the I-V characteristics, and moreover the line lies fairly close to the characteristic for 20.4°K, so that relation (1-13) is seen to be obeyed.

In Figure 3-10 are shown for the same diode J-4, characteristics at 300°K and 195°K. The measured values for the logarithmic slopes at these two temperatures are 36 volt^{-1}(at 300°K) and 55 volt^{-1} (at 195°K). These agree very well with the calculated slopes ($^{q}/_{KT}$) for thermally generated current, which have the values 39 volt^{-1} at 300°K and 59 volt^{-1} at 195°K. Thus we see that while at the temperature of 77°K and below the current due to photon-assisted tunneling dominates in a certain region of bias, at 195°K and above the dominant current injection mechanism is thermionic for all biases. An approximate value of the temperature T_{trans}, at which the transition from one kind of mechanism being dominant to the other being dominant could be expected to take place, can be determined by equating the logarithmic slope

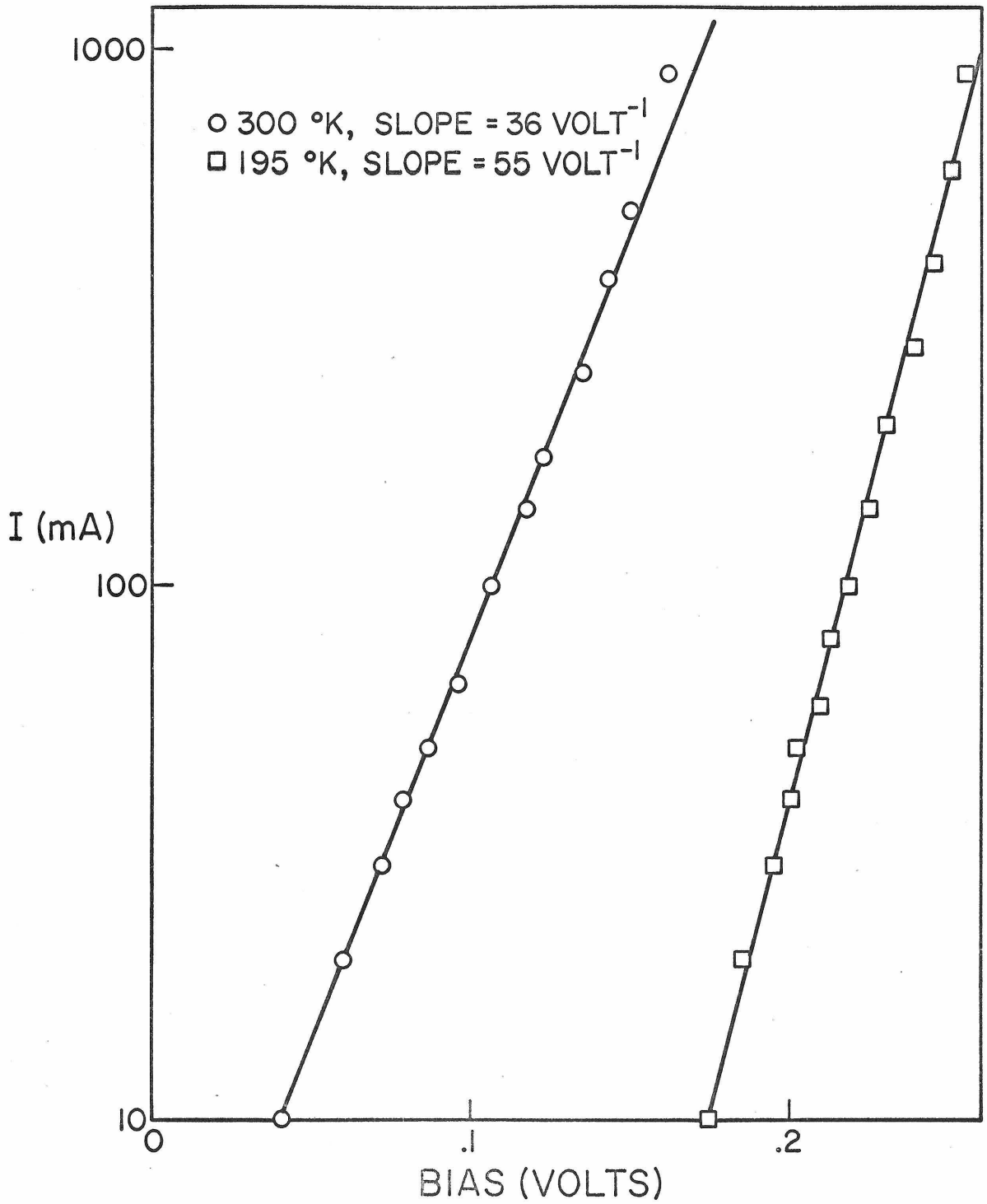

Figure 3-10. I-V Data for Diode J_4 at 300°K and 195°K

constants for the two cases:

$$\frac{qV}{kT_{trans}} = S_T V \qquad (3\text{-}11a)$$

$$\text{i.e.} \qquad T_{trans} = \frac{q}{kS_T} \qquad (3\text{-}11b).$$

Substituting the value of $S_T = 120\ \text{volt}^{-1}$ for the diode under consideration, we get $T_{trans} = 100^{\circ}K$, which is gratifying in that it lies between $77^{\circ}K$ and $195^{\circ}K$.

Figure 3-11 shows a curve tracer display of the I-V characteristic of diode K_9 at $77^{\circ}K$. For forward bias voltages the display is seen to extend up to 350 mV; we see from the logarithmic plot of the I-V curve in Figure 3-12, that it is just around this bias (the current being approximately 100 mA) that the current due to photon-assisted tunneling of carriers (the data points connected by the straight line) becomes the dominant current carrying mechanism. Also from Figure 3-13, which shows a plot of total integrated light intensity v.s. the current I, we see that above a current of 100 mA (at which point as we saw above, photon-assisted tunneling becomes the dominant mechanism for current injection), $\mathcal{S} \sim I$, while below 100 mA, $\mathcal{S}$ drops off very rapidly with decreasing current.

The I-V characteristic displayed in Figure 3-11, looks quite similar to that obtained during direct horizontal band to band (non-radiative) tunneling in narrow junctions for low values of biases (Figure 1-6).

With the aid of the plots in Figures 3-12 and 3-13 we can show

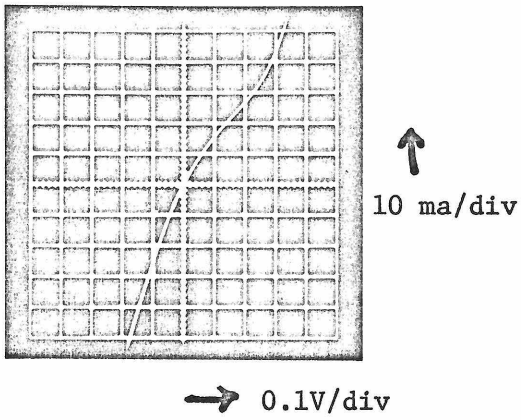

Figure 3-11. Curve Tracer Display of I-V Characteristic of Diode K_9 at $77^{o}K$

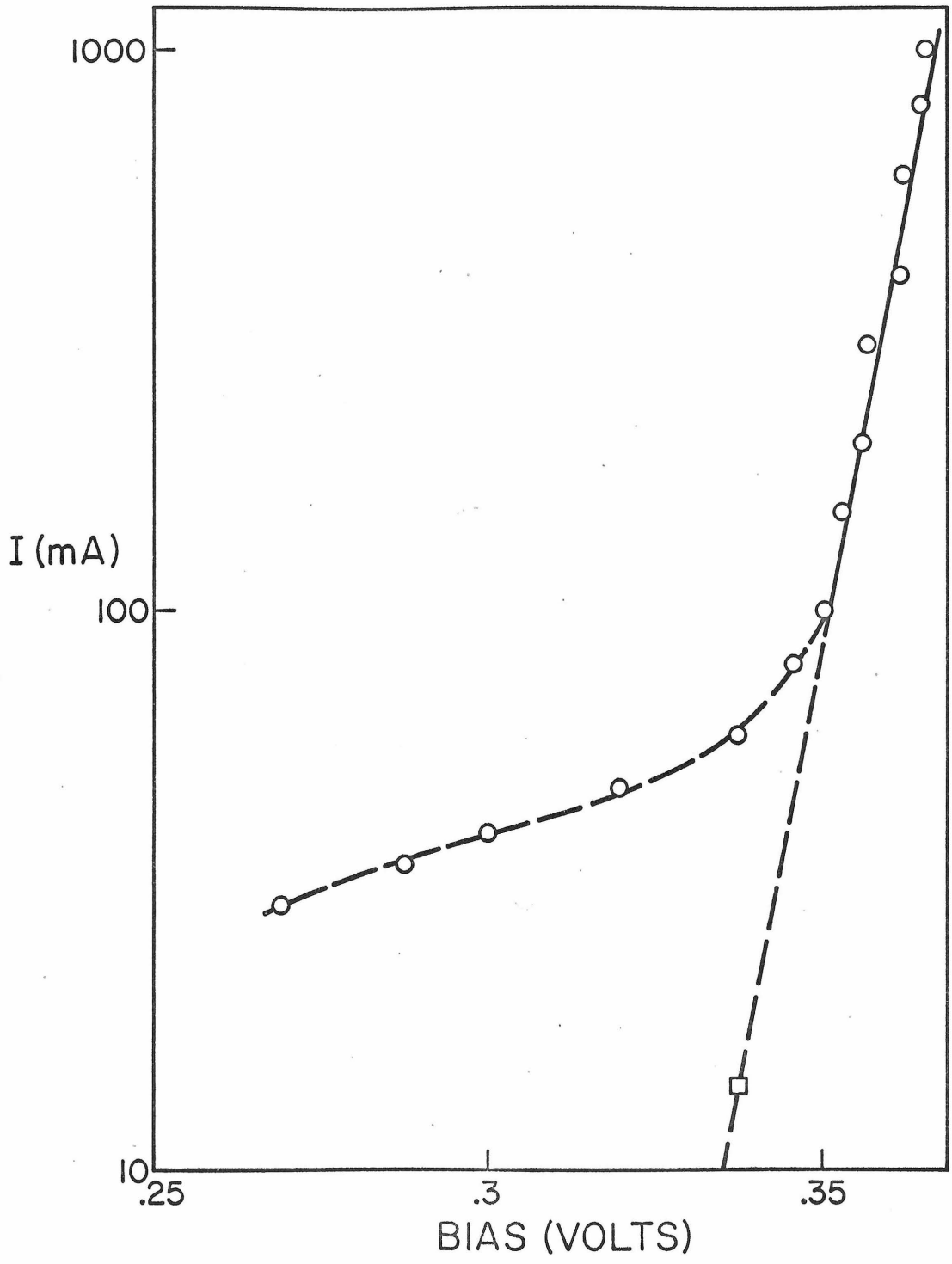

Figure 3-12. I-V Data of Diode K_9 at 77°K

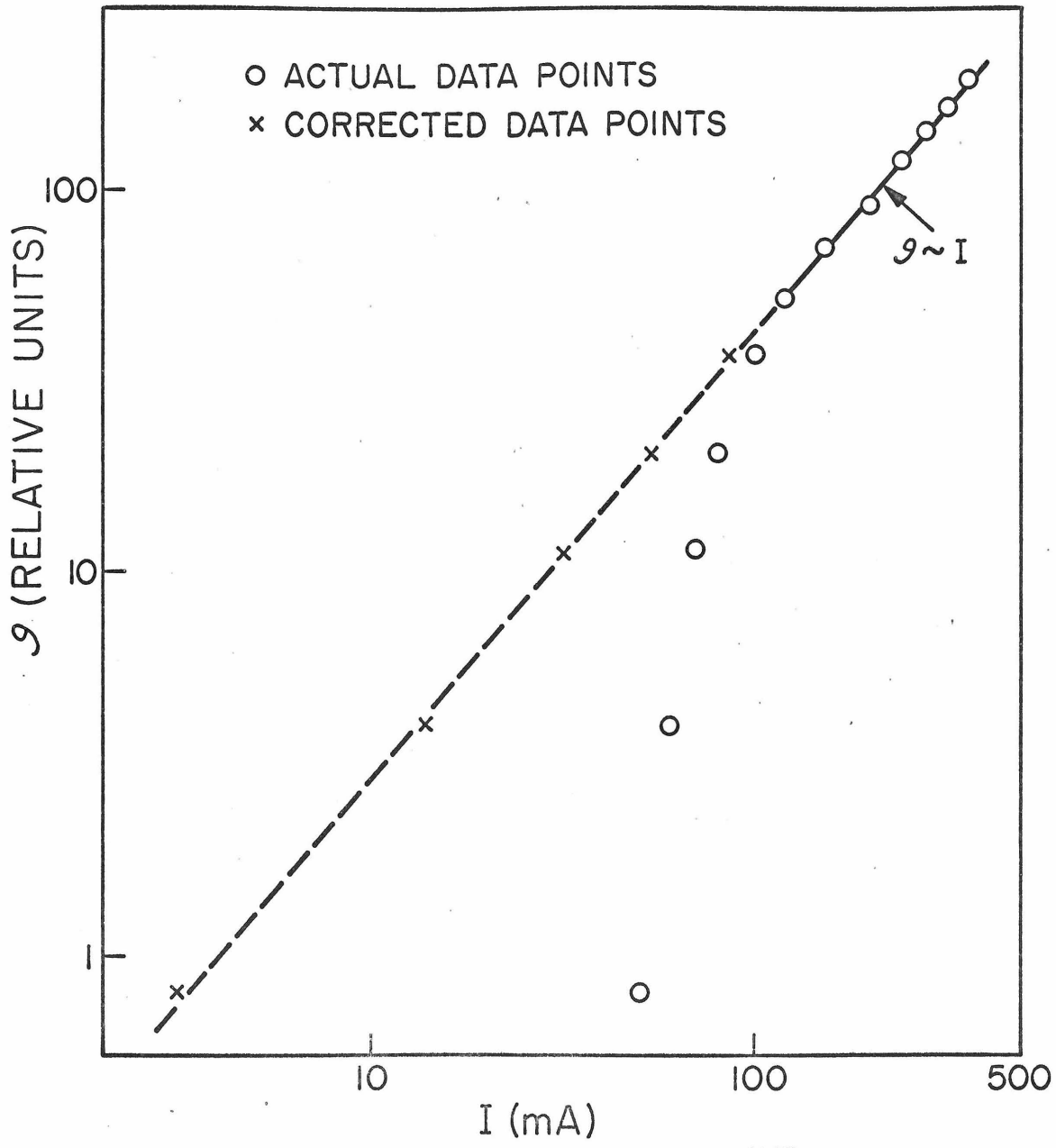

Figure 3-13. 9-I Data of Diode K_9 at 77°K

that the dominant current injection mechanism, below a current of 100 mA, is non-radiative (or if it results in any radiation, the emitted photon wavelength exceeds 15μ, which was the long-wavelength limit of the detector used). In Figure 3-12 if we extrapolate the straight line (which connects the data points in the region in which photon-assisted tunneling is the dominant injection mechanism) to currents below 100 mA, then for a given value of the current we can determine what fraction of it is due to photon-assisted tunneling. For example we see that at a bias of .338 volts, the actual current is 60 mA, while the straight line crosses this bias at 14 mA, so that out of a total current of 60 mA, 14 mA is due to photon-assisted tunneling. Now, on the $\mathcal{P}$ vs I plot in Figure 3-12, if we plot $\mathcal{P}$ vs the current due to photon-assisted tunneling (instead of the actual total current), we get the points shown by 'x's. We see that these points fall right on the extension of the straight line joining the points for currents above 100 mA, where $\mathcal{P} \sim I$ and all the current and radiation is due to photon-assisted tunneling. Thus we see that even below a current of 100 mA, all the radiation can be accounted for by that component of the current which is due to photon-assisted tunneling, so that the current injection mechanism responsible for the rest of the current must be non-radiative. This mechanism may be direct band to band tunneling as discussed in Chapter I, or tunneling via impurity levels in the gap as illustrated in Figure 3-14. What is more probable is that it is a combination of both, the first dominating at lower biases and the second at higher biases, before they are both swamped by the photon-assisted tunneling mechanism. The fact that the mechanism responsible is of a

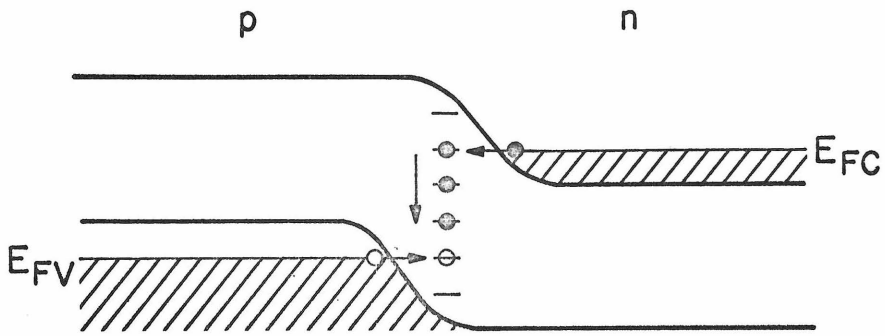

Figure 3-14. Model for Radiationless Diagonal Tunneling via Impurity Levels

tunneling kind is supported by the evidence that the I-V characteristics in this region at $77^{o}K$, $20.4^{o}K$ and $4.2^{o}K$, are almost totally independent of temperature.

Chapter IV

Threshold Current, Gain and Loss Coefficients, Superradiant Narrowing, Axial Mode Distribution and Stimulated External Quantum Efficiency

4-1 Lasing Threshold and Gain and Loss Coefficients

We saw near the end of the discussion of Chapter I that at sufficiently high applied voltage there is an active region in the vicinity of the junction where the carrier population is inverted. Associated with the stimulated emission produced by this population inversion is a gain in the active region, and the gain $\gamma(\nu)$ per unit length is directly proportional to the injection current density. For a photon field of frequency ν in a semiconductor diode, $\gamma(\nu)$ is given by [10]

$$\gamma(\nu) = \frac{c^2 \xi \eta}{8\pi \nu^2 qd} J\, g(\nu) \qquad (4\text{-}1)$$

where c is the velocity of light, η is the recombination quantum efficiency defined as the fraction of injected electrons which recombine radiatively, q is the electron charge, J is the injected current density, $\xi = 1 - (n_1/n_2)$ is the inversion factor, with n_2 and n_1 being the upper and lower energy level populations, d is the width of the region containing the electromagnetic modes in the cavity and $g(\nu)$ is the normalized line shape for the spontaneous emission from the diode.

Because the active region is generally quite thin (of the order of a micron), the maximum gain over a reasonable distance will be in the plane of the junction. This is the reason that the Fabry-Perot cavity,

formed by means of reflectors polished, or cleaved, directly on the semiconductor crystal, is extensively used so that the feedback path is directly in the plane of maximum gain. Coherent oscillations occur when the gain experienced by the radiation wave in a single pass between the reflectors is equal to the total loss incurred in the same distance

$$R\, e^{(\gamma-\alpha)L} = 1 \tag{4-2}$$

or

$$\gamma_{(\text{threshold})} = \alpha + \frac{1}{L}\, \ell n(\frac{1}{R}) \tag{4-3}$$

where α is the distributed loss coefficient per unit length, L is the length of the cavity and R is the reflectivity of the end surfaces of the cavity ($R < 1$ constitutes a loss mechanism). Substituting (4-1) into (4-3) the oscillation condition at line center (ν_o) becomes

$$\frac{c^2 \xi\, \eta}{8\pi \nu^2 q d\, \Delta\nu}\, J_{th} = \alpha + \frac{1}{L}\, \ell n(\frac{1}{R}) \tag{4-4}$$

where $\Delta\nu = g(\nu_o)^{-1}$ is the measured recombination line width. The threshold current density is then

$$J_{th} = \beta\, [\alpha + \frac{1}{L}\, \ell n(\frac{1}{R})] \tag{4-5}$$

where we have put the constant

$$\frac{8\pi \nu^2 q d\, \Delta\nu}{c^2 \eta\, \xi} = \beta \tag{4-6}$$

We can also rewrite (4-1) in terms β as

$$\gamma(\nu) = \frac{J}{\beta} \tag{4-7}$$

which shows explicitly that the gain is proportional to the injection current density.

We see from (4-5) that a convenient method for determining the loss coefficient α and the gain factor β is to measure the threshold current density for a series of lasers with different lengths but otherwise identical structures [11] . Such measurements were carried out on two groups of diodes at $20.4^{o}K$. The threshold currents were determined from plots of total light intensity against injected current as described in the last section of this chapter.

A comparison of different diodes is possible only if they are of uniform quality. This requires a uniform diffusion front as well as a uniform current distribution. The latter was achieved by using, as described in Chapter II, large area contacts covering the whole surface area on both the n side and the p side. To assure diffusion fronts as uniform as possible in a given group of diodes, batches of diodes of different lengths were made from small sections of larger wafers into which the Zn diffusion was made.

4-2 Superradiant Line Narrowing

The spontaneous recombination radiation from a p-n junction, emitted with a line shape $g(\nu)$, when passing through a distance z in the active medium gets amplified by a factor $e^{ag(\nu)z}$, where $ag(\nu) = \gamma(\nu)$ is the gain per unit length, a being a constant proportional to the degree of inversion of the population. Since $g(\nu)$ is usually a singly peaked function, the frequencies near the line maximum

are amplified more strongly than those further away, and consequently there is a narrowing of the emitted line. Although the narrowing is observable even before the current density reaches its threshold value, it starts becoming appreciable just around the point when the threshold conditions is reached. Then the diode cavity goes into coherent oscillations with the concomitant appearance of narrow-band mode structure in the spectrum of the emitted light. If, however, the optical feedback in the diode cavity is removed (e.g., by cleaving one of its ends at an angle to the other, or spoiling the reflectivity of its ends by roughening them) then the diode cannot go into coherent oscillations, even when driven above what would have corresponded to threshold, and the narrowing of the emitted line can be greatly accentuated. This kind of narrowing is referred to as "superradiant" narrowing and is characterized, as shown below for a Gaussian $g(\nu)$, by its square root dependence on the gain for high gain values

$$\frac{\delta\nu}{\Delta\nu} = \frac{1}{\sqrt{\gamma(\nu_o)L}} \qquad (4\text{-}8)$$

where $\gamma(\nu_o)$ is the exponential gain constant at line center, $\delta\nu$ is the width at half intensity of the externally observed radiation, $\Delta\nu$ is the half-width of the spontaneous emission line shape function $g(\nu)$, and L is the characteristic distance per single pass [4].

Let us now derive relation (4-8) for a Gaussian $g(\nu)$. The radiation emerging from a sample length ℓ and a distributed loss constant α is given by

$$F(\nu) = \int_0^{\ell} g(\nu)\ e^{[\gamma(\nu) - \alpha]x}\ dx \qquad (4\text{-}9a)$$

Integrating we get

$$F(\nu) = g(\nu)\ \frac{e^{[\gamma(\nu) - \alpha]\ell} - 1}{\gamma(\nu) - \alpha} \qquad (4\text{-}9b)$$

Here $F(\nu)$ is not normalized. For $\gamma(\nu_o)\ell << 1$, $F(\nu)$ = constant $\cdot$ $g(\nu)$. If $\gamma(\nu_o)$ is increased to a point where it becomes comparable yet smaller than α , $F(\nu)$ = constant $\frac{g(\nu)}{\alpha - \gamma(\nu)}$ which is, because of the frequency dependent denominator, narrower than $g(\nu)$. Thus we see that the narrowing is a gradual process, and the approximate requirements for the onset of narrowing are

$$\gamma(\nu_o)\ell \simeq 1 \qquad (4\text{-}10a)$$

$$\gamma(\nu_o) \sim \alpha \qquad (4\text{-}10b)$$

If we limit ourselves to the range where we are well past the onset of narrowing, so that

$$\gamma(\nu_o)\ell >> 1 \qquad (4\text{-}11a)$$

$$\gamma(\nu_o) > \alpha \qquad (4\text{-}11b)$$

the expression (4-9) for $F(\nu)$ reduces to

$$F(\nu) = e^{\gamma(\nu)\ell} \qquad (4\text{-}12)$$

Hence $$F(\nu_o) = e^{\gamma(\nu_o)\ell} \qquad (4\text{-}13a)$$

and $$F(\nu_{1/2}) = \frac{1}{2} F(\nu_o) = e^{\gamma(\nu_{1/2})\ell} \qquad (4\text{-}13b)$$

where $$2(\nu_{1/2} - \nu_o) = \delta\nu \tag{4-13c}$$

the half width of $F(\nu)$.

Combining these we get

$$\gamma(\nu_o)\ell = \ln 2 + \gamma(\nu_{1/2})\ell \tag{4-14}$$

For a Gaussian $g(\nu)$

$$\gamma(\nu) = a\, g(\nu) = \frac{a}{\sqrt{\pi}}\, e^{-4\left(\frac{\nu - \nu_o}{\Delta\nu}\right)^2 \ln 2} \tag{4-15a}$$

$$\gamma(\nu) = \gamma(\nu_o)\, e^{-4\left(\frac{\nu - \nu_o}{\Delta\nu}\right)^2 \ln 2} \tag{4-15b}$$

so

$$\gamma(\nu_{1/2}) = \gamma(\nu_o)\, e^{-\left(\frac{\delta\nu}{\Delta\nu}\right)^2 \ln 2} \tag{4-16}$$

$$\gamma(\nu_{1/2}) \simeq \gamma(\nu_o)\left[1 - \left(\frac{\delta\nu}{\Delta\nu}\right)^2 \ln 2\right] \tag{4-17}$$

Combining (4-14) and (4-17) we get the required expression (4-8)

$$\left(\frac{\delta\nu}{\Delta\nu}\right) = \frac{1}{\sqrt{\gamma(\nu_o)\,\ell}}$$

Using (4-7) to substitute for $\gamma(\nu_o)$ in terms of the experimentally controllable quantity J , the current density, we get

$$\frac{\delta\nu}{\Delta\nu} = \left[\frac{J\ell}{\beta}\right]^{-1/2} \tag{4-18}$$

From a plot of $\delta\nu/\Delta\nu$ against $J^{-1/2}$ a value of β can be obtained.

Measurements of the line widths as a function of different injection current densities were carried out on an InAs diode with a non-lasing structure. This unit was constructed by cleaving one of its ends in a (110) plane in the regular manner and the other end in a (111) plane. To do this, this end of the diode was first cleaved in a (110) plane. Then, after laying the diode down sideways on one of its rough sides, a blade was placed on the top corner containing the junction so that the plane of the blade roughly coincided with a (111) plane (making about 35^{o} with the (110) end). The blade was then tapped until the corner cleaved off, exposing the junction in a (111) plane. The finished cavity looked as shown in Fig. 4-1.

4-3 Spectral Separation of Stimulated Modes

The oscillating modes inside a Fabry-Perot cavity must satisfy the condition

$$\frac{m\lambda}{2n_r} = L \tag{4-19a}$$

i.e.,

$$m\lambda = 2Ln_r \tag{4-19b}$$

where m is an integer, the mode number, λ is the radiation wavelength in free space, L is the length of the cavity, and n_r is the index of refraction of the cavity material at wavelength λ. By differentiating this expression with respect to λ and setting $\Delta m = -1$, the separation in wavelength between adjacent modes can be shown to be [12]

$$\Delta\lambda = \frac{\lambda^2}{2Ln_r\left[1 - \left(\frac{\lambda}{n_r}\right)\left(\frac{dn_r}{d\lambda}\right)\right]} \tag{4-20}$$

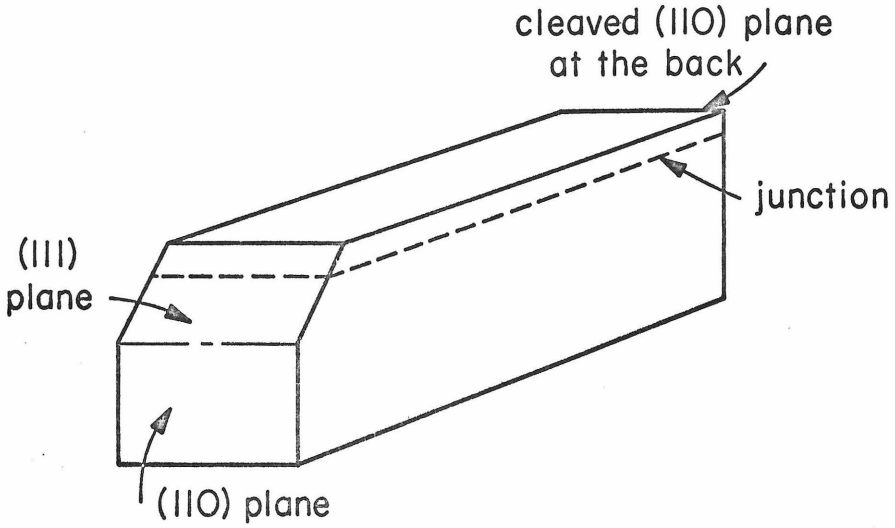

Figure 4-1. Non-Lasing Diode Cavity of InAs

4-4 Experimental Data and Discussion

4-4a. Figure 4-2 shows the observed threshold current density J_{in} plotted as a function of $1/\ell$ for two sets of diode samples. In agreement with the relation (4-5), reasonable linear fits can be made to the experimental points. These fits yield the following values for the distributed loss coefficient α and the gain constant β for the two sets of diodes:

$$\begin{aligned} &(1) \quad \alpha = 40 \text{ cm}^{-1} ; && \beta = 10 \text{ amp cm}^{-1} \\ &(2) \quad \alpha = 40 \text{ cm}^{-1} ; && \beta = 7.5 \text{ amp cm}^{-1} \end{aligned} \tag{4-21}$$

The acceptor doping depth and profile are not expected to be uniform all over the large wafer (diameter $\sim$ 2 cm) into which the Zn was diffused. A slight variation in the junction profile could account for the small difference in the values of β .

Although the exact agreement in the two values of α is rather fortuitous, it is gratifying to see the values to be in agreement since the doping concentrations for the two groups of diodes were the same.

Sources which may contribute to the loss coefficient α are (a) valence band to conduction band absorption or acceptor level to conduction band absorption and (b) free carrier absorption. The free carrier absorption may be within the conduction band, or within a given valence band, or an interband transition between the different light hole and heavy hole valence bands. Usually it is the last of these that gives the major contribution to free-carrier absorption constant values (this is because momentum conserving transitions can occur between the different bands). The photon energy observed from the

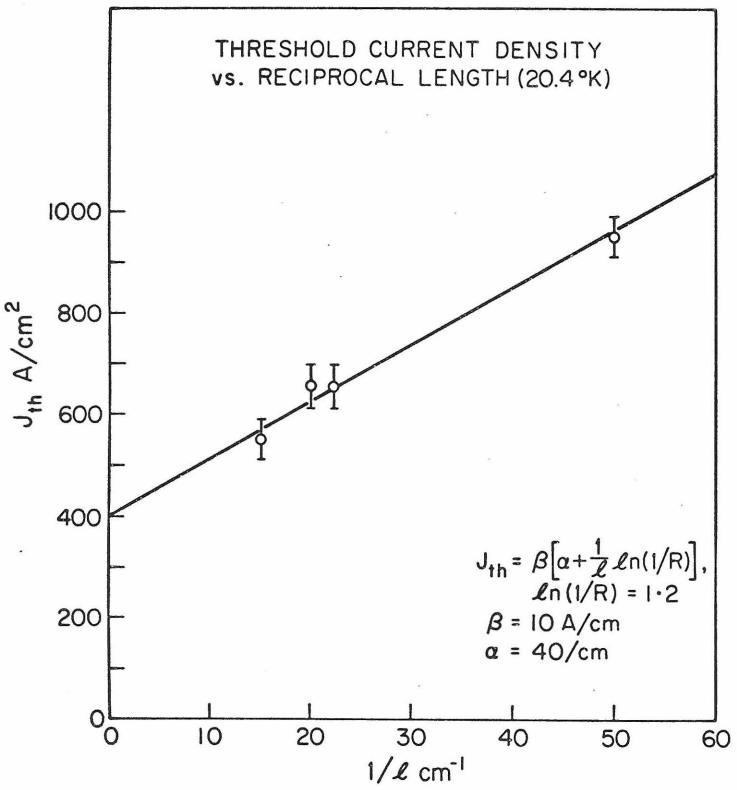

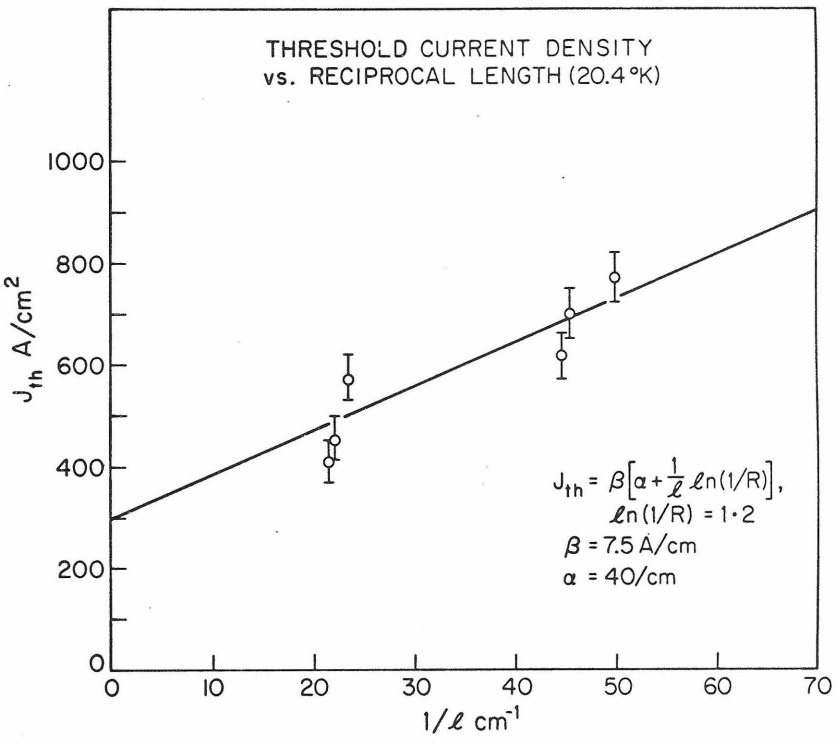

Figure 4-2. J_{th} vs. $1/\ell$ Data (20.4°K)

stimulated emission spectral data of InAs diodes at 20.4°K is .400 ± .003 eV, while the bandgap at that temperature is .42 eV. This value of the photon energy agrees with that observed by Melngailis [3] in his work on similarly constructed InAs diodes. By comparing the emission from diodes with different donor doping levels and photoluminescence from n and p type InAs single crystals with different dopings, he concluded that the diode emission was resulting from a recombination between the conduction band (and/or donor levels) and Zn acceptor levels lying about 17 meV above the valence band.

Since the energy of the photon is less than the bandgap, it cannot be absorbed via a band to band transition, but it could be absorbed via an acceptor level to conduction band transition. The published values for the absorption constant for free-carrier absorption [13] and acceptor level to conduction band transition [14] for samples with comparable doping are of the same order of magntidue as in (4-21). Thus it looks probable that cavity losses are due to free-carrier absorption and acceptor level to conduction band transition.

4-4b. Figure 4-3 shows a number of spectral output curves as the injection current was increased from 0.4A to 13.5A, while Fig. 4-4 shows a plot of $(\frac{\delta\nu}{\Delta\nu})$ vs. $I^{-1/2}$. At high pumping rates (high currents), a linear relationship is obtained, in agreement with (4-18). The value of the gain constant β obtained from the slope of this line is

$$\beta = 16 \text{ A cm}^{-1} \qquad (4\text{-}22)$$

The narrowing is observed to set in between 0.5 and 0.7A, which when using the above value of β, yields $\gamma(\nu_o) \simeq 15$ and

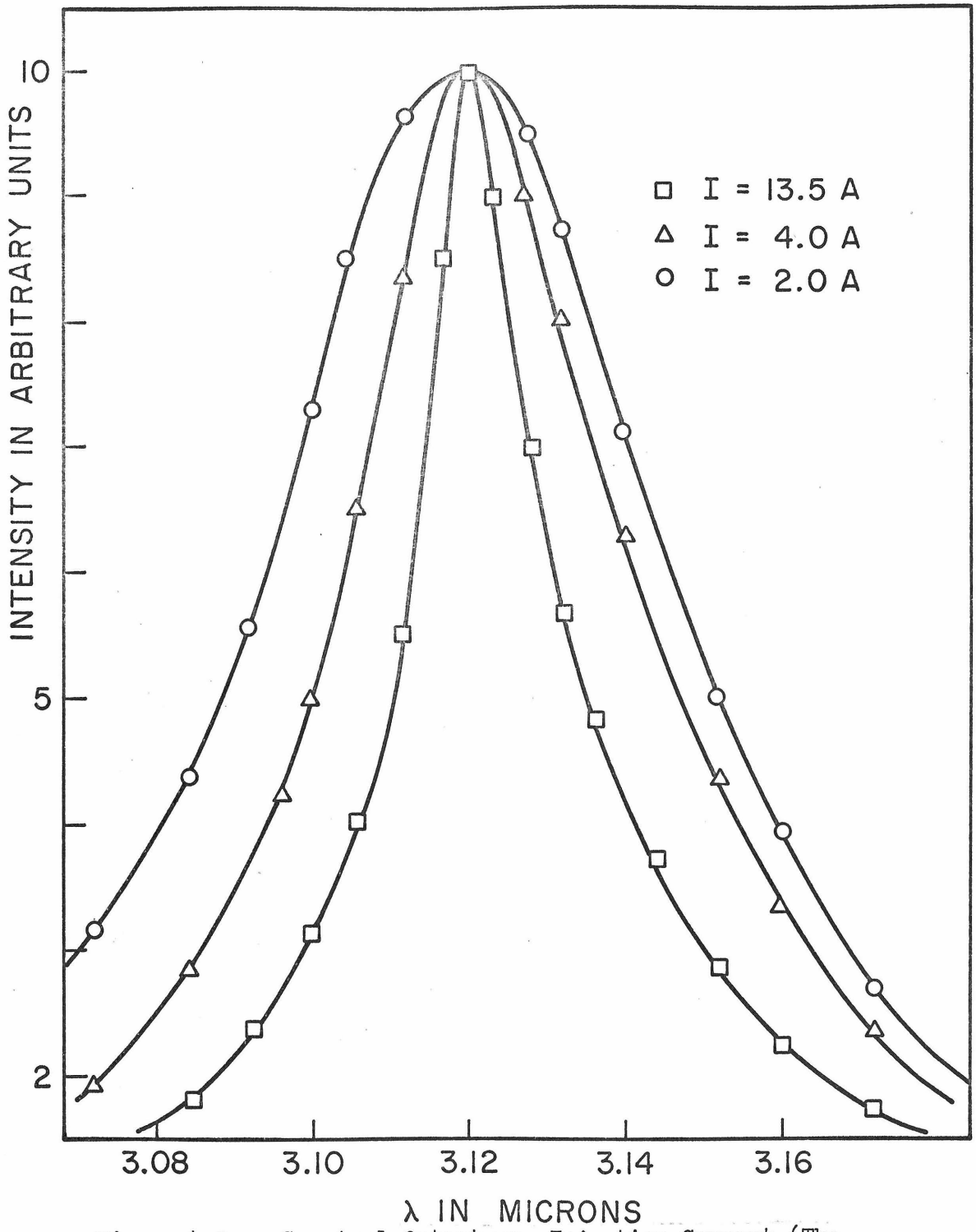

Figure 4-3. Spectral Output vs. Injection Current (The curves have been renormalized and shifted horizontally so as to have a single peak).

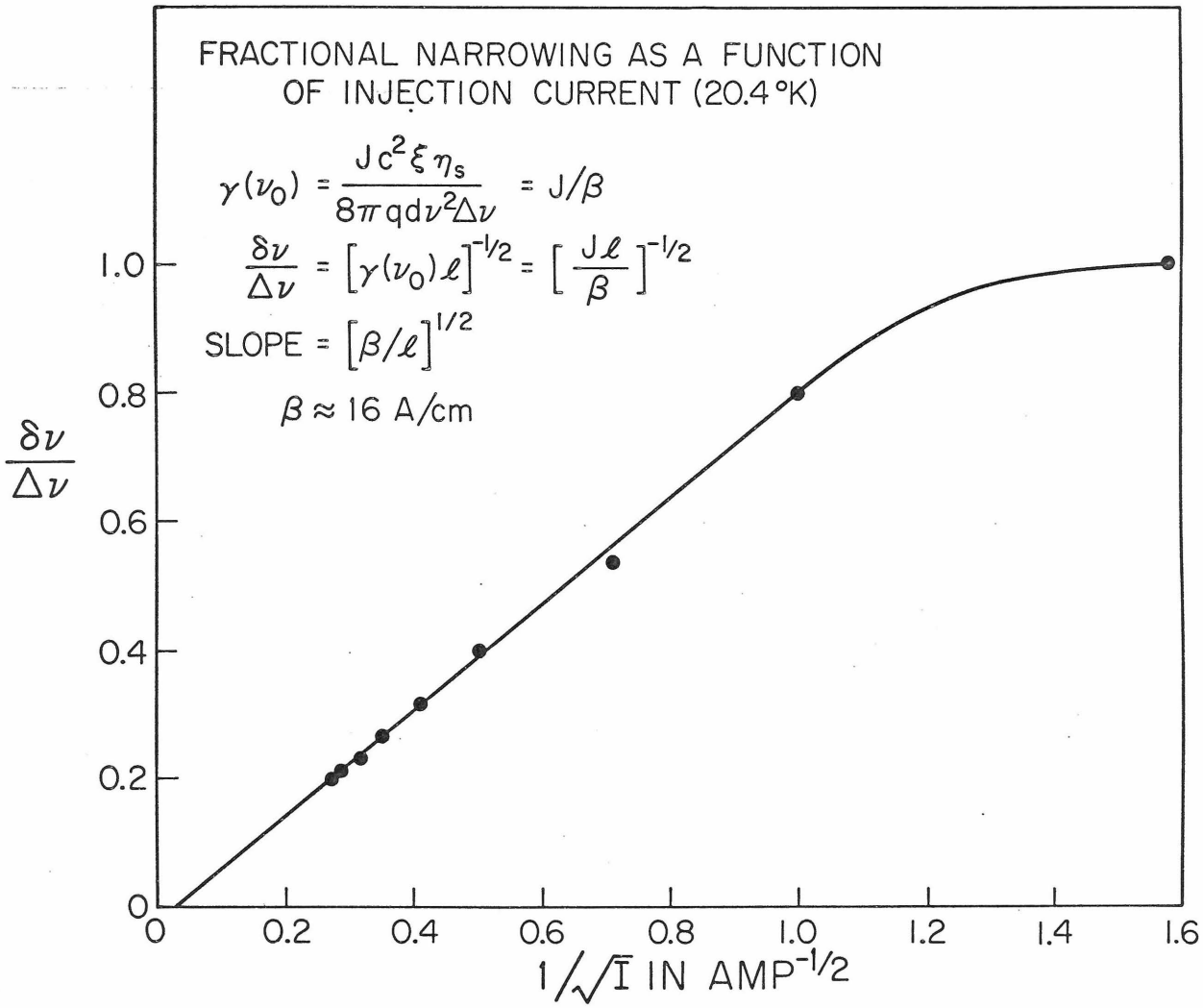

Figure 4-4. Fractional Line Narrowing vs. $1/\sqrt{I}$

$\gamma(\nu_o)\ell \simeq 1$, in agreement with the requirements for the onset of narrowing put down in (4-10).

4-4c. The narrow band spectral lines which characterize the stimulated emission from InAs diodes are shown in Fig. 4-5. These are for a current well above threshold and show the presence of five families of stimulated modes. The existence of different families of modes is easily understood from the condition for constructive interference given by (4-19). Microscopic "steps" in the cleaved faces (which form the reflecting ends of the diode cavity) can form individual cavities, each with its own characteristic length L. Therefore it is possible to have several families of modes which can oscillate simultaneously. The measured wavelength separation for all the five families of modes is $\Delta\lambda = 50\text{Å}$ ($\pm 4\text{Å}$).

Substituting this into (4-20) we get a value for the dispersion coefficient $dn_r/d\lambda$ (at $\lambda = 3.11\mu$)

$$\frac{dn_r}{d\lambda} = 3.1 \times 10^{-5}\ \text{Å}^{-1} \tag{4-23}$$

This agrees very closely with the value one obtains by using the spectral data on similar diodes published by Melngailis [3].

The measured half width of 5Å of the spectral lines corresponds to the resolution of the grating spectrometer used.

4.5 Determination of the Threshold Current and Stimulated External Quantum Efficiency

In Fig. 4-6 is shown the $\mathcal{P}$-I data for diode L_{16}. We observe that at a current of 340 mA there is a very sharp increase in the intensity

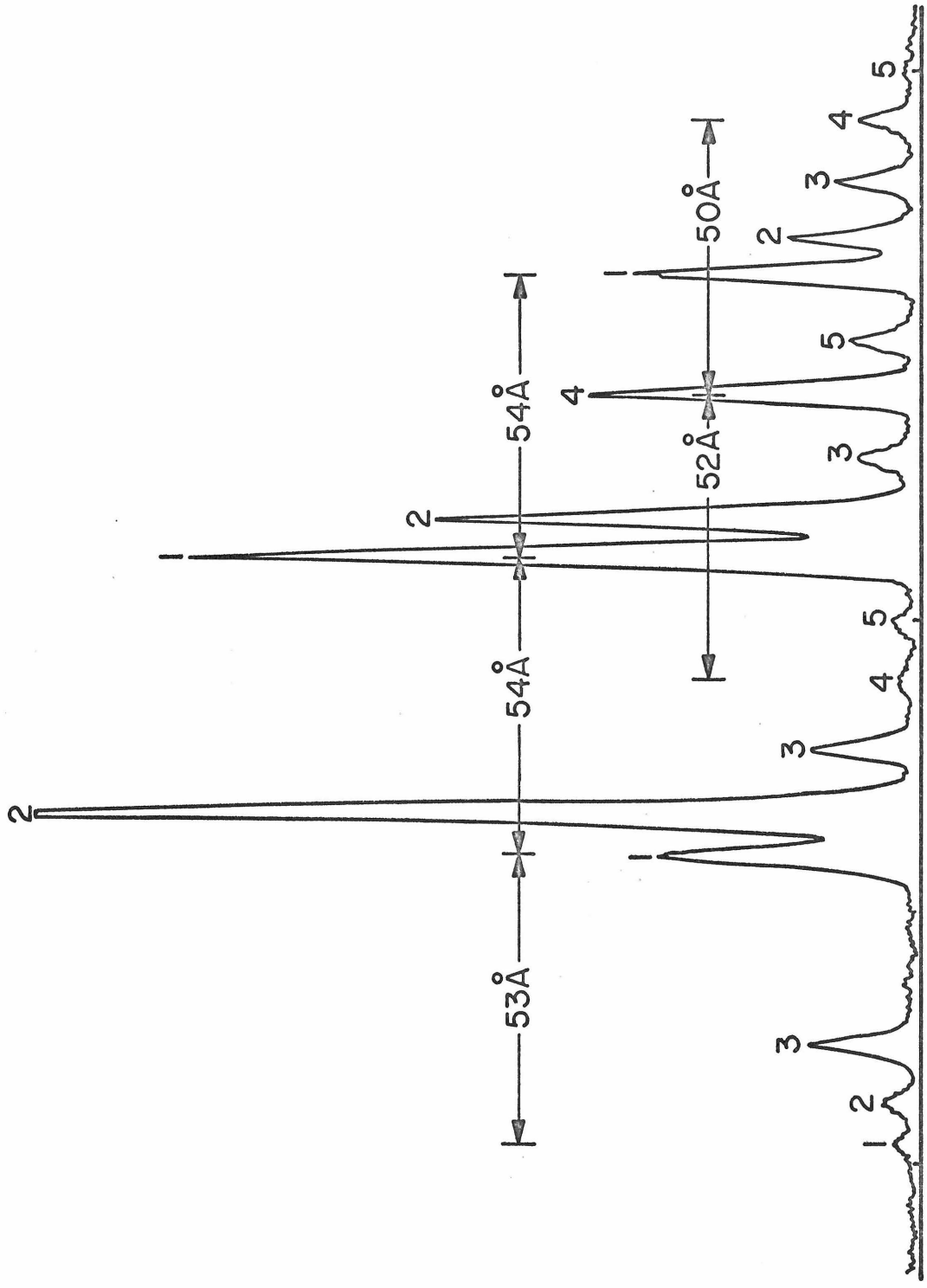

Figure 4-5. Spectral Intensity Data for Diode L_{26}

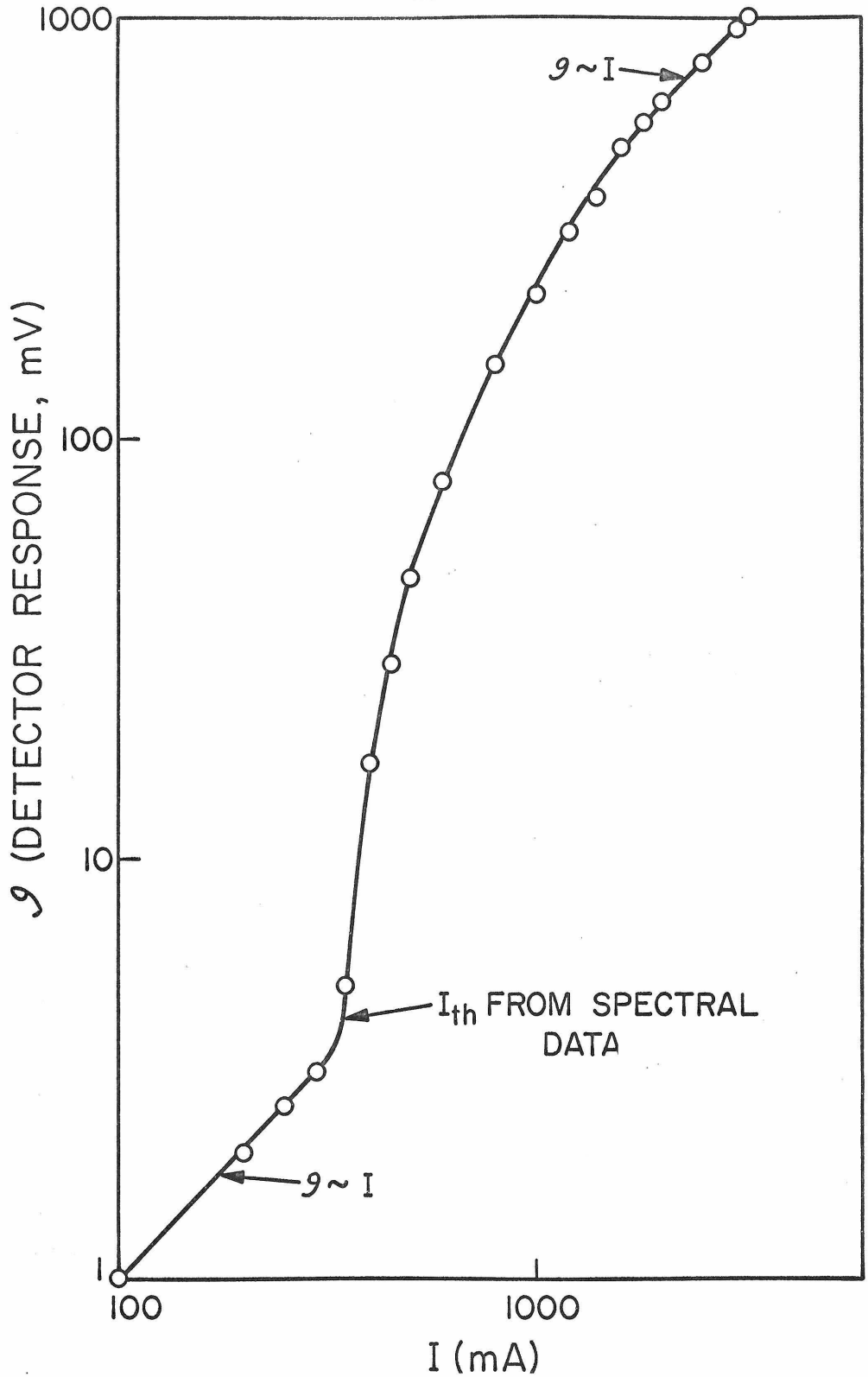

Figure 4-6. ϑ -I Data for Diode L_{16} (20.4°K)

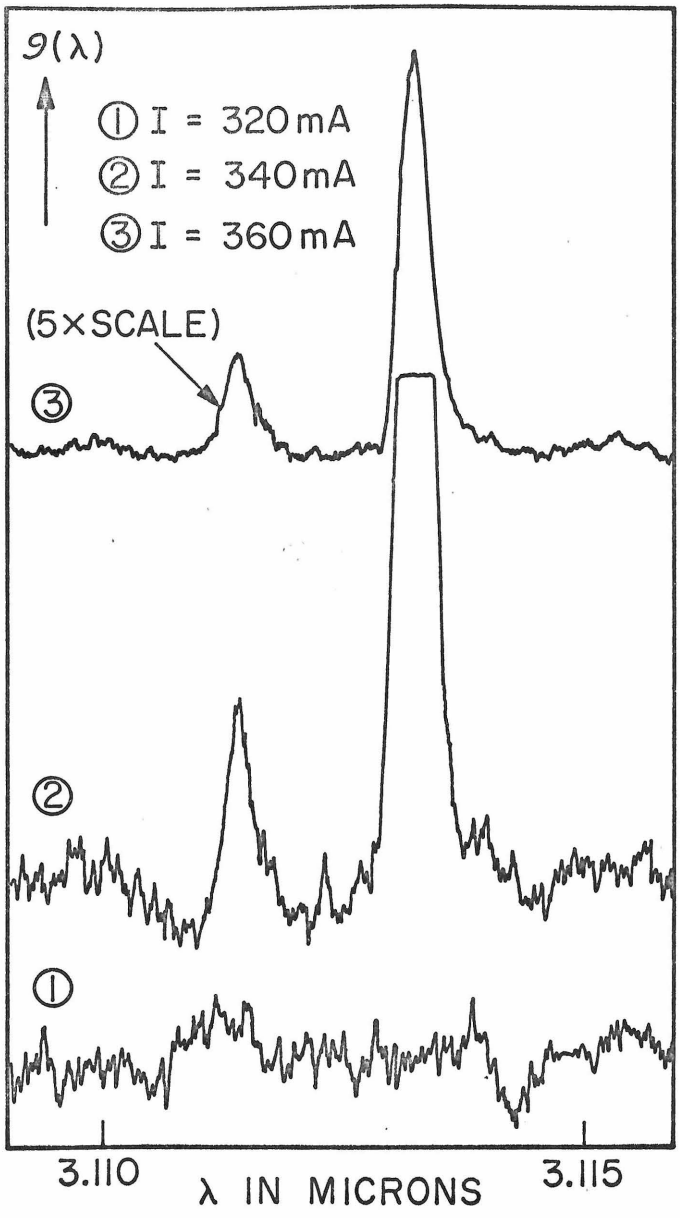

Figure 4-7. Spectral Intensity Data for Diode L_{16} (20.4°K)

$\mathcal{I}$ with increasing current. This is the threshold for stimulated emission, as is confirmed by the stimulated emission spectra $\mathcal{I}(\lambda)$ for the same diode shown in Fig. 4.7. We see that it is at 340 mA that the narrow bandwidth stimulated mode appears. We see thus that the threshold current for stimulated emission can be determined from the $\mathcal{I}$-I data by observing the current at which the sudden steep increase in $\mathcal{I}$ begins.

We observe in Fig. 4-6 that at high currents the increase of $\mathcal{I}$ with I slows down and ultimately we have the situation where $\mathcal{I} \sim I$. This is the so-called saturation region for stimulated emission, because the differential quantum efficiency η_d (i.e., $d\mathcal{I}/dI$) is constant in this region. We can determine η_d, knowing the parameters of the detector used, and using the relation 3-4 developed in Chapter III. We had

$$\eta_d = \frac{(\tau_t/\tau)}{\eta_D \, G R_L} \cdot \frac{d(\Delta V)}{dI} \qquad (4\text{-}24)$$

The quantity $d(\Delta V)/dI$ is the slope of the detector signal ΔV as a function of the diode current I, obtained from the $\mathcal{I}$-I data in Fig. 4-6. The numerical value of this slope is

$$\frac{d(\Delta V)}{dI} = 0.31 \text{ volts/amp} \qquad (4\text{-}25)$$

Substituting this into (4-24), together with the parameters of the detector used (Hg doped Ge at 20.4°K), we get

$$\eta_d \simeq 10\% \qquad (4\text{-}26)$$

This was a typical value obtained for most of the diodes.

The corresponding radiative power output of stimulated light ($\lambda = 3.1\mu$) for a diode current of 5 amps is 200 milliwatts.

Chapter V

Heating Effects and Time-Resolved Spectra

General Remarks:

When injection lasers are driven by current pulses, the temperature rise during the pulse causes transient changes in the observed spectra. All pulsed injection lasers exhibit "mode jumping" to longer wavelengths during the time interval when the laser is pumped, particularly under conditions of high peak current. As the temperature of a junction laser is changed two kinds of wavelength shifts are observed. First, the peak of the broad emission (which envelopes the laser spectrum) shifts, approximately at the same rate as the energy gap of the semiconductor used in fabricating the junction. In addition, there is a shift of individual laser modes with temperature, usually at a smaller rate. Thus as the temperature is raised, a particular mode will change its wavelength continuously, but will have its amplitude diminish and become unobservable when it no longer falls within the spontaneous emission envelope [15].

Several sources of heat generation can cause a junction temperature rise: (1) joule power dissipation in the semiconductor bulk region and at the contacts (2) reabsorption of the spontaneous and stimulated radiation (3) non-radiative recombination in the junction region.

We will show that in the InAs junction lasers used, the first effect predominates at moderate to high peak currents and that the shift of the peak photon energy of the emission follows the change of bandgap energy of InAs with temperature.

In order to study the changes in the laser spectrum occurring with

increasing time during the applied pulse, it is necessary to resolve spectrally the light output occurring during very small time intervals (compared to the total time of the applied current pulse) at different points along the pulse. In other words, it is necessary to obtain time-resolved spectra of the light output of the pulsed injection laser.

Experimental set-up:

The time-resolved spectra of the pulsed laser were obtained with the system outlined in Figure 5-1. The combination of a high-speed detector [Ge:Hg operated at 20.4°K, time constant < 50 ns] and a PAR boxcar integrator with gatewidth capability down to a nanosecond was used to satisfy the requirement that the system sample, and resolve spectrally, light output occurring during time intervals as small as .1 μs or less.

The laser (at 77°K) was pulsed with square current pulses, approximately 10 μs long, at a repetition rate of 20 per second. The emitted radiation was spectrally resolved by passing it through a spectrometer and then detected with the high-speed detector. The detector output was fed into the boxcar integrator with a gatewidth of .2 μs, and the d.c. output from the boxcar drove a pen recorder. The spectral content of the light pulse at a particular time along the pulse was measured by choosing the starting time of the gate of the boxcar integrator to coincide with that time, and then scanning with the spectrometer.

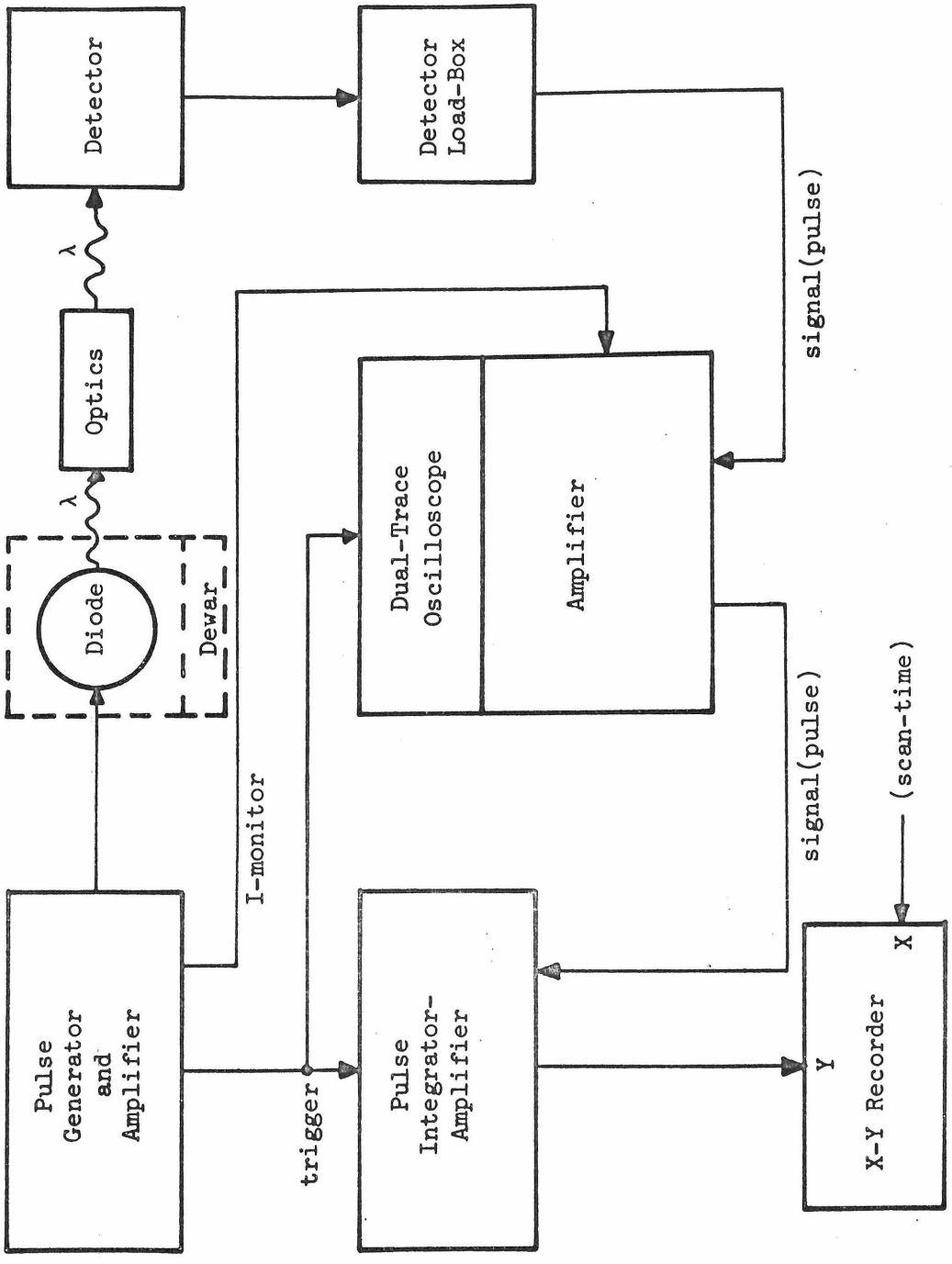

Figure 5-1. (a) Data Acquisition Scheme for Time-Resolved Spectra (Electronics)

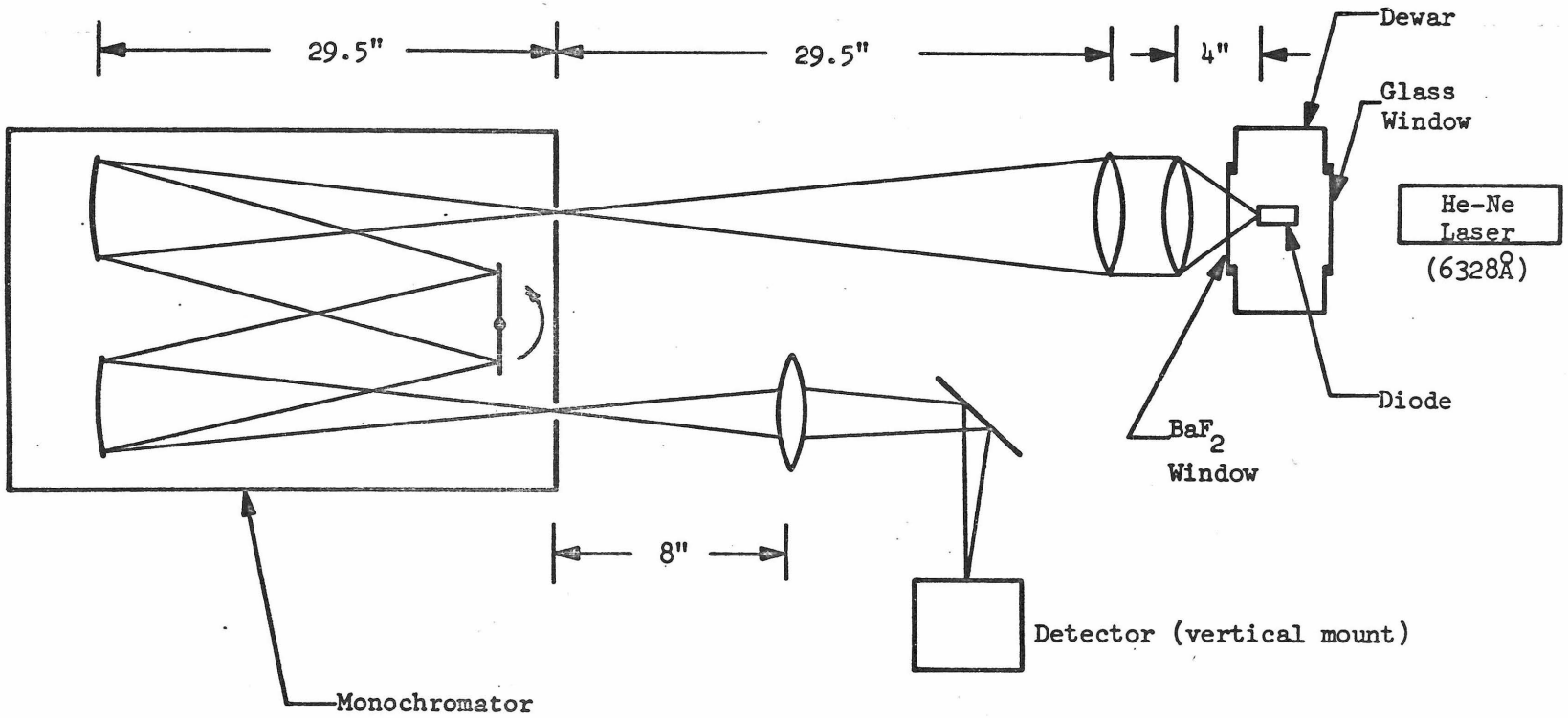

Fig. 5-1 (b) Data Acquisition Scheme for Time Resolved Spectra (Optics).

Experimental Data and Discussion:

Figure 5-2 shows typical data which illustrate the shift of the peak photon energy of the emission (the line shift) in the time-resolved spectra for a current of 6.0 Amperes. In order to follow the shift of the peak of the broad emission the resolution of the spectrometer was reduced, so that neighboring modes merged into one another.

Figure 5-3 shows the line shift as a function of time for various injection currents. It is seen that the line shift is linear with time and is proportional to the square of the current, indicating that the junction temperature rise is due to joule heating. A linear relationship with current would have indicated reabsorption and/or non-radiative processes as the source of heating.

The shift is seen to follow the relation

$$\Delta\lambda = k\, I^2\, t \quad \text{Å} \tag{5-1}$$

where I is in Amperes and t in μsec. For this particular diode the average experimental value of the lineshift coefficient k is found to be

$$k = 0.77 \ \text{Å}/_{A^2} - \mu s \ . \tag{5-2}$$

The line shift coefficient k can be calculated from the device and material parmeters, as follows. The joule heating power is $P_j = I^2 R$ where R is the series resistance of the diode (for the currents used, this is the dominant resistance of the device). Neglecting cooling during the passage of the current pulse, the junction temperature rise is given by

$$\Delta T(t) = \frac{P_j t}{cdv} = \frac{I^2 R t}{cdv} \tag{5-3}$$

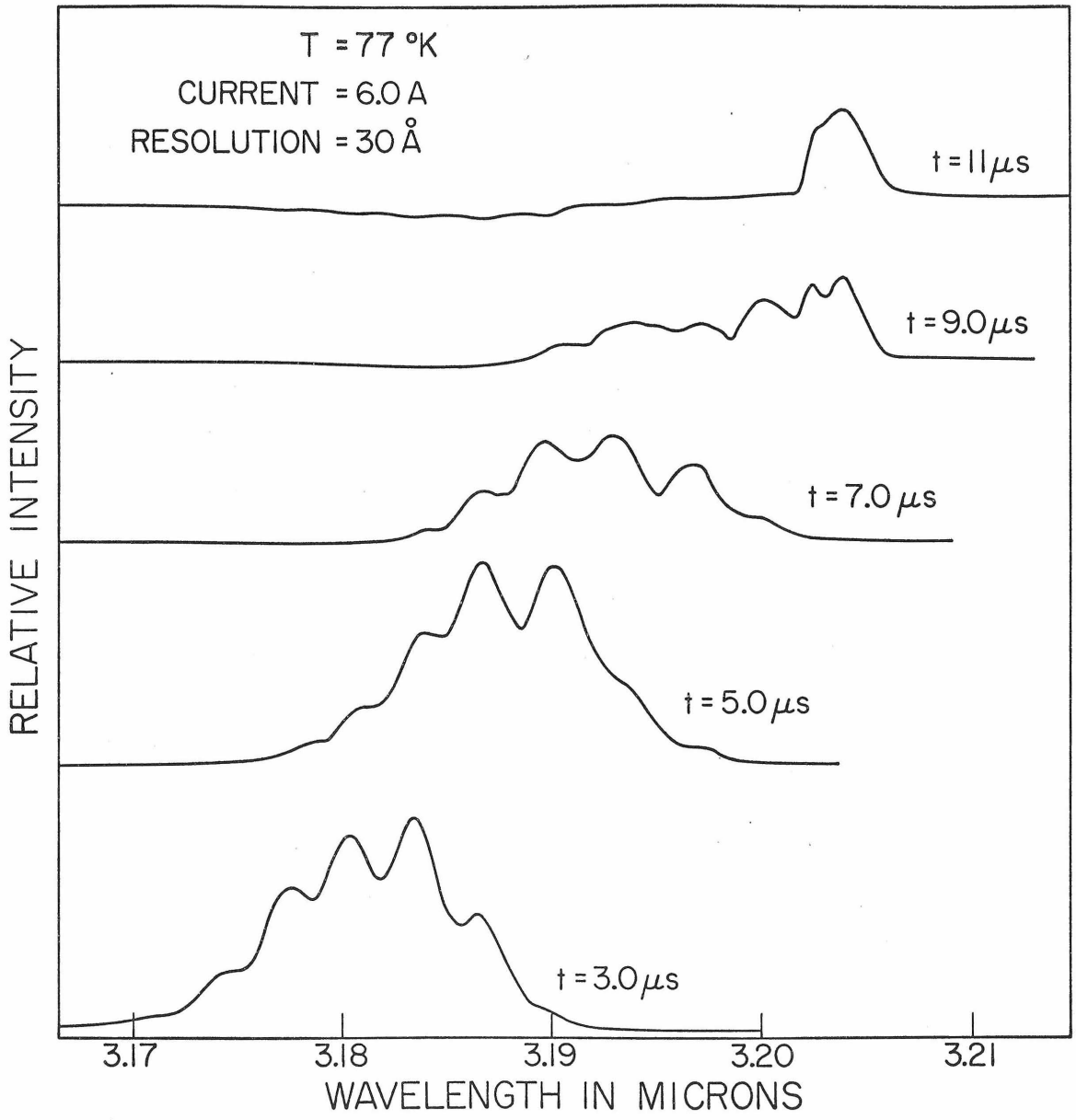

Figure 5-2. Time-Resolved Spectra at I = 6.0A

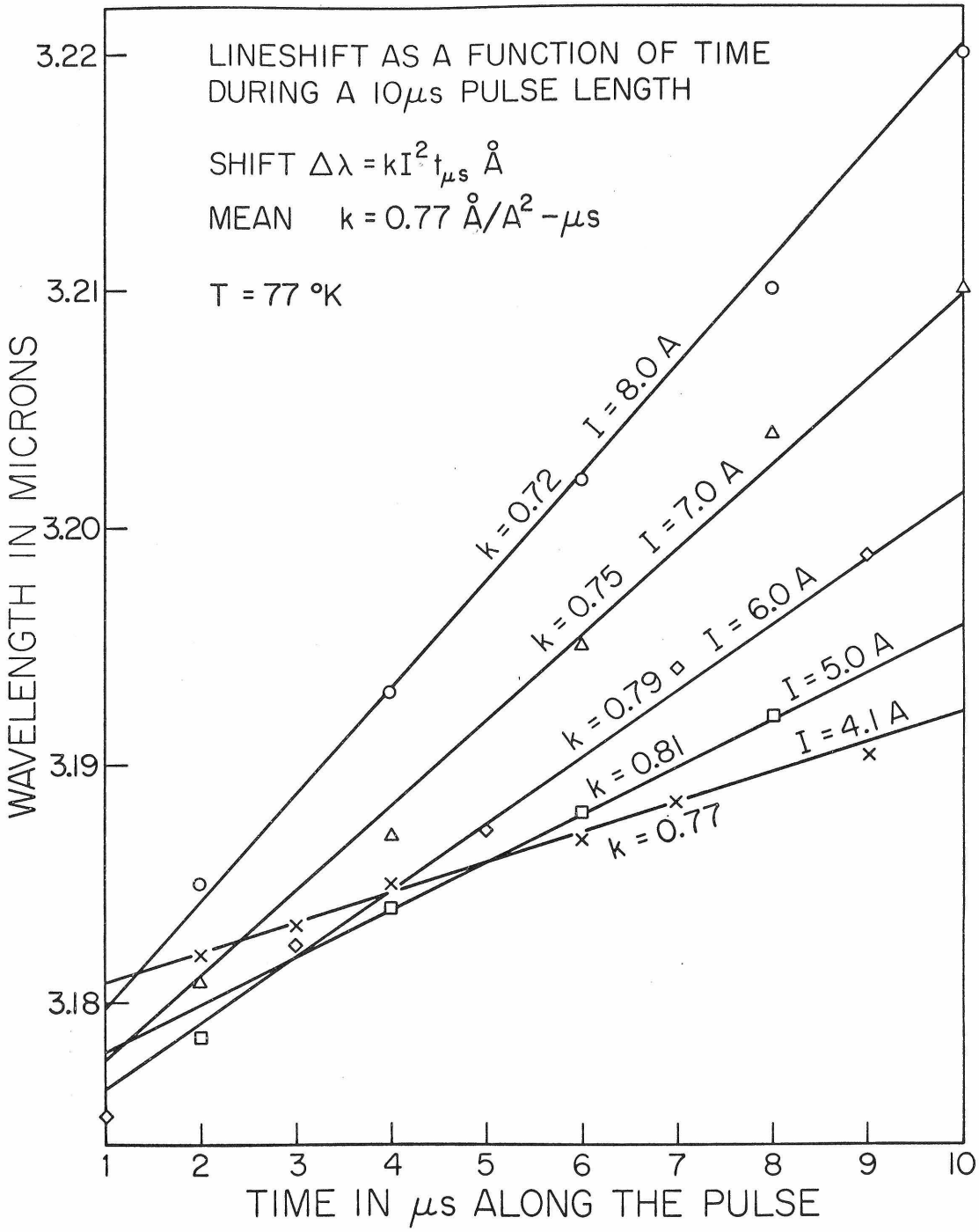

Figure 5-3. Laser Lineshift as a Function of Time

where c is the specific heat capacity of the material at $77^{o}K$, d is the density and v the volume of the diode.

If we assume that the laser line temperature coefficient is identical to that for the bandgap (-2.8×10^{-4} eV/$^{o}_{c}$) [5], the laser line shift is given by

$$\delta E = -2.8 \times 10^{-4} \Delta T \text{ eV} \qquad (5\text{-}4)$$

Writing this in terms of $\delta\lambda$ and substituting for ΔT from (5-3) we get

$$\delta\lambda = 0.74 \, I^2 t \quad \text{Å} \qquad (5\text{-}5)$$

Where I is in Amperes and t in μsec. We see that the calculated line shift coefficient agrees quite well with the measured value.

It can be demonstrated that joule heating can be expected to dominate over the other two processes for the range of currents used in this experiment. Compared with the joule heating power $P_j = I^2R$, the rate of heating by the other two processes is $P_n = (1-\eta_{ext})\, IV_g$. Here η_{ext} is the external quantum efficiency of the diode and V_g the potential drop across the diode junction. For this particular diode we had, $R = .33\ \Omega$, $\eta_{ext} \simeq 0.1$ and also $V_g \simeq 0.4$ V. Substituting these values in the expressions for P_j and P_n we have

$$\frac{P_j}{P_n} \simeq .9\, I \qquad (5\text{-}6)$$

Thus we see that for the currents used (4 A to 8A), P_j will dominate over P_n.

In all of this there has been the tacit assumption that during the

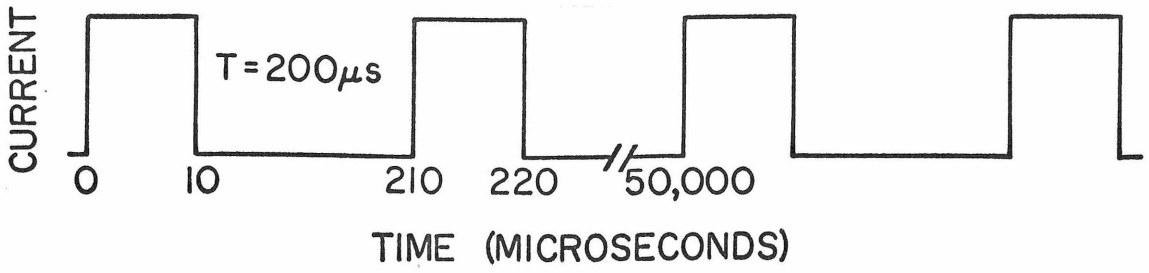

Figure 5-4. Pulse Train Employed in Double-Pulse Experiment

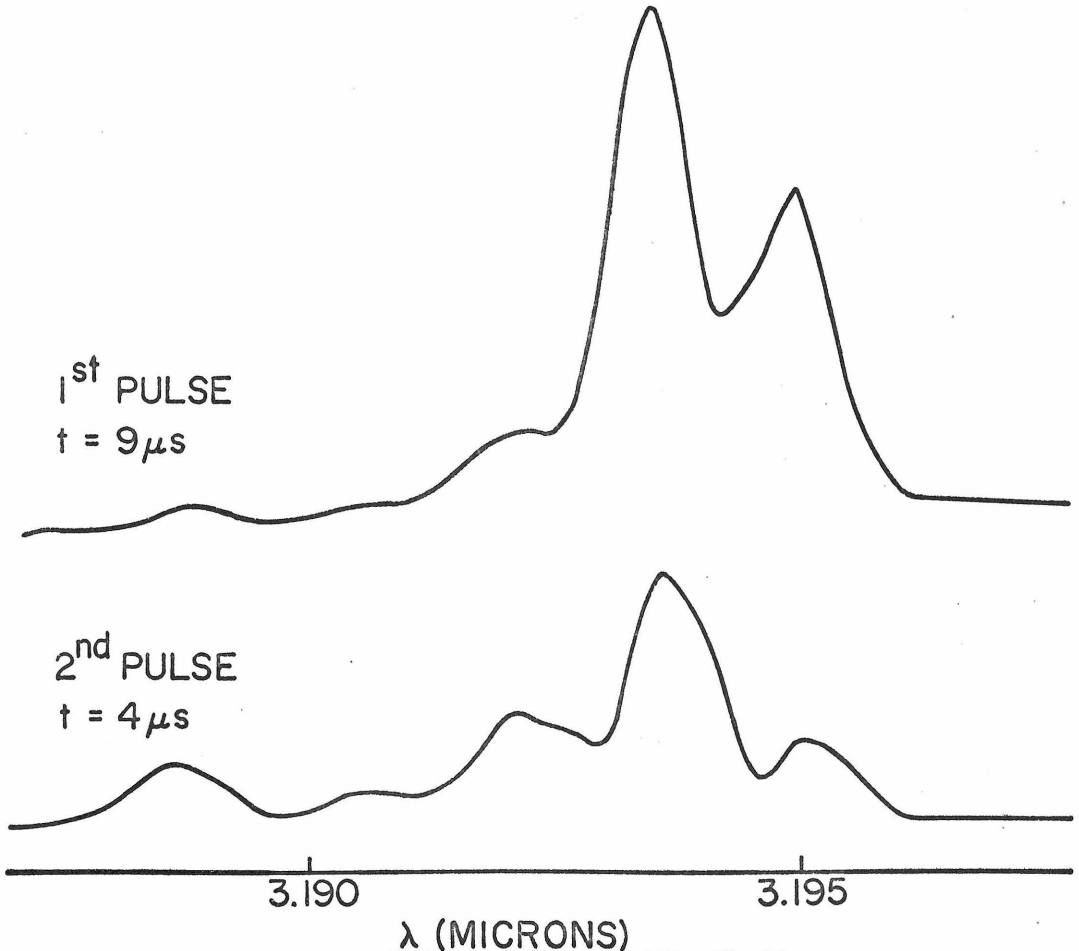

Figure 5-5. Comparison of Spectra in the First and Second Pulses

passage of the current pulse (~10 μs) the diode acts as a heat integrator, i.e. very little heat escapes to the heat sink, and also that by the time the next pulse arrives (time between pulses = 50 milliseconds) all the heat generated has been drained away by the heat sink. This was checked by a simple experiment. With the same set-up as before, the diode was pulsed with a double-pulse (Figure 5-4, each pulse being of 10 μs duration) at the same repetition rate as before, i.e. 20 double pulses per second. The time T between the two pulses in the double pulse was variable.

Time resolved spectra were obtained for both the pulses. With T = 200 μs and I = 5 Amp, it was found that the spectrum at beginning of the second pulse matched with 5μs spectrum of the first pulse. Similar matching was obtained for other spectra with a time difference of 5 μs between the corresponding points on the two pulses. This is shown in Figure 5-5 for the 9μs and 4 μs spectra of first and second pulse respectively. This indicates that when the second pulse of the double pulse arrives, there is some heat (from the first pulse) left in the diode, the amount of which corresponds to that which would be generated by a current pulse 5 μs long. Thus the time constant for heat escape from the diode is of the order of 200 μs, confirming the assumptions made at the beginning of this discussion.

Chapter VI

Mode Confinement

The active region of a p-n junction diode, over which stimulated emission can take place, is normally a few microns in width. A plane electromagnetic wave propagating along a region this narrow, upon getting reflected (partially) from an end of the diode cavity, would suffer quite a large diffraction, (the diffraction angle is $\Omega \simeq 2\lambda/d$, where the radiation of wavelength λ is confined to a distance d normal to the junction). Consequently at the other end of the diode cavity, a distance L away, only a fraction $d/L\Omega = d^2/2\lambda L$ of the reflected radiation would be incident on the active region aperture of height d. Thus the diffractions at end faces would constitute a large loss mechanism. Using the typical parameters for an InAs junction laser of $L = 0.2$ mm, $\lambda \simeq 1\mu$ (in the material), $d \simeq 6\mu$ the loss is $d^2/2\lambda L \simeq 9 \times 10^{-2}$, which corresponds to an exponential loss coefficient

$$\alpha_{\text{diffraction}} = \frac{1}{L} \ell n \frac{d^2}{2\lambda L} \simeq 125 \text{ cm}^{-1}.$$

However it is observed (Chapter IV) that the total loss coefficient for such lasers is an order of magnitude less than this value. Most of this loss can be accounted for by other loss mechanisms, and the estimated diffraction loss in the p-n junction diode laser is only a few reciprocal centimeters. This is because the diffraction loss is negated to a large extent by the confinement of the radiating modes due to variations in the real part of the dielectric constant near the

active layer. This has a lens-like focussing effect whereby the mode intensity is enhanced in a middle region of high dielectric constant, bounded by regions of lower dielectric constant with spatially decaying intensities. Thus the active layer acts a dielectric waveguide in which the otherwise diverging rays of the reflected beam are focussed back toward the axis.

A simple dielectric waveguide model, representing the situation to first-order, is illustrated in Figure 6.1. An inner layer with thickness $2d$ and dielectric constant $K\varepsilon (K > 1)$ is sandwiched between regions with dielectric constant ε. The corresponding solutions to the Maxwell's equations have been examined by Leite and Yariv [16] for the additional condition that the magnitudes of $\overline{E}$ and $\overline{H}$ (the electric and magnetic vectors) be constant in planes parallel to the junction. The solutions for the electric field in the TE-even mode, propagating as $\exp(-i\beta z)$, are of the form

$$E_y = B \cos(hx)\exp(-i\beta z) \qquad |x| \leqslant d \qquad (6.1a)$$

$$E_y = A \exp[-p(|x| - d) - i\beta z] \qquad |x| \geqslant d \qquad (6.1b)$$

where A and B are constants. The only other nonzero field-components are H_x and H_z. E_y and H_x are related by

$$\frac{E_y}{H_x} = \sqrt{\frac{\mu}{\varepsilon}} \qquad (6.2)$$

where μ is the permeability of the medium. The boundary condition

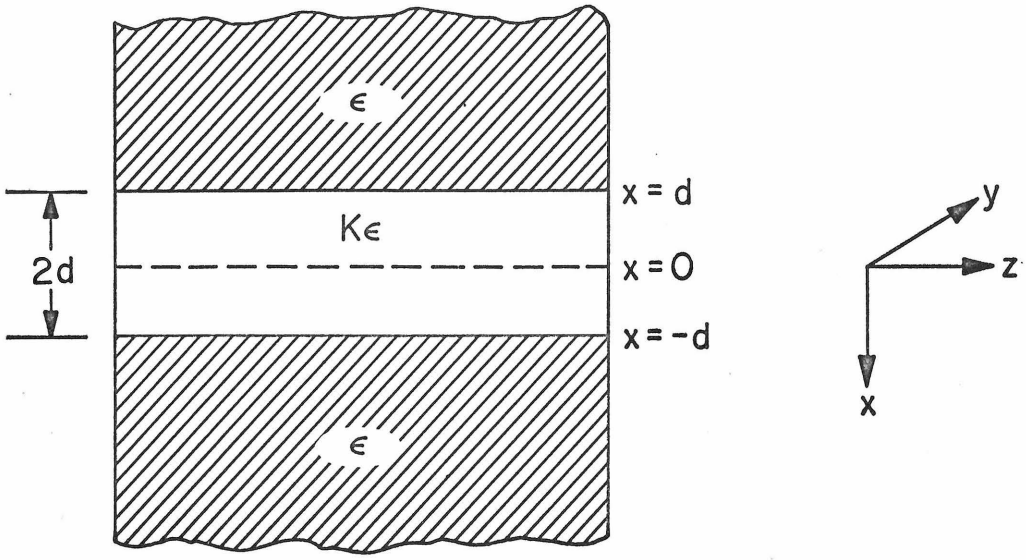

Figure 6-1. Geometry of Diode Dielectric Cavity

that E_y be continuous at $x = d$ gives

$$A = B \cos hd \tag{6.3}$$

Using this and the additional boundary condition that H_z be continuous at $x = d$, we obtain the following relation between p, h, and d

$$pd = hd \tan(hd) \tag{6.4a}$$

Applying the wave equation $\nabla^2 E_y + k^2 E_y = 0$ (where $k^2 = \omega^2 \mu\varepsilon$) at $x \leqslant d$ and $x \geqslant d$, we obtain the additional relation

$$(pd)^2 + (hd)^2 = (K - 1)k^2 d^2 \tag{6.4b}$$

The relations in (6.4) provide two equations and four unknowns (p, h, K, d). Therefore the experimental determination of p and h will allow the calculation of K and d.

The radiation intensity of an EM field is proportional to the real part of the complex Poynting vector (E x H*). It follows, using 6.2, that the intensity of energy flow per unit time in the z-direction is

$$\mathcal{I} \sim EE^* = E_y E_y^* \tag{6.5}$$

for the case under consideration.

The intensity as a function of the position $\mathcal{I}(x)$ in the direction perpendicular to the junction plane is then (using 6.5 and 6.1) given by

$$\mathcal{I}(x) = B^2 \cos^2 hx, \qquad |x| \leq d \qquad (6.6a)$$

$$\mathcal{I}(x) = B^2 \cos^2 hd \exp[-2p(|x| - d)], \qquad |x| \geq d \qquad (6.6b)$$

The experiment performed is the measurement of the far-field diffraction (intensity) pattern of a diode when oscillating in a stimulated mode of emission. The experiment, illustrated in Figure 6.2a, involves moving a detector (with input baffle-slits parallel to the junction) perpendicular to the junction (i.e. in the x direction) in the radiation field at a distance D from the radiating end of the diode.

The electric field of the diffraction pattern may be related to the electric field at the radiating source by using Huygen's principle. Since, for our case, $E_y(x)$ is constant in a given plane which is parallel to the junction, we have simply a one-dimensional diffraction problem. Using the notation and construction shown in Figure 6.2b, the diffraction field $E_y(x')$ due to the source field $E_y(x)$ is of the form [17]

$$E_y(x') \sim \int_F \frac{E_y(x) e^{-\frac{2\pi i}{\lambda} S(x,x')}}{S(x,x')} \, dx \qquad (6.7)$$

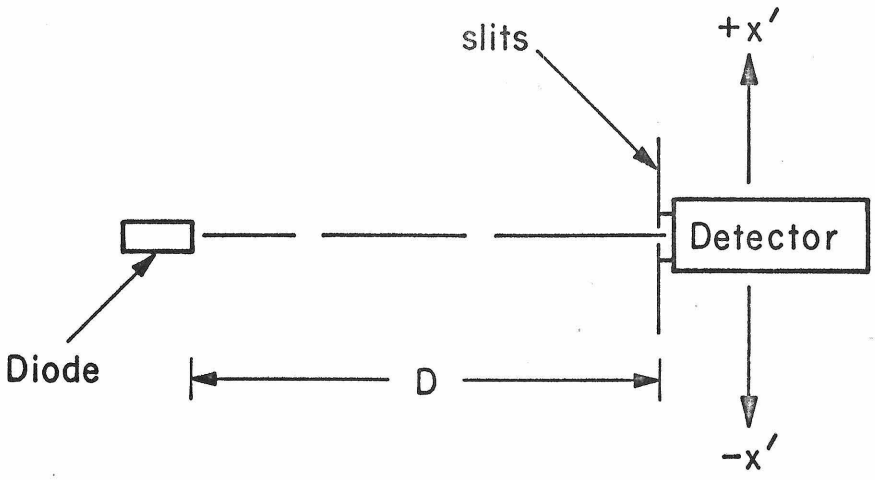

Figure 6-2. (a) Far-Field Diffraction Intensity Experiment

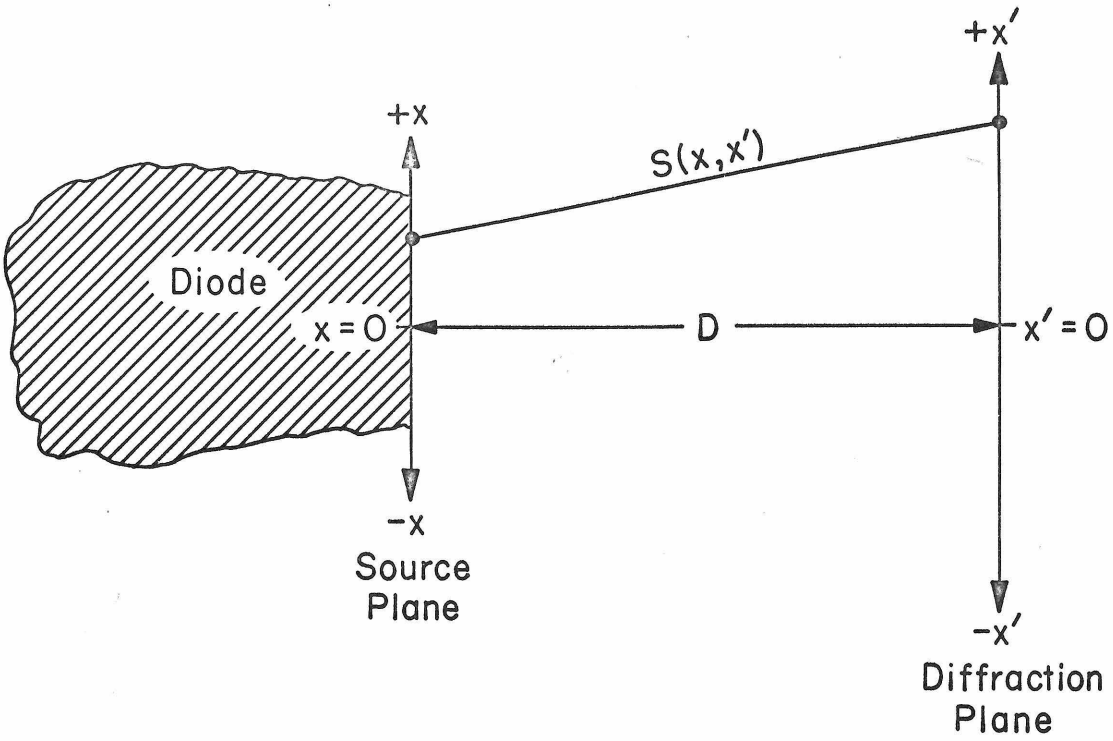

Geometry for Diffraction Field Calculation

Figure 6-2 (b)

In (6.7) it is assumed that the phase of the field $E_y(x)$ is constant over the width (F) of the emitting surface, allowing $E_y(x)$ to be a real quantity. The validity of this assumption is supported by the fact that the stimulated emission coming from the diode cavity is phase-coherent.

For the case of far-field (Fraunhofer) diffraction, where $x' >> x$ and $x'x << D^2$, (6.7) becomes

$$E_y(x') \sim \int_F E_y(x) e^{2\pi i \frac{x}{\lambda} \frac{x'}{D}} \tag{6.8}$$

The integral in 6.8 is just the Fourier transform integral for E_y in terms of the variables x and x'. The inversion of 6.8 gives

$$E_y(x) \sim \int_{F'} E_y(x') e^{-2\pi i \frac{x}{\lambda} \frac{x'}{D}} dx' \tag{6.9}$$

where F' is the width of the far-field pattern. If we take $E_y(x)$ to be symmetric in x (and since it already is real), we obtain $E_y(x')$ as a real quantity. We may then use the experimentally measured values of $\mathcal{I}(x')$ to determine $E_y(x')$. Using 6.5 we have

$$E_y(x') \sim [\mathcal{I}(x')]^{\frac{1}{2}} \tag{6.10}$$

We may therefore obtain, from the experimental data for $\mathcal{I}(x')$, the intensity profile $\mathcal{I}(x)$ at the radiating surface of the diode, using

6.10 in 6.9 and then the relationship

$$\mathcal{I}(x) \sim E_y^2(x) \tag{6.11}$$

The diffracted far-field intensity $\mathcal{I}(x')$ of the stimulated radiation from diode L_{26} at 20.4°K, is shown in Figure 6.3. The diode was pumped with a current of 290 mA. The stimulated emission spectrum at this current showed that the diode was oscillating in a single mode.

Using relations 6.9, 6.10, and 6.11, the $\mathcal{I}(x')$ data in Figure 6.3 was transformed into corresponding values for $\mathcal{I}(x)$. The result of this transformation is represented in Figure 6.4, by the dots, plotted on a semi-logarithmic scale. Also plotted are curves for relations 6.1, with values of h and p chosen to obtain best fits with the transformed experimental data represented by the dots.

The fit shows a consine-squared decrease for small x, changing to an exponential dependence which holds for an order of magnitude change change in $\mathcal{I}(x)$. Therefore the general nature of the source intensity profile $\mathcal{I}(x)$ is in accord with that predicted by the simple dielectric-waveguide theory. The values obtained from Figure 6.4 for the parameters in 6.1 are:

$$\begin{aligned} d &= 2{\cdot}5 - 3{\cdot}5\mu \\ h &= 0{\cdot}20\mu^{-1} \\ 1/p &= 7{\cdot}8\mu \end{aligned} \tag{6.12a}$$

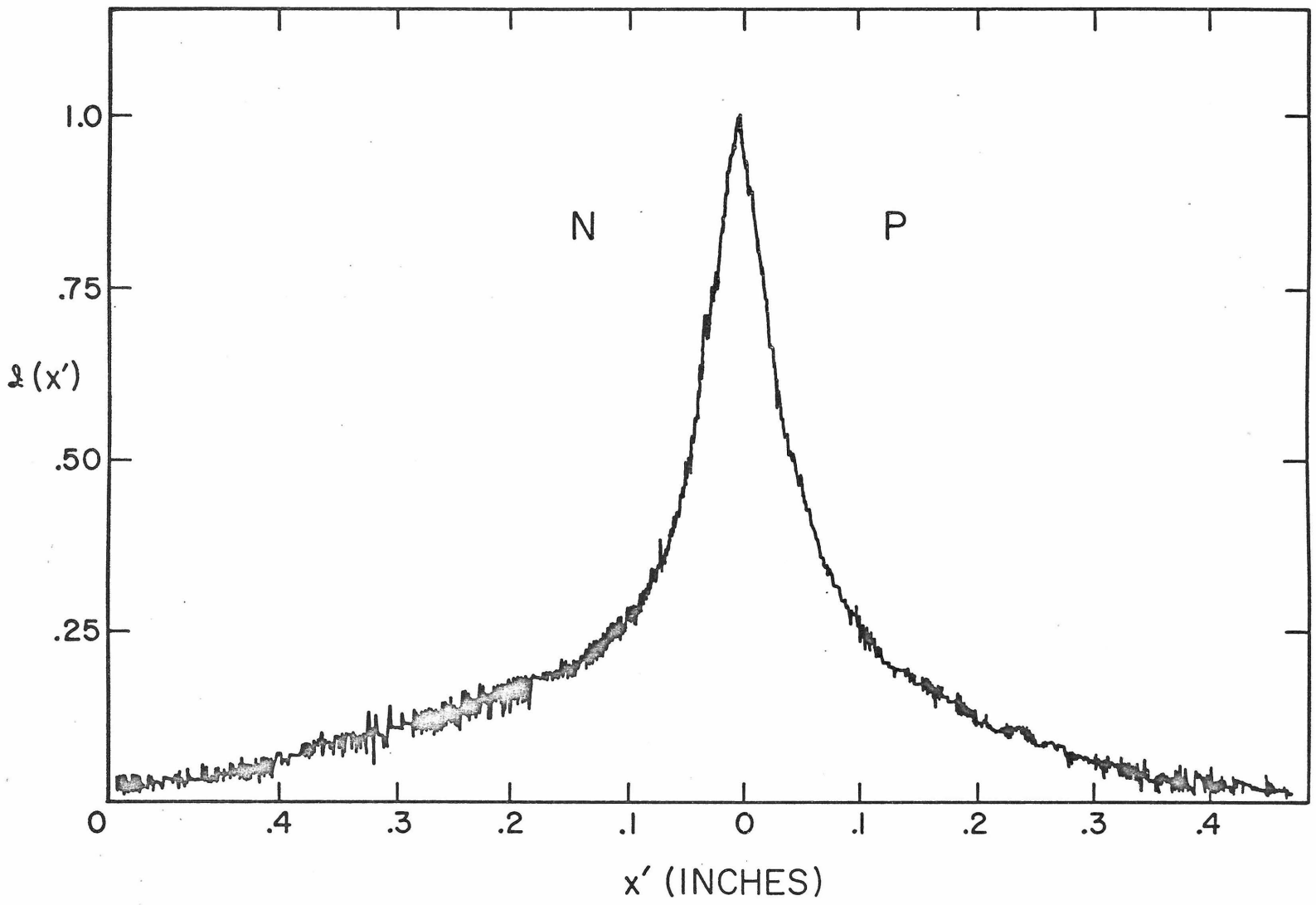

Figure 6-3. Far-Field Diffraction Intensity Data for Diode L_{26} (20.4°K)

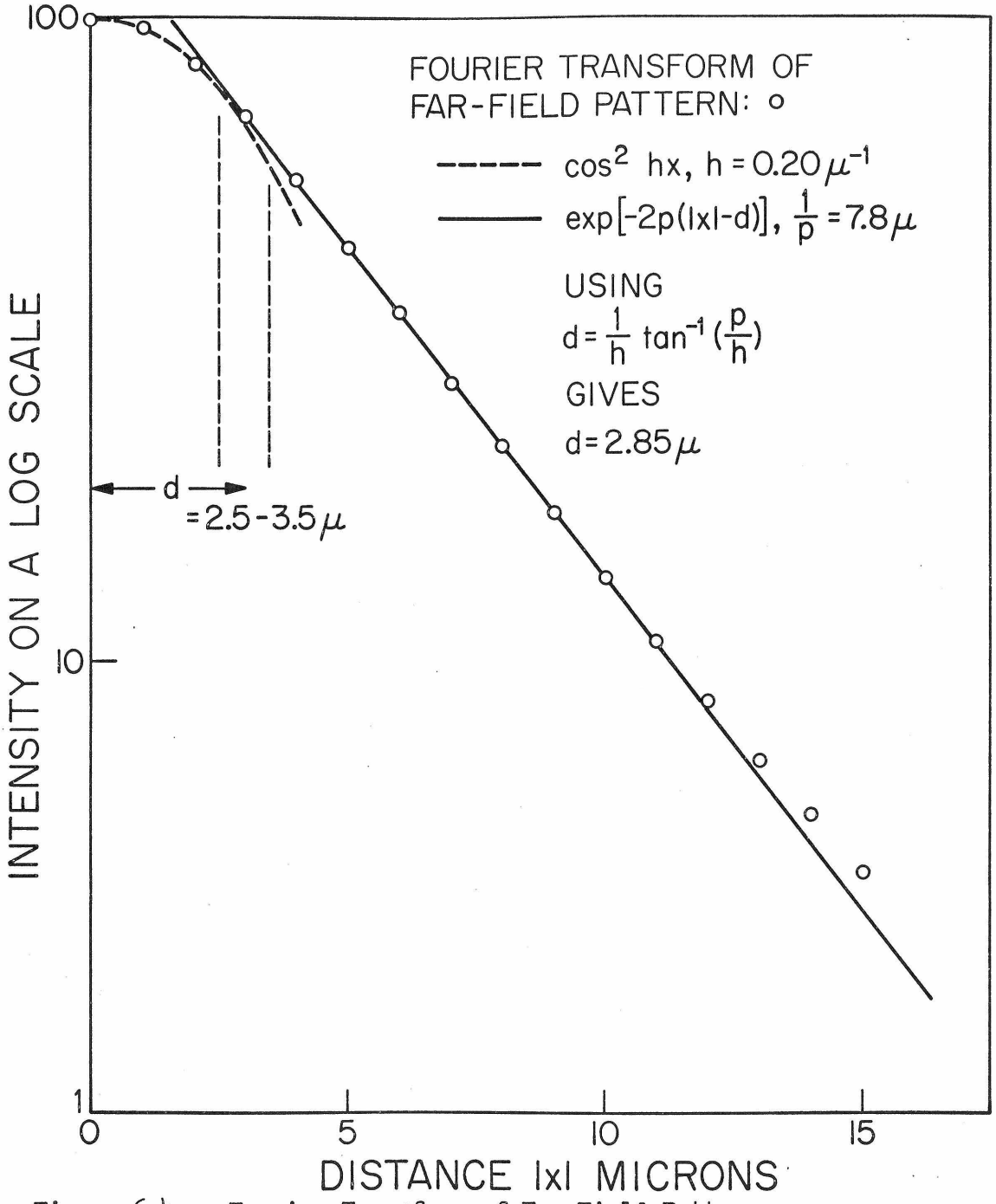

Figure 6-4. Fourier Transform of Far-Field Pattern

A self-consistency check can be made on the above experimentally determined parameters with the use of equation 6.4a. Using the values of h and p given by 6.12a, the corresponding value of d is

$$d = \frac{1}{h} \tan^{-1} \left(\frac{p}{h}\right) = 2{\cdot}9\mu, \qquad (6.12b)$$

in good agreement with 6.12a. In addition, equation 6.4b may be used to calculate the dielectric discontinuity $(\delta\varepsilon/\varepsilon)$ in the diode cavity, (Figure 6.1):

$$\frac{\delta\varepsilon}{\varepsilon} \equiv (K - 1) = \frac{p^2 + h^2}{k^2} = 1{\cdot}1 \times 10^{-3}. \qquad (6.13)$$

where $k = 2\pi n_r/\lambda$ and λ is the measured wavelength of the oscillations mode. The numerical value for $(\delta\varepsilon/\varepsilon)$ indicates the smallness of the dielectric discontinuity needed for the confimement of electromagnetic modes.

One of the mechanisms put forward to explain the physical origin of the observed $(\delta\varepsilon/\varepsilon)$ in semiconductor diodes is that in which the mechanism is directly related to the variation in the gain characteristic of the medium [18]. Associated with this variation in amplification from that of net gain in the active layer to loss (absorption) in the surrounding region, is a change in the imaginary part of the dielectric constant. This in turn is associated, via the Kramers-Kromg relations, with a change in the real part of the dielectric constant. The expression for $(\delta\varepsilon/\varepsilon)$ which results from such an analysis [18]

with the requirement that near threshold the power gain in the amplification (active) region balance the power loss in the absorption region, is as follows:

$$\frac{\delta\varepsilon}{\varepsilon} \simeq \frac{\alpha_t}{2kpd} \tag{6.14a}$$

where α_t is the total exponential intensity loss coefficient.

Substituting the observed values of α_t, k and p and d (6.12a) for the diode under consideration, we obtain

$$\frac{\delta\varepsilon}{\varepsilon} \simeq 1.4 \times 10^{-3} \tag{6.14b}$$

in fair agreement with 6.13

As discussed in Chapter I, the population inversion (and hence the active layer) caused by the injected minority carriers can be expected to extend upto a diffusion length on either side of the junction. Using the published values of minority carriers lifetime τ in InAs [19], the diffusion length L_D of the minority carriers can be calculated with the aid of the relation

$$L_D = \sqrt{D\tau} \tag{6.15}$$

where D is the diffusion constant. We obtain

$$L_D \simeq 2 \times 10^{-4} \text{ cm}$$

which is in fair agreement with the value of d (the half-width of the active region) in 6.12a.

REFERENCES

1. H. Welker, Z. Naturforsch 7a, 744 (1952).
2. R. N. Hall et al, Phys. Rev. Letters 9, 366 (1962); M. I. Nathan et al, Appl. Phys. Letters 1, 62 (1962); T. M. Quist et al, Appl. Phys. Letters 1, 91 (1962).
3. I. Melngailis, Appl. Phys. Letters 2, 176 (1963); I Melngailis et al, J. Appl. Phys. 37, 899 (1966); I. Melngailis et al, Appl. Phys. Letters 2, 202 (1963).
4. A. Yariv and R. C. C. Leite, J. Appl. Phys. 34, 3410 (1963).
5. J. Dixon and J. M. Ellis, Phys. Rev. 123, 1560 (1961).
6. M. G. A. Bernard and G. Duraffourg, Physica Status Solidi 1, 659 (1961).
7. D. Dewitt and A. L. Rossoff, Transistor Electronics, McGraw-Hill, 1957, p. 68.
8. C. T. Sah, R. N. Noyce and W. Shockley, Proc. IRE 45, 1228 (1957).
9. R. C. C. Leite et al, Phys. Rev. 137, A1583 (1965).
10. A. Yariv, Quantum Electronics, John Wiley and Sons, 1967, p. 284.
11. M. Philkyn and H. Rupprecht, Proc. IEEE 51, 12 (1963).
12. G. Burns and M. I. Nathan, Proc. IEEE 52, 770 (1964).
13. F. Matossi and F. Stern, Phys. Rev. 111 472 (195).
14. J. Dixon, Proceedings of the International Conference on Semiconductors, Prague, Publishing House of the C.A.S. 1960, p. 366 and reference [5] .
15. T. Gonda et al, IEEE J. Quantum Electronics 1, 159 (1965).
16. A. Yariv and R. C. C. Leite, Appl. Phys. Letters 2, 55 (1963); A. Yariv, ibid, pp. 287-289.
17. J. B. Marion, Classical Electromagnetic Radiation, Academic Press, 1965, Ch. 12.

18. R. C. C. Leite and A. Yariv, Proc. IEEE 51, 1035 (1963).

19. M. P. Mikhailova et al, Soviet Physics--Solid State 5, 1685 (1964).

List of Figures

Figure 1-1. Energy Bands in Semiconductors 6
(a) Conduction and Valence Bands
(b) Direct and Indirect Semiconductors

Figure 1-2. Radiative Transitions in Semiconductors 7
(a) Direct Semiconductor
(b) Indirect Semiconductor

Figure 1-3. Energy versus Density of States in a Semiconductor 9
(a) Equilibrium, T = $0^{o}K$
(b) Inverted, T = $0^{o}K$
(c) Inverted, T > $0^{o}K$

Figure 1-4. A Degenerate P-N Junction 12
(a) With Zero Bias
(b) With Forward Bias (V) and an Effective Population Inversion

Figure 1-5. Energy Band Diagrams of Tunnel Diode 16
(a) Zero Bias
(b) Reverse Bias
(c) and (d) Forward Bias

Figure 1-6. Tunnel Diode I-V Characteristic 17

Figure 1-7. The "Diagonal" Tunneling Model 17

Figure 2-1. Cleaving Configuration of (100) Wafer of InAs 21

Figure 2-2. Diffusion Tube for InAs 23

Figure 2-3. Diffusion Furnace 23

Figure 2-4. Lapping Configuration of InAs Crystals 23

Figure 2-5. Fabrication Steps for a Laser Diode Cavity 25

Figure 2-6. Finished InAs Laser Diode 26

Figure 2-7. Laser Structures Cleaved from (111) InAs Wafer 27

Figure 2-8. Cleaving Configuration of (100) Bars of InAs 28

Figure 2-9. Diode Mounted on a TO-5 Header 31

Figure 3-1. I-V Data Acquisition Scheme 36

Figure 3-2. C-V Data Acquisition Scheme 36

Figure 3-3. $\mathcal{S}$-I Data Acquisition Scheme 38

Figure 3 4. Ge:Hg Detector and Circuit 39

Figure 3-5. Detector Linearity 39

Figure 3-6. (a) $\mathcal{S}(\lambda)$ Data Acquisition Scheme (Electronics) 42

(b) $\mathcal{S}(\lambda)$ Data Acquisition Scheme (Optics) 43

Figure 3-7. C-V Data for Diode J_4 45

Figure 3-8. I-V Data for Diode J_4 46

Figure 3-9. -I Data for Diode J_4 47

Figure 3-10. I-V Data for Diode J_4 at 300°K and 195°K 50

Figure 3-11. Curve Tracer Display of I-V Characteristic of Diode K_9 at 77°K 52

Figure 3-12. I-V Data of Diode K_9 at 77°K 53

Figure 3-13. $\mathcal{S}$-I Data of Diode K_9 at 77°K 54

Figure 3-14. Model for Radiationless Diagonal Tunneling via Impurity Levels 56

Figure 4-1. Non-Lasing Diode Cavity of InAs 65

Figure 4-2. J_{th} vs. $1/\ell$ Data (20.4°K) 67

Figure 4-3. Spectral Output vs. Injection Current 69

Figure 4-4. Fractional Line Narrowing vs. $1/\sqrt{I}$ 70

Figure 4-5. Spectral Intensity Data for Diode L_{26} 72

Figure 4-6. -I Data for Diode L_{16} (20.4°K) 73

Figure 4-7. Spectral Intensity Data for Diode L_{16} (20.4°K) 74

Figure 5-1. (a) Data Acquisition Scheme for Time-Resolved Spectra (Electronics) 79

(b) Data Acquisition Scheme for Time Resolved Spectra (Optics) 80

Figure 5-2.	Time-Resolved Spectra at I = 6.0A	82
Figure 5-3.	Laser Lineshift as a Function of Time	83
Figure 5-4.	Pulse Train Employed in Double-Pulse Experiment	85
Figure 5-5.	Comparison of Spectra in the First and Second Pulses	85
Figure 6-1.	Geometry of Diode Dielectric Cavity	89
Figure 6-2.	(a) Far-Field Diffraction Intensity Experiment	92
	(b) Geometry for Diffraction Field Calculation	93
Figure 6-3.	Far-Field Diffraction Intensity Data for Diode L_{26} ($20.4^{o}K$)	96
Figure 6-4.	Fourier Transform of Far-Field Pattern	97